CONTROLLING NANOPARTICLE LOCATION IN BLOCK COPOLYMERS USING EXTERNAL FIELDS: EXPERIMENTS AND SIMULATIONS

A Dissertation

Presented to the Faculty of the Graduate School

of Cornell University

in Partial Fulfillment of the Requirements for the Degree of

Doctor of Philosophy

by

Vibha Kalra

August 2009

CONTROLLING NANOPARTICLE LOCATION IN BLOCK COPOLYMERS USING EXTERNAL FIELDS: EXPERIMENTS AND SIMULATIONS

Vibha Kalra, Ph.D.

Cornell University 2009

Advances in materials synthesis and fabrication techniques allow an unprecedented control over the creation of novel building blocks such as polymers and particles. The first principle for effective utilization of these building blocks is to create techniques to control their assembly at length scales ranging from nanoscale to macroscopic scale. Hierarchically structured materials have been fabricated by combining the functionalities of block copolymer nanocomposites with the advantages of nanofibers. First, a novel methodology to synthesize block copolymer nanofibers with ordered self assembly has been developed, followed by a systematic study on how this self assembly is altered due to the cylindrical confinement of nanofibers. Then, this self assembly in nanofibers is used as a template to control the spatial distribution of functional nanoparticles. One of the key findings of this work is that a much larger fraction of nanoparticles can be placed (without agglomeration) within nanofibers compared to films of the same materials. To zero in on the mechanism and to understand the thermodynamic and kinetic processes that drive nanoparticle placement in block copolymers during deformation (an important constituent of electrospinning - nanofiber fabrication process), coarse grained molecular dynamics simulations have been conducted. Here, the effect of shear flow on different types of block copolymer/nanoparticle systems has been first studied, followed by a study on effect of elongational flow on various block copolymer nanocomposite systems.

BIOGRAPHICAL SKETCH

Vibha Kalra pursued her undergraduate education in Chemical Engineering at the Indian Institute of Technology (IIT), Delhi, India. During her stay at IIT, she worked on two research projects; production of hydrogen using photochemical reactor and modeling and simulation of proton exchange membrane fuel cells. In her junior year, she got an opportunity to study at the University of British Columbia, Vancouver, Canada for a semester as part of student exchange program. In May 2004, Vibha received her Bachelor of Technology in Chemical Engineering from IIT, Delhi, India. In August of the same year, she began her MS/PhD program in the School of Chemical and Biomolecular Engineering at Cornell University.

To my mom, dad and my sisters, Geetu and Neetu.

ACKNOWLEDGEMENTS

I would like to thank my advisor, Dr. Yong L. Joo, for his help in getting me started with this project, for providing me with the necessary tools to do this work, and for his invaluable ideas and advice throughout my PhD. I am especially thankful to him for being such a supportive advisor and helping me explore new things and learn at every step. I thank Dr. Ulrich Wiesner for his guidance and support for the nanofiber nanocomposite project, for his role on my Special Committee and for all the invaluable discussions of my work. I thank Dr. Claude Cohen for his role on my Special Committee and all the useful discussions of my work. I would like to thank Dr. Fernando Escobedo for his guidance and support for my simulation work.

I would also like to thank the Nanotek Consortium at Kraft Foods, Interdisciplinary Network of Emerging Technology Program at Philip Morris USA, and Samsung Cheil Industries for providing funds to support this work.

I also want to thank all the members of the Joo Research group for their support and helpful advice. I especially want to express gratitude to Jinwoo Lee for synthesis of nanoparticles, Marleen Kamperman and Jung Hun Lee for the synthesis of block copolymers. I would like to thank LaShanda Korley, Sergio Mendez, Brian Pasquini, Jeanne Panels, Seung-Yeon Kang, Huy Nguyen for their help. Finally, I want to thank my family and friends for their support and guidance.

TABLE OF CONTENTS

LIST OF TABLES

LIST OF FIGURES

CHAPTER 1

INTRODUCTION

1.1 Block Copolymers

Block Copolymers are two or more distinct polymeric blocks joint by covalent bonds. The simplest in the family are diblock copolymers, which contain a sequence of type "A" monomers covalently linked to a sequence of type "B" monomers. Similarly, triblock, tetrablock, multiblock copolymers can be synthesized. In addition, one could synthesize block copolymers with branched architectures, such as star-branched block copolymers, where each arm may contain either the same or chemically different block sequences.

1.1.1 Microphase Separation: Current and Potential Applications

Block Copolymers (BCP) attract great interest, both commercial and scientific, due to their tendency to microphase separate into periodic structures under suitable conditions. The size and shape of these structures, and hence the properties of these materials can be precisely controlled by varying the type of blocks, volume fractions, molecular weights and so on. This phenomenon has been extensively studied for both solution and melt via theory [1, 2, 3], experiments [4, 5, 6, 7] and simulations [8, 10, 11, 9].

Figure 1.1 shows the phase diagram of a poly(styrene-*block*-isoprene) (PS-*b*-PI) diblock copolymer melt showing regions of different self-assembled struc-

tures as a function of isoprene volume fraction (f_{PI}) and χN, where χ is the Flory Huggin's Interaction parameter and N is the degree of polymerization [4]. χN represents the incompatibility between A and B and is an inverse function of temperature. As shown in the figure, for low χN values or for very low volume fraction of either block, the diblock copolymer appears in disordered or homogenous state. On the other hand, when the volume fraction of one of the blocks is greater than approximately 0.1 and the system is above a certain critical χN (approximately 10.5), A and B phase separate into micro-domains. The simplest types of domain shapes are spheres, cylinders and lamellae. For an AB diblock copolymer, spheres of A are formed in a matrix of B when f_{PI} is around 0.18-0.23. If the volume fraction of A is around 0.3-0.35, then cylinders of A are formed in matrix of B. For roughly equal amounts of A and B, lamellar morphology is formed. For even higher f_{PI}, inverse phases are formed with B spheres or cylinders in A matrix. Richness of this phase diagram can be greatly enhanced by going over to more complicated architectures such as triblock copolymers, branched copolymers or star-shaped copolymers.

The simplest advantage of such composite materials can be realized when a rubbery major block (such as butadiene or isoprene) is attached to a glassy minor block (such as styrene). The resultant microseparated material exhibits both high rigidity and toughness. Block Copolymers are also used as compatibilizers in a blend of A and B homopolymers, for example. Block copolymers with water-soluble blocks have found uses in the biomedical-pharmaceutical industry. With the recent interest in nanotechnology, block copolymers have gained a lot of attention as templates to fabricate nanostructured materials. This interest stems from the nanometer scale (typically a few tens of nanometers) of self assembled block copolymer structures and the convenient tunability of their size,

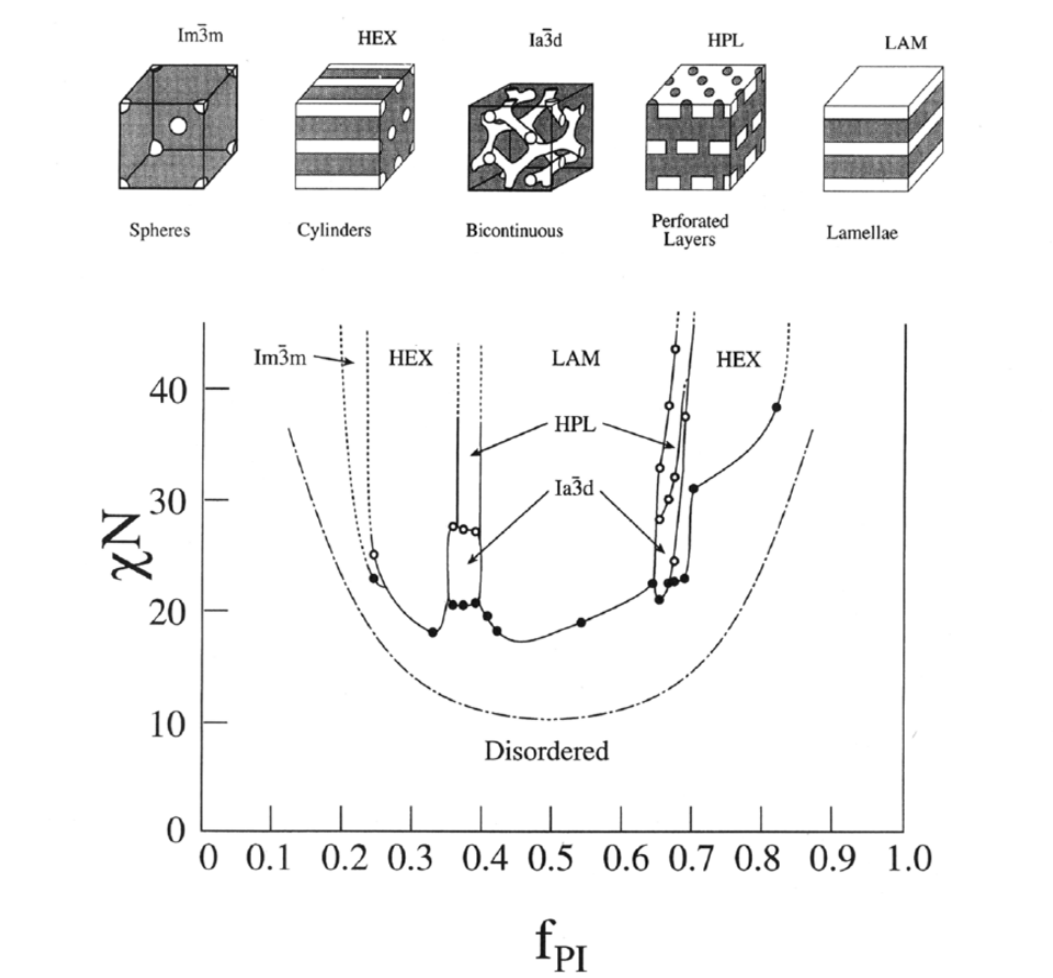

Figure 1.1: Phase Diagram of Poly(styrene-*block*-isoprene) diblock copolymer showing different self assembly structures as a function of PI volume fraction (f_{PI}) and χN [4].

shape and periodicity. For example, by selective dissolution of the minor block, porous materials with tailored pore characteristics could be formed, while, dissolution of the major block can form nanoscale objects. Other current efforts to utilize BCPs in nanotechnologies include nanostructured membranes, photonic crystals, high density information storage media and as templates to spatially guide nanoparticles [6]. The focus of this work has been on utilization of block copolymers as templates to guide nanoparticles and I will talk about this aspect

in more detail in Section 1.1.4.

1.1.2 Rheology and Shear Aligning of Block Copolymers

Block copolymers can be subjected to external fields, such as electric field or shear flow, to induce structural changes. Both of these fields have been demonstrated to produce favorable effects such as inducement of long-range order and order-disorder or order-order structural transitions, as well as the orientation of self-assembled structures. As documented in a review by Hamley, the effects of shear flow on self-assembled spheres, cylinders and lamellae have been well studied [12]. In a more focused review, Wiesner surveyed the current progress in understanding how shear flow affects the lamellae formed by symmetric diblock copolymers [13]. When symmetric BCPs are annealed at a high temperature, lamellae form but usually there is only local ordering and grain boundaries pervade throughout the bulk sample. Shear can help to remove these grain boundaries thus resulting in the formation of large lamellae. For BCPs that are at temperatures slightly above the order-disorder transition, shear can induce the formation of lamellae. Shear is thought to suppress concentration fluctuations and therefore stabilize the lamellae.

Shear-induced switch in lamellar orientation has also been observed. Experimentally, three lamella orientations have been seen as a function of shear rate, shear frequency and temperature: 1) parallel, in which the lamellar layers are parallel to the shearing surface i.e the normal to the lamellar layers is along the velocity gradient direction; 2) perpendicular, in which the normal to the layers is parallel to the vorticity axis and 3) transverse, in which the

normal to the layers is parallel to the flow direction [14]-[21]. Wiesner and co workers did some remarkable studies on effect of large amplitude oscillatory shear flow on symmetric poly(styrene-*block*-isoprene) and found that at low shear frequencies, the lamellae tend to align in a parallel configuration while at higher frequencies, there is a transition to the perpendicular alignment [15, 16, 17, 21] . In addition, they found that the critical shear frequency at which the transition takes place decreases as temperature increases and for temperatures close to T_{ODT}, the low frequency parallel alignment is not seen. Studies on poly(ethylenepropylene-ethylethylene) (PEP-*b*-PEE) also show similar results [23]. For the case of low molecular weight PS-*b*-PI, three regimes have been observed, , parallel at low frequencies, perpendicular at higher frequencies and again parallel at still higher shear frequencies. This is referred to as the 'double flip phenomena' [16] . Wiesner and coworkers suggested that at low shear frequencies, the time scale of shear is much larger compared to the time scale of polymer relaxation, therefore the blocks have enough time to relax and therefore they feel the most stable with the interface parallel to the shearing surface. For higher shear rates, the wave-like distortions or defects in the lamellar layers couple to the vorticity of the the shearing flow and lead to rotation of the layers, destabilizing the parallel orientation and switching to perpendicular alignment [24]. A very interesting analogy suggested by Wiesner and coworkers compares the block copolymer chains during perpendicular alignment to rolling logs, that show less resistance to flow during perpendicular lamallae orientation than in parallel alignment. As I mentioned before, for the case of PS-*b*-PI, parallel alignment reappears at even higher shear frequencies. This transition occurs at ω_c, the frequency beyond which the time scale of molecular relaxation is larger than the time scale of deformation. Therefore

for $\omega > \omega_c$, molecular deformation becomes dominant and therefore governs the alignment. The possible explanation for the reformation of parallel lamellae at very high frequencies is as follows: in PS-*b*-PI, polystyrene block is much more viscous than polyisoprene, i.e. the blocks have a very large mechanical contrast. Thus, the mechanical stresses experienced by styrene are larger than those felt by isoprene. In parallel lamellae, the high stresses in the viscous styrene can be reduced by redistributing the imposed strain preferentially into the less viscous isoprene blocks [25]. The parallel alignment of two contrasting moduli materials during high shear flow is analogous to hard plates (styrene) flowing in a liquid (isoprene) [16]. In another work, Wiesner and coworkers found that the effect of shear frequency and shear amplitude can be lumped into a single parameter, namely the shear rate [16]. This reinforced the hypothesis that the change in time scale of flow with respect to the time scale of block copolymer dynamics is the key to understanding the orientation behavior [13, 20].

The flip of lamellar orientation from parallel to perpendicular alignment has often been associated with a sudden decrease in viscosity. Experimentally, Zipfel *et al.* demonstrated the occurrence of such a phenomena for lyotropic lamellae in a ternary poly(ethylene oxide)-*b*-poly(propylene oxide)-*b*-poly(ethylene oxide) (Pluronic P123)/water/butanol system [26]. In addition, Koppi *et al.* found that the storage modulus for lamellae aligned in a perpendicular direction is always smaller than those aligned parallel to the flow direction [24]. This is equivalent to having a low viscosity for perpendicular lamellae. Such a decrease in viscosity also provides an energetic reason for the flip of orientation from parallel to perpendicular.

The flip of low shear rate parallel lamellae to high shear perpendicular lamel-

lae has also been shown computationally. Again, viscosity has been shown to sharply decrease at the critical shear rate, where this flip occurs. Fraser *et al.* used molecular dynamics simulations to model the shear-induced transition of lamellar layers in a symmetric diblock copolymer [9, 22]. Starting with lamellae in both orientations, they plotted the potential energy as a function of shear rate. They found that shearing the lamellae that were initially perpendicular always resulted in lower potential energy and that the lamellae that were initially parallel converted to the perpendicular arrangement at higher shear rates. In another computational study, Guo studied the effect of segregation strength between the two blocks on the critical shear rate in symmetric diblock copolymer melts [27, 28]. They found that as the segregation between the two blocks decreases, the critical shear rate decreases. This is consistent with the experimental finding where critical shear rate has been shown to decrease as the temperature increases.

1.1.3 Effect of Cylindrical Confinement on Block Copolymers

Recently, some work has been done to obtain novel meso-structures via cylindrical confinement of self assembling materials such as block copolymers. Shin *et al.* [29] and Xiang *et al.* [30] studied the effect of cylindrical confinement on morphology of poly(styrene-*block*-butadiene) (PS-*b*-PBD) in nanoporous alumina membranes. They found that if the pore diameter is large compared to the equilibrium bulk spacing and one component preferentially segregates to the wall, symmetric copolymer forms a concentric cylindrical morphology with alternating cylinders of PS and PBD. If the pore diameter is small and not an integer multiple of the bulk repeat period, the high degree of curvature in a cylin-

drical pore causes frustration of chain packing at the interface forming stacked PS lamellar structures along the axis of the pore. Wu *et al.* [31] studied the confined assembly of silica/copolymer composite in cylindrical pores of varying diameters using alumina nanochannels. They also carried out self consistent field calculations for comparison with experimentally obtained self assembled structures. They found that in asymmetric block copolymers that lie in the hexagonal cylinder regime, the minor block cylinders bend around the pore axis and form helical structures due to confinement. Li *et al.* [32] studied different self assembled structures formed by a diblock copolymer in a cylindrical nanopore. They mapped out a phase diagram using real-space self consistent field theory. They found that mixtures of lamellae and cylinders are formed for certain compositions of diblock copolymers that develop pure cylindrical morphology in the bulk. In this work, we have studied the effect of cylindrical confinement via electrospun nanofibers. These materials provide an easy template for this study compared to nanorods which are not only difficult to handle and process, but are also limited with respect to applications owing to their small aspect ratios.

1.1.4 Block Copolymers as Templates to Guide Functional Nanoparticles

Block copolymers, with their self assembling behavior, have attracted great attention as templates to periodically arrange nanoparticles (NPs) in three dimensions. Having the NPs periodically spaced can lead to synergistic effects of optical [1] and mechanical properties [2, 3], for example, and can potentially be used in novel applications such as magnetic storage media and catalysis [4, 5, 6]. One

of the most interesting examples of such synergy has been demonstrated by Warren *et al.*, where the authors developed high surface area mesoporous catalytic membranes using block copolymer as the template material [33]. They employed block copolymer self-assembly as a means to guide ligand-stabilized platinum nanoparticles. Once the self assembly was formed, they selectively removed the organic material to form mesoporous catalytic membranes with exceptionally high platinum loading.

Numerous studies have been conducted to explore how various system parameters affect the equilibrium location of NPs within block copolymers (BCPs) using experiments, theory and computer simulations. In these studies, researchers varied parameters such as the interaction between the NP and the "A" or "B" monomer of an "AB" diblock copolymer or the size of the NPs (relative to the BCP end to end distance, R_0). In order to experimentally study the effect of interaction between different components of the system, one would typically chemically coat the surface of the nanoparticles with short polymeric ligands. For example, one could synthesize 'selective' nanoparticles by chemically modifying the NP surfaces with ligands of block "A" [34, 35]. In another scenario, one could chemically tether ligands of both blocks "A" and "B" on NP surfaces to fabricate "Non Selective" NPs [35]. As expected, the equilibrium location of the NPs within a block copolymer melt is dictated by thermodynamics, namely, by the balance between enthalpy and entropy. There are enthalpic interactions between the chemically altered NP and the copolymer blocks. The entropic contribution has two prominent components: the translational entropy of the NPs and the configurational entropy of the polymer chains. In line with the above factors, it has been found that small sized selective NPs ($R<<R_{gyr}$; where, R=NP radius, R_{gyr} = Radius of gyration of polymer chains) uniformly disperse

within the preferred block copolymer domain to gain translational entropy [36]. However, when the NP radius is comparable to the R_{gyr}, the polymer chains can lose significant configurational entropy if they try to wrap around the particles. Therefore, the chains push the particles away towards the chain ends (which lie at the center of the preferred domain), causing the NPs to line up at the center of the preferred BCP domain [34, 37, 38]. In addition, interesting results have been found for the case of non selective NPs. Experimentally, Kramer and coworkers have shown gold NPs with surfaces coated half and half with ligands of "A" and "B" respectively. Here the NPs line up at the interface between the two blocks due to enthalpic interactions of different surface ligands with different blocks [34, 35]. As a consequence, they found that the presence of NPs at the interface led to a decrease in the number of *A*-*B* contacts, thereby weakening segregation between the two blocks at the interface. In a recent study that we conducted using molecular dynamics simulations, we modeled our non selective NPs in such a way that the entire NP surface was identical and had equal interaction with both blocks [38]. In this case, one would intuitively expect the NPs to be uniformly dispersed in both blocks. However, the presence of NPs at the interface even in this scenario suggested that reduction in *A*-*B* contacts could be a driving force for such an assembly. Please refer to chapter 6 for more details of this study.

Besides investigating the spatial arrangement of NPs, there is interest in determining how the addition of NPs affects the formation of self-assembled structures or the phase diagram of block copolymers, which in turn will affect the final arrangement of NPs within the polymeric matrix. It has been found that addition of selective NPs leads to higher effective volume fraction of the preferred domain and therefore induces phase transitions between the thermodynami-

cally stable self-assembled structures such as spheres, cylinders and lamellae [37, 39]. The nonselective NPs do not show any dramatic effects on the self-assembled structures except that their presence shifted the χN_{ODT} to a higher value; moreover, for a given χN, above a certain critical NP volume fraction, the structure transitioned from ordered to disordered [37]. This is analogous to a reduction in segregation between "A" and "B" found by Kramer and coworkers [35].

We would like to point out here that most studies on block copolymer nanocomposites in the past have been focused on equilibrium systems. We cannot overstate the importance of studying non equilibrium systems, given that deformation and flow is a constituent of most everyday manufacturing processes. During the manufacturing process a polymer-based melt can be exposed to shearing, compressive, and tensile forces, which may affect the properties of the finished product. Knowledge of how the material behaves in such circumstances is therefore imperative. Moreover, flow has been shown to induce long range order in block copolymer systems, therefore, it is important to understand how nanoparticles behave when we apply deformation/flow to block copolymer templates. In this work, we have integrated both experiments and computational simulations to understand the effect of deformation on assembly of nanoparticles within block copolymers.

1.2 Electrospinning: Nanofiber Fabrication

Electrospinning is a simple, top-down method that has earned enormous attention due to its versatility and capability to produce continuous nanofibers. Typ-

ically, a strong electric field is applied on a droplet of polymer solution/melt. When the electrostatic forces on induced charges on polymer liquid surface exceed surface tension, a thin polymer jet is ejected. The charged jet undergoes strong deformation (strain (extension) rate $\sim 10000\ s^{-1}$) and fast solvent evaporation (~ 200 nl/s) and gets deposited on a grounded collector placed 4-6 inches away as a random non woven mat. We refer the reader to recent reviews that elaborate on the versatility and promise of this distinctive process [40, 41]. Owing to the ultrathin diameters, these fiber mats exhibit large surface area to mass ratios and are attractive materials for high performance separation, sensing and filtration devices, to name a few. Specific surface area ranges from 10 m^2/g for fiber diameters of 500 nm to 1000 m^2/g for diameters around 50 nm.

Recently, some work has been done to fabricate core/sheath nanofibers by coaxially electrospinning two different immiscible liquids through a coaxial spinneret system [42, 43, 44, 40]. Using ethylene glycol and photopolymer as inner and outer jets, Loscertales *et al.* demonstrated the principles and design of stable, coaxial, electrified liquid nanojets towards the production of nanocapsules and nanofibers [42]. Sun *et al.* described the processing of core-shell nano-/mesofibers by coaxial electrospinning of polymer solutions or a combination of polymer solution and melt [43]. They demonstrated that undesirable mixing of the core and shell material can be prevented by slow diffusion rates of the polymer chains as compared to the fast solidification of the polymer jet in the electrospinning process. In the coaxial electrospinning process, the shell serves as a template for formation of fibers from the core material. Therefore, as demonstrated by Yu *et al.* [44], this process is particularly advantageous for core materials that are not viscoelastic enough to form fibers by themselves. Using coaxial electrospinning, Li and Xia produced hollow nanofibers with walls

made of titanium oxide/poly(vinyl pyrrolidone) (TiO_2/PVP) composite or pure titania [45]. Recently, melt coaxial electrospinning has been demonstrated as a versatile method for the encapsulation of solid materials and fabrication of phase change nanofibers [46].

In this work, we have combined the functionalities of block copolymer nanocomposites with the advantages of nanofiber mats (e. g. high surface area, open pore structure, ability to be woven into a fabric) to greatly widen the scope of potential applications. In chapters 2 and 3, we talk about the novel methodology we developed to synthesize block copolymer nanofibers with ordered self assembly, followed by a systematic study on how this self assembly is altered due to the cylindrical confinement of nanofibers. Chapters 4 and 5 discuss the use of internal block copolymer self assembly in nanofibers as a template to control the spatial distribution of functional nanoparticles. One of the key findings of this work is that a much larger fraction of nanoparticles can be successfully placed (without agglomeration) within nanofibers compared to films of the same materials. To zero in on the mechanism and to understand the thermodynamic and kinetic processes that drive nanoparticle placement in block copolymers during deformation (an important constituent of electrospinning - nanofiber fabrication process), coarse grained molecular dynamics simulations have been conducted. Chapters 6 and 7 discuss the effect of shear flow on different types of block copolymer/nanoparticle systems. Lastly, chapter 8 talks about our work on effect of elongational flow on block copolymer/nanoparticle systems and how these effects vary with those under shear flow.

BIBLIOGRAPHY

[1] Bates, F.S.; Fredrickson, G.H. *Annu. Rev. Phys. Chem.* **1990**, 41, 525.

[2] Matsen, M.W.; Schick, M. *Phys. Rev. Lett.* **1994**, 72, 2660.

[3] Fredrickson, G.H.; Bates, F.S. *Annu. Rev. Mater. Sci.* **1996**, 26, 501.

[4] Khandpur, A.K. *et al*. *Macromolecules* **1995**, 28, 8796.

[5] Almdal, K.; Koppi, K.A.; Bates, F.S.; Mortensen, K. *Macromolecules* **1992**, 25, 1743.

[6] Park, C.; Yoon, J.; Thomas, E. L. *Polymer* **2003**, 44, 6725.

[7] Sota, N.; Hashimoto, T. *Polymer* **2005**, 46, 10392.

[8] Hoffman, A.; Sommer, J.; Blumen, A. *J. Chem Phys.* **1997**, 106, 6709.

[9] Fraser, B; Denniston, C; Muser, M.H. *J. Poly. Sc. Part B* **2005**, 43, 970.

[10] Srinivas, G.; Discher, D.; Klein, M.L. *Nature Materials* **2004**, 3, 638.

[11] Groot, R.D.; Madden, T.J.; Tildesley, D.J. *J. Chem. Phys.* **1999**, 110, 9739.

[12] Hamley, I.W. *J. Phys. Condens. Matter* **2001**, 13, R643.

[13] Wiesner, U. *Macromol. Chem. Phys.* **1997**, 198, 3319.

[14] Okamoto, S.; Saijo, K.; Hashimoto, T. *Macromolecules* **1994**, 27, 5547.

[15] Maring, D.; Wiesner, U. *Macromolecules* **1997**, 30, 660.

[16] Leist, H.; Maring, D.; Albrecht, T.T.; Wiesner, U. *J. Chem. Phys.* **1999**, 110, 8225.

[17] Zhang, Y.; Wiesner, U.; Spiess, H.W. *Macromolecules* **1995**, 28, 778.

[18] Gupta, V.K.; Krishnamoorti, R.; Chen, Z.R.; Kornfield, J.A.; Smith, S. D.; Satkowski, M. M.; Grothaus, J. T. *Macromolecules* **1996**, 29, 875.

[19] Gupta, V.K.; Krishnamoorti, R.; Kornfield, J.A.; Smith, S.D. *Macromolecules* **1995**, 28, 4464.

[20] Chen, Z.R.; Kornfield, J.A. *Science* **1997**, 277, 1248.

[21] Zhang, Y.; Wiesner, U. *J. Chem. Phys.* **1995**, 103, 4784.

[22] Fraser, B.; Denniston, C.; Muser, M.H. *J. Chem. Phys.* **2006**, 124, 104902.

[23] Koppi *Phys. Rev. Lett.* **1993**, 70, 1449.

[24] Koppi *J Phys II (France)* **1992**, 2, 1941.

[25] Patel *Macromolecules* **1995**, 28, 4313.

[26] Zipfel, J.; lindner, P.; Tsianou, M.; Alexandridis, P.; Richtering, W. *Langmuir* **1999**, 15, 2599.

[27] Guo, H. *The Journal of Chemical Physics* **2006**, 124, 054902

[28] Guo, H. *The Journal of Chemical Physics* **2006**, 125, 214902.

[29] Shin, K.; Xiang, H.; Moon, S.I.; Kim, T.; McCarthy, T.J.; Russel, T.P. *Science* **2004**, 306, 76.

[30] Xiang, H.; Shin, K.; Kim, T.; Moon, S.I.; McCarthy, T.J.; Russell, T.P. *Macromolecules* **2004**, 37, 5660.

[31] Wu, Y.; Cheng, G.; Katsov, K.; Sides, S.W.; Wang, J.; Tang, J.; Fredrickson, G.H.; Moskovits, M.; Stucky, G.D. *Nature Materials* **2004**, 3, 816.

[32] Li, W.; Wickham, R.A.; Garbary, R.A. *Macromolecules* **2006**, 39, 806.

[33] Warren S.C.; Messina L.C.; Slaughter L.S.; Kamperman M.; Zhou Q.; Gruner S.M.; DiSalvo F.J.; Wiesner U. *Science* **2008**, 320, 1748.

[34] Chui, J. J.; Bumjoon, J. K.; Kramer, E. J.; Pine, D. J. *J Am. Chem. Soc.* **2005**, 127, 5036.

[35] Kim, B.J.; Fredrickson, G.H.; Hawker, C.J.; Kramer, E. J. *Langmuir* **2007**, 23, 7804.

[36] Thompson, R.B.; Ginzburg, V.V; Matsen, M.W.; Balazs, A.C. *Science* **2001**, 292, 2469.

[37] Schultz, A. J.; Hall, C. K.; Genzer, J. *Macromolecules* **2005**, 38, 3007.

[38] Kalra. V.; Mendez, S.; Escobedo, F.; Joo, Y.L. *J. Chem. Phys.* **2008**, 128, 164909.

[39] Huh, H.; Ginzburg, V.V; Balazs, A.C. *Macromolecules* **2000**, 33, 8085.

[40] Li, B.D.; Xia, Y. *Adv. Mater.* **2004**, 16, 1151.

[41] Dzenis, Y. *Science* **2004**, 304, 1917.

[42] Loscertales, I.G.; Barrero, A.; Guerrero, I.; Cortijo, R.; Marquez, M.; Ganan-Calvo, A.M. *Science* **2002**, 295, 1695.

[43] Sun, Z.; Zussman, E.; Yarin, A.L.; Wendorff, J.H.; Greiner, A. *Adv. Mater.* **2003**, 15, 1929.

[44] Yu, J.H.; Fridrikh, S.V.; Rutledge, G. C. *Adv. Mater.* **2004**, 16, 1562.

[45] Li, B.D.; Xia, Y. *Nano Letters*. **2004**, 4, 933.

[46] McCann, J. T.; Marquez, M; Xia, Y. *Nano Letters* **2006**, 6, 2868.

CHAPTER 2

SELF ASSEMBLED STRUCTURES IN ELECTROSPUN POLY(STYRENE-*BLOCK*-ISOPRENE) FIBERS

2.1 Abstract

Formation of various domain shapes in submicron scale fibers of poly (styrene-*block*-isoprene) (PS-*b*-PI) has been investigated via electrospinning. Monodisperse PS-*b*-PI block copolymers with 29 and 53 vol% of PI were synthesized using two-step anionic polymerization and were dissolved in tetrahydrofuran (THF). Solutions of block copolymer with varying concentrations in THF were electrospun, and fibers with average diameters from 200 nm to 5 μm were obtained. Small Angle X-Ray Scattering (SAXS) and Transmission Electron Microscope (TEM) studies revealed that cylindrical and lamellar morphology can be formed in electrospun fibers of 29% and 53% PI copolymers, respectively. We note that these domain structures in fibers are not as well developed as those in films possibly due to the short residence time and strong elongation deformation involved in the electrospinning process. For both systems we find that the *d* spacing in electrospun fibers is smaller than that in the cast film. This could be due to the elongational deformation and fast solvent evaporation during electrospinning. The domain structure of electrospun fibers from the symmetric (53% PI) copolymer exhibits some degree of the effect of fiber morphology such as confinement and curvature due to its high molecular weight. More uniform domain structures in the fibers and increase in *d* spacing are observed after the

annealing process.

2.2 Introduction

Fibers with submicron diameters have been a subject of intensive research due to their large surface area to mass ratio, and are finding uses in filtration, protective clothing, and biomedical applications [1]. These nanofibers can be formed using a relatively simple electrospinning process where a polymer solution or melt is continuously drawn from a syringe needle by a strong electric field. While the strong extension of the viscoelastic jet continuously reduces its diameter, rapid evaporation of solvent solidifies it producing ultra thin fibers. We refer the reader to recent reviews that elaborate on the versatility and promise of this emerging process [2, 3]. Studies on electrospinning, however, have been limited to relatively simple polymeric systems. Casper *et al.* studied the effect of humidity and molecular weight on pore size and distribution on the surface of electrospun polystyrene fibers [4]. Nanofiber formation from complex systems including composites [5, 6] and block copolymers [7, 8, 9] is now beginning to be studied.

Block copolymer solutions and melts are known to self assemble into a variety of nanoscale morphologies including spheres, rods, micelles, lamellae, vesicle tubules, and cylinders depending on the volume fraction and interaction parameter between different blocks [10, 11]. This phenomenon has been extensively studied for both solution and melt via theory [12, 13], experiments [14, 15, 16] and simulations [17, 18, 19, 20]. Numerous studies have focused on the effect of shear on self assembly in block copolymers [12]. Harada *et*

al. obtained highly oriented microstructures in ABABA pentablock copolymer and ABA triblock copolymer using solution extrusion [22]. They reported that the transverse lamellae orientation can be achieved by extruding ABABA pentablock copolymer at high shear rates.

Studies on effect of elongational deformation on block copolymer self assembly have also been conducted in the past. Seguela *et al.* studied elongational deformation mechanism of solution cast films of polybutadiene-hydrogenated SBS block copolymer exhibiting lamellar morphology [23]. They found that lamellae undergo necking and rupture at the yield point. They also reported a reduction in first order Bragg spacing with the increasing longitudinal draw ratio in the neck region. Pakula and coworkers studied the extensional deformation behavior of Styrene-Butadiene-Styrene block copolymer exhibiting cylindrical morphology [24]. They presented a variety of deformation behaviors that occur when the oriented microdomain structure is deformed at various angles to its original orientation. They also found that rupture of domain structures takes place at high extension rates with some evidence of lower domain spacing. Shin *et al.* studied the effect of cylindrical confinement on morphology of PS-*b*-PBD using nanoporous alumina membrane [25]. The copolymer film was annealed at 125^{o}C for it to enter the pores via capillary action and the temperature was kept fixed for 24 hrs to allow the formation of stable equilibrium structures. They found that due to the high degree of curvature imposed in a cylindrical confinement frustration of chain packing occurs at the interface forming stacked PS lamellar structures along the axis of the pore.

Our work focuses on the development of self assembled structures during the formation of sub-micronscale fibers in the electrospinning process.

To the best of our knowledge, there are only a few publications that report on the microphase separation of nanofibers formed by electrospinning block copolymer solutions. Fong *et al.* produced nanofibers from styrene-butadiene-styrene triblock copolymer solution by electrospinning [7]. They observed weak and irregular microphase separation on the surface of electrospun fibers. They found that annealing of fibers allowed the phase domains to become larger. Ma *et al.* recently produced superhydrophobic microphase separated nanofibers from solution of Poly(Styrene-*block*-dimethylsiloxane) block copolymer blended with homopolymers PS in THF and dimethylformamide via electrospinning [8]. They reported the formation of PDMS cylinders in PS matrix via TEM. Self assembly of comb-shaped supermolecules, polystyrene-*block*-poly (4-vinylpyridine) (PS-*b*-P4VP(PDP)-pentadecylphenol(PDP) in electrospun fibers have also been studied [9].

In this paper, we report the formation of self-assembled structures in PS-*b*-PI diblock copolymers of two different compositions. Our experiments are the first to report the structure development in fibers formed by electrospinning symmetric block copolymer solution which forms lamellar morphology. Although previous results have been reported for cylindrical morphology in electrospun fibers, unlike earlier results, we see clear microphase separation via both TEM and SAXS. Furthermore, results on effect of annealing on fiber morphology have also been presented.

2.3 Experimental Methods

2.3.1 Material Synthesis

Two different compositions of PS-*b*-PI diblock copolymers were synthesized and used in the electrospinning study. For the copolymer which we refer to as "IS29", the molecular weights of styrene and isoprene blocks were 32 and 13 kg/mol respectively resulting in a 29 vol% isoprene. For "IS53" copolymer, the PS and PI molecular weights were 74 and 68 kg/mol respectively giving a 53 vol% isoprene. The synthesis of monodisperse PS-*b*-PI block copolymers is accomplished using a two-step living anionic polymerization. Sec-butyllithium is used as an initiator to first polymerize styrene monomer anionically and then to initiate isoprene monomer with this living polystyrene to form a living PS−*b*−PI diblock copolymer. The polydispersity of the polymer obtained by gel permeation chromatography is 1.04 ~ 1.05.

2.3.2 Sample Preparation

PS-*b*-PI copolymers with two different compositions are dissolved in THF. High molecular weight of IS53 copolymer allowed the formation of fibers using 15 to 25 wt% solutions in THF. However, due to the relatively low molecular weight of IS29 copolymer, 30 to 40 wt% solutions were needed to spin non beaded fibers. In the electrospinning unit, block copolymer solution was fed at a constant flow rate of 0.02 ml/min to a syringe by a digitally controlled micropump (Harvard Apparatus, PHD 2000). The tip of the syringe was connected to a high voltage supply (Gamma High Voltage Research, ES-30P), and fibers were spun

at electrical potential of 20 KV using a 24 gauge needle. The distance between the tip of the needle and the grounded collector was kept fixed at about 10 cm.

2.3.3 Characterization

Morphology of electrospun fibers was examined by Scanning Electron Microscopy (SEM) (Leica 440). The structural study was performed through TEM (JEOL 1200EX) and SAXS (Bruker-Axs Nanostar System). In the TEM study electrospun fibers were microtomed at room temperature using a diamond knife. Microtomed fibers were stained with osmium tetroxide vapors (OsO_4). TEM images of both the section along the fiber axis and cross-section were taken using JEOL 1200EX at an accelerating voltage of 120 kV. SAXS data were collected in the 2θ range of 0.1-4^o, in steps of 0.02^o and a scanning rate of 4 sec per point.

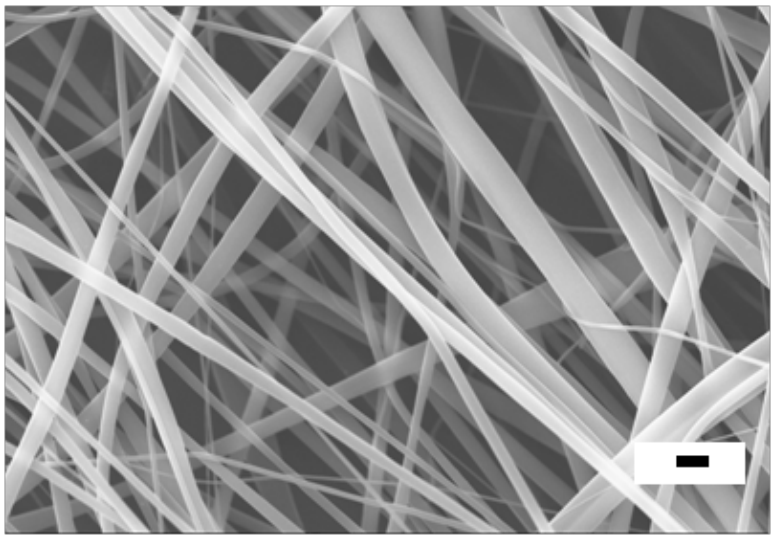

Figure 2.1: SEM image of electrospun IS29 PS-*b*-PI fibers from 30 wt % solution in THF. Scale bar is 3 μm.

2.4 Results and Discussion

Solutions of 30 to 40 wt% of IS29 and 15 to 25 wt% of IS53 copolymer in THF were electrospun, and fibers with average diameters from 200 nm to 5 μm were obtained. A typical scanning electron microscopy (SEM) image of electrospun fibers is shown in Figure 2.1.

2.4.1 IS29 Electrospun Fibers

IS29 PS-*b*-PI bock copolymer film was cast from a 10 wt% solution in THF. Both TEM (Figure 2.2d) and SAXS (Figure 2.3) studies on the cast film show the existence of hexagonally packed PI cylinders in a PS matrix. 30 wt% solution in THF of the same block copolymer was then electrospun using the processing conditions mentioned above. TEM images taken from a microtomed IS29 fiber (Figure 2.2) show some evidence of hexagonal PI cylinders. It is interesting to note that the size of the PI domains is very small as seen in the Figures 2.2a and 2.2b. The possible explanation for largely disordered and short cylinders is the strong elongational deformation during the electrospinning process that causes necking and rupture of the PI cylinders as reported in the literature [24, 26]. Due to the rapid solvent evaporation and short residence time involved in this process the broken cylinders can be frozen in a metastable state before the final equilibrium is reached.

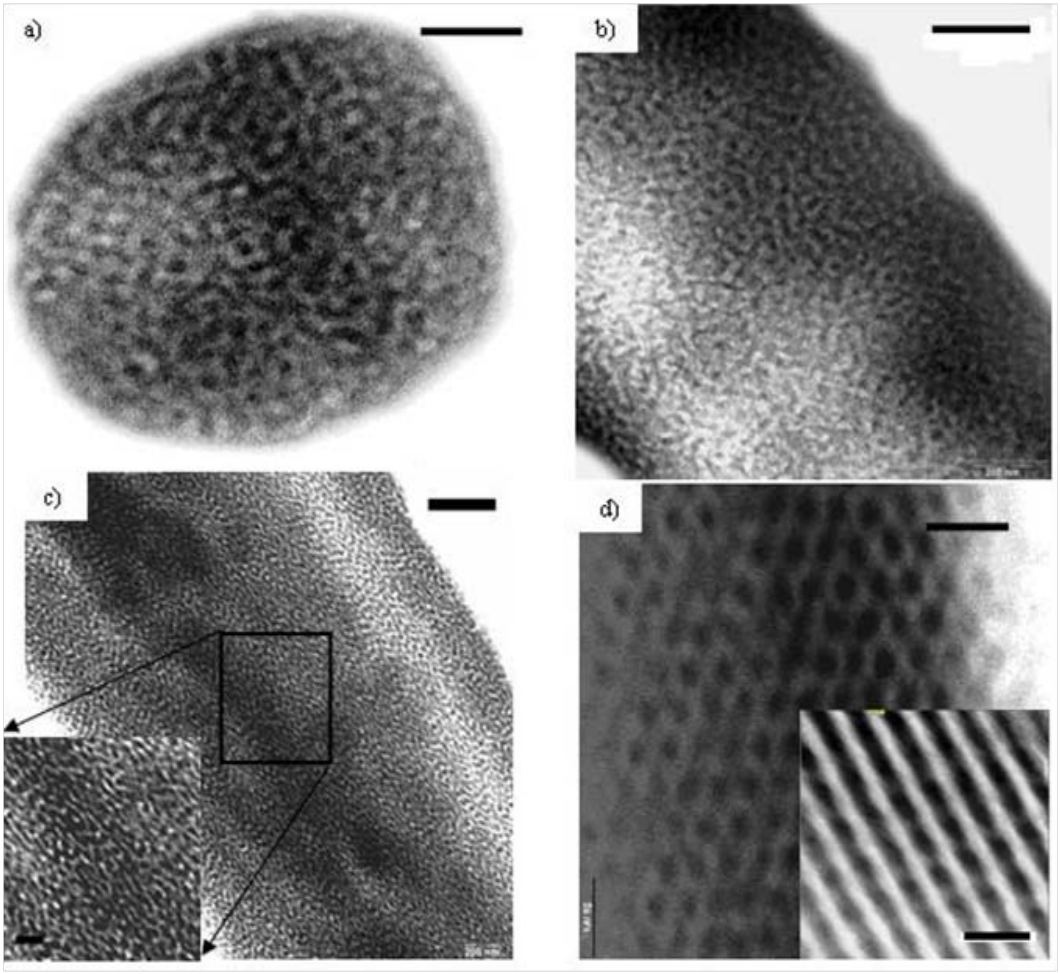

Figure 2.2: TEM images of IS29 system a) cross section of fibers spun from 30wt% solution in THF, scale bar = 100 nm b) along the axis of as-spun fiber, scale bar=200 nm c) along the axis of fiber annealed for 24 hrs at 80°C, scale bar = 200 nm, inset scale bar=50 nm and d) film cast from 10wt% solution in THF, side view and top view scale bars = 50 nm.

SAXS experiments were performed on non-woven fiber mats and results are shown in Figure 2.3. Presence of a well defined first order peak confirms microphase separation between the two blocks. However, a weak second order peak at a ratio of $\sqrt{3}$ indicates the presence of weakly segregated domains and largely disordered morphology. For example, two different SAXS patterns for

as-spun IS29 fibers taken at different regions of the same sample are shown in Figure 2.3. Presence of the second order peak in only one curve shows that the electrospun fibers have regions of both ordered cylindrical domains and disordered PI domains in the PS matrix. It is also worth noting that the *d* spacing between isoprene cylinders is smaller in fibers than in films. A similar reduction in *d* spacing was seen by Pakula *et al.* [24] who studied the elongational deformation behavior of Styrene-Butadiene-Styrene triblock copolymer with a cylindrical morphology, while Kim *et al.* [27] observed a smaller domain spacing as the solvent evaporation rate was increased in thin films of 100 nm in thickness. The decrease in *d* spacing from the equilibrium bulk value in our system could be a combined effect of both extensional deformation and rapid solvent evaporation.

To investigate the effect of annealing on domain structures, electrospun fibers were annealed at 80°C for 24 hours and 48 hrs. TEM image of a longitudinal cross section of 24 hr annealed fiber is shown in Figure 2.2c. The annealed fiber shows some evidence of longer cylinders with a tendency to align along the fiber axis. Due to the confinement of the fiber curvature, the PI domains are not able to reorient themselves completely and a substantial annealing effect on structure development is seen in the SAXS data only at a temperature of 110°C as shown in Figure 2.3. The annealing effect is seen with the emergence of a higher order peak indicating the beginning of formation of strongly segregated domains. Annealing at temperatures above 90°C helps release the external stresses imposed during electrospinning and the domain spacing of the original undeformed state is recovered, while the fiber morphology is not fully preserved above 110°C. The *d* spacing of both as-spun and annealed IS29 fibers at various temperatures is summarized in Table 2.1. It is observed that

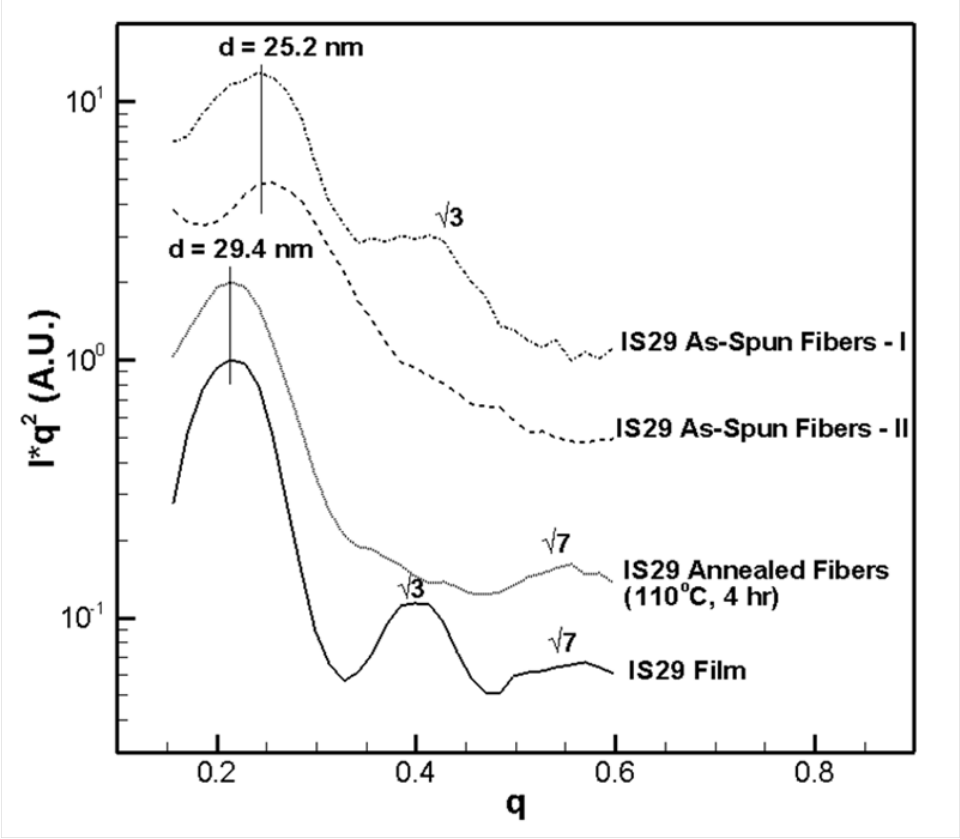

Figure 2.3: SAXS patterns of IS29 fibers and film. Fibers were spun using a 30 wt% solution in THF. Two different SAXS curves for as-spun IS29 fibers taken at different regions of the same sample are shown.

the *d* spacing increases with the degree of annealing and eventually recovers that of the film.

Table 2.1: Domain spacing obtained for IS29 fibers on annealing at various temperatures.

	As Spun	80°C, 24 hrs	100°C, 4 hrs	110°C, 4 hrs	Film
d spacing (nm)	25.2	25.2	27.6	29.4	29.4

2.4.2 IS53 Electrospun Fibers

Similar studies were done on IS53 copolymer. Films were cast from a 10 wt% solution in THF and lamellar morphology was obtained via TEM as shown in Figure 2.4. 15 to 25 wt% polymer solutions in THF were electrospun. TEM images of the cross section of fibers spun from 25 wt% IS53 copolymer in THF are shown in Figure 2.4. We find two different morphologies in as spun fibers (Figures 2.4a and 2.4b). While we see alternating parallel layers of PI and PS at the edges of the fiber cross section in one type of morphology (Figure 2.4a), we find some evidence of alternating segments of PI and PS in the other with PI located at the outer walls due to its lower surface energy (Figure 2.4b). However, both morphologies show disordered PI domains in the center of the cross section due to high deformation rates and short residence time during electrospinning. The domain spacing of fibers is substantially lower than that of the film. One possible explanation for this is the strong confinement and curvature effect of the fiber morphology due to the relatively large equilibrium domain spacing of IS53 copolymer (~ 62 nm). This along with the other effects of elongation and rapid solvent evaporation causes a compression of the lamellar morphology. However, the reason for such a small domain spacing in fibers is still not well understood.

We annealed the IS53 fibers at 90^{o}C for 12 hrs and TEM images of fiber cut across the cross section and along the fiber axis are shown in Figures 2.4 c) and d), respectively. Only one kind of morphology which shows the emergence of alternating concentric rings of PI and PS with PI on the outer walls was found in the annealed fibers. In addition, the annealed fibers show a better contrast between the blocks indicating stronger segregation.

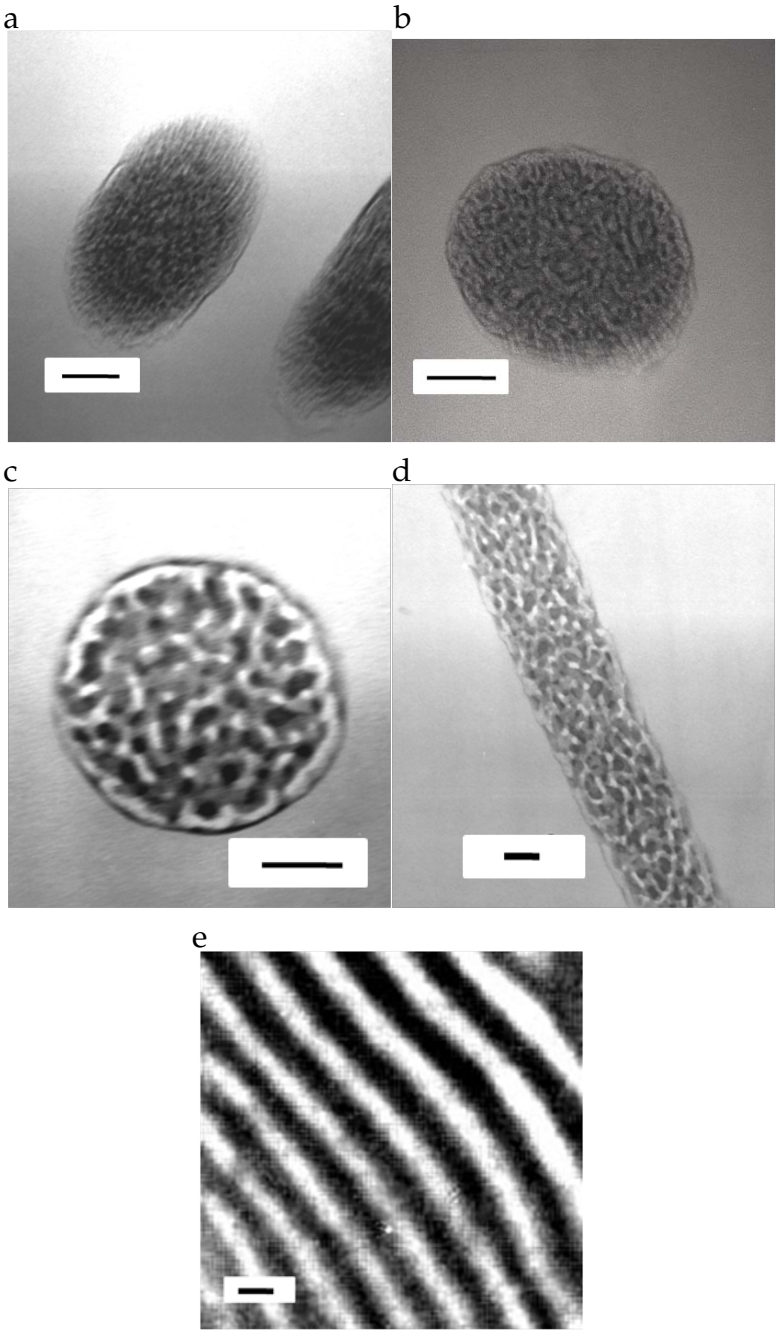

Figure 2.4: TEM images of IS53 copolymer a) and b) two cross sections with different domain structures of fiber spun from 25wt% solution in THF, c) cross section of fiber annealed at 90°C for 12 hrs. d) along the axis of fiber annealed at 90°C for 12 hrs. e) film cast from 10 wt% solution in THF. All scale bars are 100 nm.

However, the morphology is still largely disordered in the center. TEM image along the fiber axis shows small broken domains possibly due to high extensional deformation during electrospinning. SAXS experiments were performed on IS53 fiber mats and results are shown in Figure 2.5. Again, the presence of a well defined first order peak confirms microphase separation between the two blocks. However, no clear second order peak in as-spun fibers indicates the presence of weakly segregated domains and largely disordered morphology as in the IS29 system. It is also observed that the *d* spacing between isoprene domains is smaller in fibers than in films. To investigate the effect of annealing on domain structures, electrospun fibers were annealed at 100°C for 12 hours. The annealing effect is seen with the emergence of a higher order peak indicating the beginning of formation of strongly segregated domains, but the PI domains are not able to reorient themselves completely due to the confinement of the fiber curvature and relatively lower annealing temperatures. Annealing at 100°C for 12 hours gives rise to only a small increase in the domain spacing which is still substantially lower than the bulk repeat period.

2.5 Conclusion

We have presented evidence of microphase separation such as cylindrical and lamellar morphology in electrospun PS-*b*-PI nanofibers via TEM and SAXS studies. However, the domains in electrospun fibers are not well ordered due to the fast solvent evaporation and strong elongational deformation involved in the electrospinning process. IS29 fibers show smaller domain spacing than the corresponding film. However, the microdomains relax back to their equilibrium spacing on annealing. For IS53 copolymer, the bulk repeat period is very large

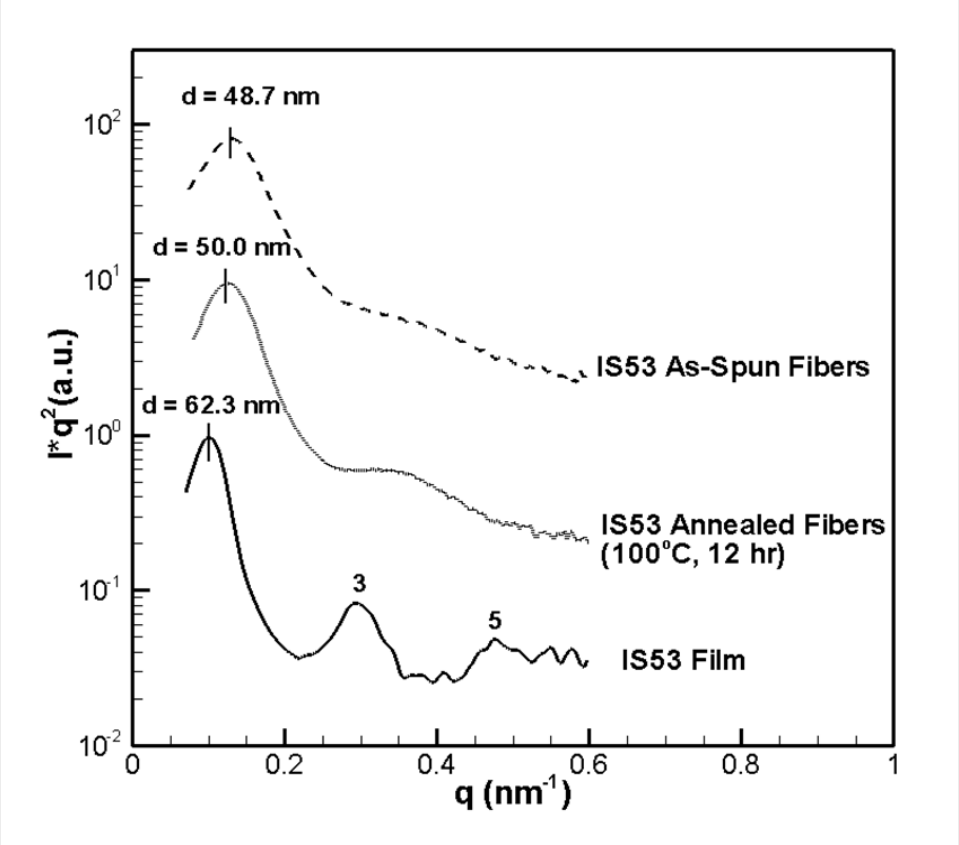

Figure 2.5: SAXS patterns of IS53 fibers and film. Fibers were spun using a 25 wt% solution in THF.

due to its high molecular weight making the effect of cylindrical confinement due to fiber morphology substantial. This leads to an extremely small domain spacing in fibers as compared to the IS53 film. Although the *d* spacing increases on annealing these fibers, it is not able to relax back to its equilibrium. A comprehensive annealing study at different temperatures and various time ranges to obtain more uniform microdomain structures for both cylindrical and lamellar morphology is underway.

BIBLIOGRAPHY

[1] Fong, H.; Reneker, D.H. *Structure Formation in Polymeric Fibers*, Hanser Gardner Publications, Munich, 2001.

[2] Dzenis, Y. *Science* **2004**, 304, 1917.

[3] Li, B.D.; Xia, Y. *Adv. Mater*. **2004**, 16, 1151.

[4] Casper, C.L.; Stephens, J.S.; Tassi, N.G.; Chase, D.B.; Rabolt, J.F. *Macromolecules* **2004**, 37, 573.

[5] Fong, H.; Liu, W.; Wang, C.S.; Vaia, R.A. *Polymer* **2002**, 43, 775.

[6] Zhou, H.; Kim, K.W.; Giannelis, E.P.; Joo, Y.L. *Polymeric Nanofibers*, ACS Symposium Series Book, volume 198, 2006.

[7] Fong, H.; Reneker, D.H. *J. Poly. Sc. Part B* **1999**, 37, 3488.

[8] Ma, M.; Hill, R.M.; Lowery, J.L.; Fridrikh, S.V.; Rutledge, G.C. *Langmuir* **2005**, 21, 5549.

[9] Ruotsalainen, T. *et al. Adv. Mater*. **2005**, 17, 1048.

[10] Khandpur, A.K. *et al. Macromolecules* **1995**, 28, 8796.

[11] Bates, F.S.; Fredrickson, G.H. *Annu. Rev. Phys. Chem.* **1990**, 41, 525.

[12] Matsen, M.W.; Schick, M. *Phys. Rev. Lett.* **1994**, 72, 2660.

[13] Fredrickson, G.H.; Bates, F.S. *Annu. Rev. Mater. Sci.* **1996**, 26, 501.

[14] Almdal, K.; Koppi, K.A.; Bates, F.S.; Mortensen, K. *Macromolecules* **1992**, 25, 1743.

[15] Park, C.; Yoon, J.; Thomas, E. L. *Polymer* **2003**, 44, 6725.

[16] Sota, N.; Hashimoto, T. *Polymer* **2005**, 46, 10392.

[17] Hoffman, A.; Sommer, J.; Blumen, A. *J. Chem Phys.* **1997**, 106, 6709.

[18] Fraser; Denniston; Muser, *J. Poly. Sc. Part B* **2005**, 43, 970.

[19] Srinivas, G.; Discher, D.; Klein, M.L. *Nature Materials* **2004**, 3, 638.

[20] Groot, R.D.; Madden, T.J.; Tildesley, D.J. *J. Chem. Phys.* **1999**, 110, 9739.

[21] Hamley, I.W. *J Phys.: Condens. Matter* **2001**, 13, 643.

[22] Harada, T.; Bates, F.S.; Lodge, T. *Macromolecules* **2003**, 36, 5440.

[23] Seguela, R.; Homme, J.P. *Macromolecules* **1981**, 14, 197.

[24] Pakula, T.; Saijo, K.; Kawai, H.; Hashimoto, T. *Macromolecules* **1985**, 18, 1294.

[25] Shin, K.; Xiang, H.; Moon, S.I.; Kim, T.; McCarthy, T.J.; Russel, T.P. *Science* **2004**, 306, 76.

[26] Daniel, C.; Hamley, I.W.; Mortensen, K. *Polymer* **2000**, 41, 9239.

[27] Kim, G.; Libera, M. *Macromolecules* **1998**, 31, 2569.

CHAPTER 3

CONFINED ASSEMBLY IN COAXIALLY ELECTROSPUN BLOCK COPOLYMER FIBERS

3.1 Abstract

Coaxial nanofibers with poly(styrene-*block*-isoprene) (PS-*b*−PI) core enveloped by silica shell have been electrospun. Thermally stable silica sheath allows us to anneal the fibers well above the glass transition temperature without the loss of fiber integrity to obtain well-ordered confined block copolymer selfassembled structures A transition of morphology from stacked lamellar discs to alternating concentric cylinders of PI and PS is shown for symmetric copolymers on annealing via Transmission Electron Microscopy (TEM). Finally, pure PS-*b*−PI fiber mats with confined assembly have been obtained by removing the silica skin layer via the treatment with NaOH solution. This coaxial electrospinning scheme of block copolymer and thermally stable silica together with annealing and silica etching provides a useful means to fabricate continuous block copolymer nanofibers with unique self-assembled structures.

3.2 Introduction

Electrospinning has received great attention in recent years as a simple process to produce submicron scale fibers. The process involves continuous stretching

of polymer solution or melt in the presence of strong electric field forming ultra thin fibers. Numerous amount of work is being done on controlling the diameter, morphology, and spatial alignment of electrospun nanofibers [1, 2]. Unlike other 1D nanostructures like nanowires and nanotubes, nanofibers exhibit a wide range of unique properties making them far more attractive for various applications such as filtration, catalysis, sensing, protective clothing, and tissue engineering scaffolds [3]. Being a continuous process, electrospinning can produce extremely long fibers comparable to those formed via conventional mechanical drawing and spinning techniques. Nanofiber mats exhibit extremely high surface to mass ratios greatly improving their efficiency for catalysis and filtration [2]. Another fascinating feature of this process is that it can be applied to a wide variety of nanostructured materials. Bognitzki *et al*. fabricated sub micron scale fibers by electrospinning ternary solutions of polylactide and polyvinylpyrrolidone [4]. They found that the fibers displayed an internal phase morphology and by selectively removing one phase they obtained highly porous fibers. However, these morphologies were largely controlled by rapid phase separation and rapid solidification of the polymer jet and no method for control of these morphologies was demonstrated. In the present study we utilize this simple process to fabricate block copolymer (BCP) nanofibers. BCP solutions and melts are known to self assemble into a variety of nanoscale morphologies including spheres, rods, micelles, lamellae, vesicle tubules, and cylinders depending on the volume fraction and interaction parameter between different blocks. We have been able to produce macroscale length fibers with a few hundred nanometer diameters exhibiting internal structures in the range of only tens of nanometers [5, 6]. Such materials, we believe, can combine the unique properties of continuous nanofibers and block copolymer self assembly

for use in a variety of applications of nanostructured materials.

BCP self assembly has attracted increasing interest in recent years for applications in nanotechnology [7]. Precise control over the size, shape and periodicity of these nanoscale microdomains is the key factor in providing opportunities for realization of nanoscale systems. Various methods including shear and elongational deformation, compressional deformation, electric fields and temperature gradients have been utilized to induce orientation of microdomains. To our knowledge, shear flow has been most extensively studied as a simple means to induce phase transitions and orient self-assembled structures in block copolymers [8, 9]. The phenomenon of flow induced alignment of lamellar block copolymers is very well studied in the bulk system [10, 11, 12]. Three different orientations of lamellar morphology, namely, parallel [13], perpendicular and transverse [14, 15, 16] have been obtained as a function of shear rate, shear frequency and temperature. We refer the reader to a review paper [7] that elaborates on the various methods to control BCP microdomains and the potential applications of these domains as nanometer scale membranes, templates for fabrication of a variety of nano-objects, and as templates for fabrication of high density information storage media.

Recently, some work has been done to obtain novel self-assembled structures as an effect of confinement of self assembling materials in 1D nanostructures like nanorods and nanowires. Shin *et al.* [17] and Xiang *et al.* [18] studied the effect of cylindrical confinement on morphology of poly(styrene-*block*-butadiene) (PS-*b*-PBD) in nanoporous alumina membranes. They found that if the pore diameter is large compared to the equilibrium bulk spacing and one component preferentially segregates to the walls, symmetric copolymer forms a concentric

cylindrical morphology with alternating cylinders of PS and PBD. If the pore diameter is small and not an integer multiple of the bulk repeat period, the high degree of curvature imposed in a cylindrical confinement causes frustration of chain packing at the interface forming stacked PS lamellar structures along the axis of the pore. Wu *et al.* [19] studied the confined assembly of silica–copolymer composite mesostructures in cylinders of varying diameters using alumina nanochannels. They also carried out self consistent field calculations for comparison with experimentally obtained self assembled structures. However, potential applications of these distinctive nanostructures are limited by their short length scale and difficulty in separating nanorods from supporting BCP films.

In this effort to obtain novel morphologies in confined yet continuous and long nanostructures, we recently reported the structure development in PS-*b*–PI nanofibers [20] formed via electrospinning. However, the microdomains in as-spun fibers are largely disordered because of the strong elongational deformation [21, 22, 23] and rapid solvent evaporation [24] during electrospinning. Fong and Reneker [25] produced nanofibers from styrene-butadiene-styrene triblock copolymer solution by electrospinning. They observed weak and irregular microphase separation on the surface of electrospun fibers. Although, these structures are seen to improve on annealing, the domains remain largely disordered. Other works [26, 27] on microphase separation in block copolymer nanofibers also report the formation of irregular morphology. It is extremely difficult to obtain long range order in these electrospun fibers because annealing the fibers above the glass transition temperature of the block copolymer results in the loss of fiber morphology. To overcome this limitation of thermal treatment, coaxial fibers where the PS-*b*–PI core is enveloped by a thermally stable silica sheath

are fabricated in the current study, thereby allowing us to anneal the fibers at high temperatures. Pure PS-*b*−PI fiber mats with well-ordered, confined assembly have been obtained by removing the silica skin layer via the treatment with NaOH solution.

Recently, some work has been done to fabricate core/sheath nanofibers by coaxially electrospinning two different immiscible liquids through a coaxial spinneret system [28, 29, 30]. Using ethylene glycol and photopolymer as inner and outer jets, Loscertales, *et al.* demonstrated the principles and design of stable, coaxial, electrified liquid nanojets toward the production of nanocapsules and nanofibers [28]. Sun *et al.* described the processing of core-shell nano-/mesofibers by coaxial electrospinning of polymer solutions or a combination of polymer solution and melt [29]. They demonstrated that undesirable mixing of the core and shell material can be prevented by slow diffusion rates of the polymer chains as compared to the fast solidification of the polymer jet in the electrospinning process. Li and Xia produced hollow nanofibers with walls made of titanium oxide/poly(vinyl pyrrolidone) (TiO_2/PVP) composite or pure titania using coaxial electrospinning [30]. In the coaxial electrospinning process, the shell serves as a template for formation of fibers from the core material. Therefore, this process is particularly advantageous for core materials that are not viscoelastic enough to form fibers by themselves.

In the current study, we utilize coaxial electrospinning technique to obtain block copolymer nanofibers with highly ordered lamellar morphologies. Stacked lamellar structures perpendicular to the fiber axis and alternating concentric cylinders of PI and PS parallel to the fiber axis are first obtained via different degrees of annealing of block copolymer fibers with a silica envelope.

Then the silica shell is dissolved by treatment with NaOH at room temperature to fabricate pure PS-*b*−PI nanofibers with confined self assembly.

3.3 Experimental Methods

Two different molecular weights of nearly symmetric PS-*b*-PI diblock copolymers were synthesized and used in the coaxial electrospinning study. For the copolymer which we refer to as "IS62-27K", the molecular weights of styrene and isoprene blocks were 11,200 and 15,500 g/mol respectively resulting in a 62 vol% isoprene. For "IS53-143K" copolymer, the PS and PI molecular weights were 74,500 and 68,400 g/mol respectively giving a 53 vol% isoprene.

The synthesis of monodisperse PS-*b*-PI block copolymers, IS53-143K and IS62-27K is accomplished using a two-step living anionic polymerization. Sec-butyllithium is used as an initiator to first polymerize styrene monomer anionically and then to initiate isoprene monomer with this living polystyrene to form a living PS−*b*−PI diblock copolymer. The polydispersity of two copolymers obtained by gel permeation chromatography is 1.04.

Figure 3.1 shows a schematic of the experimental set-up we used for electrospinning coaxial fibers. Unlike the conventional electrospinning set-up, we have 2 syringes (5 ml volume) containing core and sheath material and each syringe is connected to a separate needle. The needles are placed one inside the other to form a coaxial spinneret system. The core needle protrudes from the shell needle by about 0.5 mm to allow efficient viscous entrainment of the inner material. Both syringes were connected to an individual micropump (Harvard Apparatus, PHD 2000) to control the flow rate of both materials independently.

The tip of the needle was connected to a high voltage supply (Gamma High Voltage Research, ES-30P) and fibers formed were collected on a grounded collector.

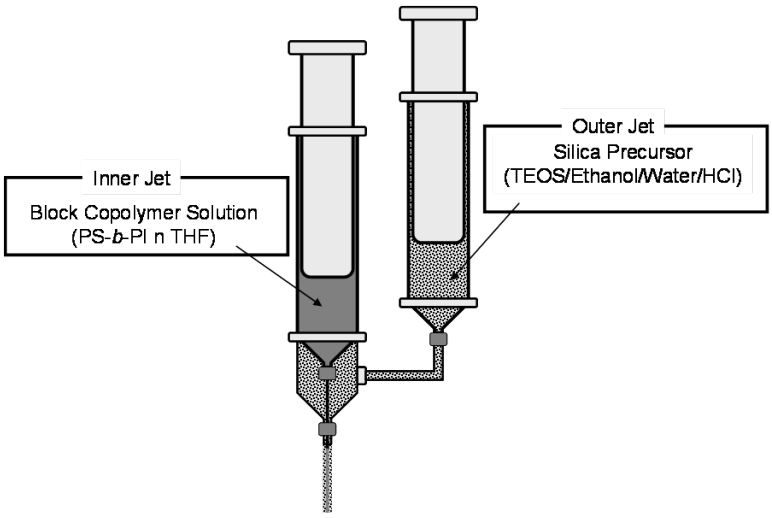

Figure 3.1: SEM image of electrospun IS29 PS-b-PI fibers from 30 wt % solution in THF. Scale bar is 3 μm.

For the core material PS-*b*-PI copolymers are dissolved in THF. We typically use a polymer concentration of 25 wt% for the high molecular weight IS53-143K copolymer and a concentration of 40 wt% for the low molecular weight IS62-27K copolymer. The solution used for the sheath material in the present study is prepared using sol-gel synthesis. Silica sol-gel is prepared by combining a silica precursor such as tetra(ethyl)ortho-silicate (TEOS) with ethanol. Water containing a small amount of catalyst such as HCl is added drop by drop, under vigorous mixing, to the TEOS/ethanol solution to control the hydrolysis and condensation reactions. The overall molar ratio of TEOS:ethanol:water:HCl was 1:2:2:0.01. This solution is then kept in the oven at 50^{o}C for 4-5 hours to accelerate the sol-gel synthesis reaction. As the sol-gel reaction takes place, the viscosity of the solution increases making it spinnable at a viscosity of about

10 Poise. This sol-gel precursor has been used to produce electrospun silica nanofibers without using any polymer binder [32]. Fibers were spun room temperature with about 50% humidity at an electrical potential of 20 kV. The distance between the tip of the needle and the grounded collector was kept at 4-6 inches. Different solution flow rates were used to produce coaxial fibers from two copolymer systems in this work. For the high molecular weight IS53-143K copolymer the flow rate of 0.005 ml/min was applied for both inner and outer jets, while 0.015 ml/min and 0.02 ml/min were used for the inner and outer jet, respectively for the low molecular weight IS62-27K copolymer. Finally, coaxially electrospun PS-b-PI/silica fibers after the annealing process (at 175^{o}C for 24 hrs) were treated with 1M NaOH solution at room temperature for 1 hr to selectively remove the silica skin layer and thus to obtain pure PS-*b*-PI fiber mats with confined assembly.

Morphology of electrospun fibers was examined by Scanning Electron Microscopy (SEM) (Leica 440). The structural study was performed through Transmission Electron Microscopy (TEM). In the TEM study electrospun fibers were embedded first in an epoxy matrix and microtomed at room temperature using a diamond knife. Microtomed fibers were stained with osmium tetroxide (OsO_4) vapors. TEM images of both section along the fiber axis and cross-section were taken using JEOL 1200EX at an accelerating voltage of 120 kV.

3.4 Results and Discussion

Figure 3.2 shows SEM images of coaxial fibers electrospun using IS53-143K solution in THF for the core and silica precursor for the shell material. The diame-

ters of coaxially spun fibers range from 300 nm to 1 μm., As seen in Figure 3.2b, the fiber morphology is preserved due to the presence of silica as a sheath even after annealing at 175^{o}C for 48 hours. Although, some of the fibers appear to be hollow in the SEM image due to the leakage of the polymer from the edges of the cut fibers during annealing, we see in the TEM studies later that the polymer core remains largely intact inside the thermally stable silica shell. It is observed that the thickness of the silica sheath is about 10 to 20% of coaxially spun fibers.

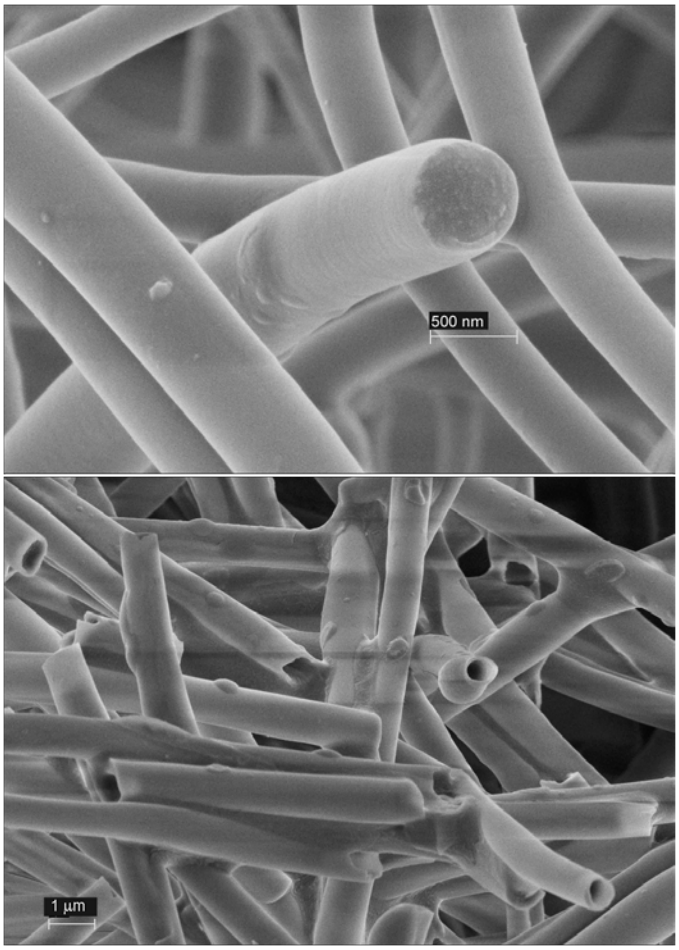

Figure 3.2: SEM image of coaxially electrospun PS-*b*-PI fibers: a) as-spun fibers, b) annealed at 175^{o}C for 48 hours.

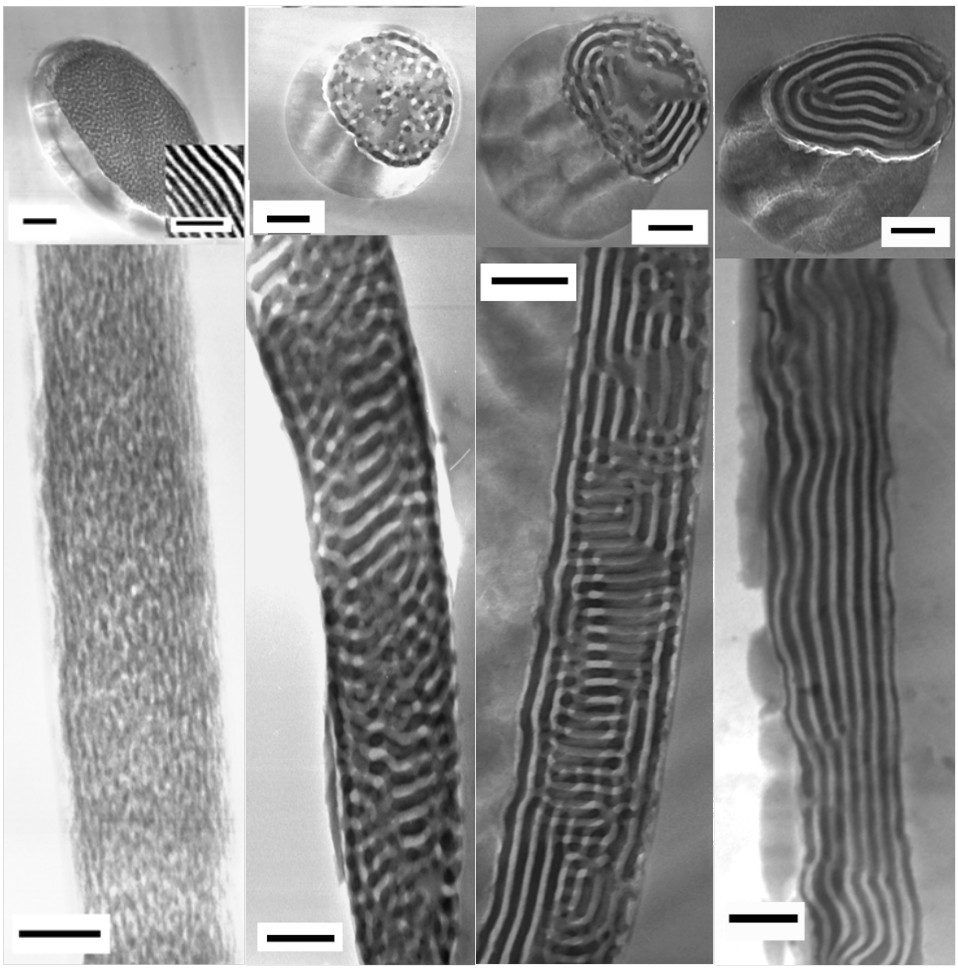

Figure 3.3: TEM images of coaxially spun IS53-143K fibers a) as spun fibers, inset is TEM image of film surface (equilibrium domain spacing ~ 60 nm), b) stacked PS lamellar structure after annealing at 125^{o}C for 24 hrs, c) transition to alternating concentric cylinder morphology after annealing at 175^{o}C for 24 hrs, d) Parallel morphology on annealing at 175^{o}C for 50 hrs. Top row is the cross sections normal to the fiber axis and bottom row is the ones parallel to fiber axis. The dark areas are stained PI domains, while light areas are PS domains. All scale bars in each image including the inset are 200 nm.

The internal structures in as-spun coaxial fibers of IS53-143K copolymer both along the fiber axis and perpendicular to the axis are shown in the TEM images in Figure 3.3a. The copolymer has a clear microphase separation, but the do-

mains are broken and largely disordered due to high elongational deformation and rapid solvent evaporation during electrospinning. Some evidence of alignment of these broken lamellae is seen along the fiber axis. As expected, these structures are very similar to those obtained in uniaxially electrospun fibers of PS-*b*-PI [20]. The fibers were then annealed at 125^{o}C for 24 hrs and SEM images were taken to confirm that fiber integrity was maintained and minimal leakage of polymer was seen through the silica envelope. The TEM image of the longitudinal section of annealed fiber shows a stacked PS lamellar structure with PI along the edges of the core of the fiber due to its low surface energy (Figure 3.3b). The corresponding cross-sectional image shows an outer PI ring consistent with the PI edges in the longitudinal image. However, it is very difficult to cut the fiber normal to the axis and exactly along the lamellar disc, and thus the cross sectional image shows sections of multiple disks along the radial direction. We note that this transverse lamellar disk structure is retained even after annealing the fibers at the same temperature for 5 days. To further investigate the development of morphology, we annealed the fibers at a temperature of 175^{o}C (yet below T_{ODT}). The fibers were annealed for different times between 24 hrs to 50 hrs at this temperature and the TEM images are shown in Figure 3.3c and 3.3d. The longitudinal section shows a mixture of stacked lamellar disc morphology and alternating concentric cylinders of PS and PI (parallel morphology) along the fiber axis (Figure 3.3c). The cross sectional image shows concentric rings of PS and PI on the outer edges consistent with the parallel lamellae seen in the longitudinal section. The emergence of pure parallel morphology is observed in the fibers after longer annealing time, 50 hours (Figure 3.3d). The corresponding cross sectional image shows eight alternate concentric rings of PI and PS. These images confirm a transition of lamellae orientation from stacked discs

perpendicular to the fiber axis (transverse orientation) to blocks oriented parallel to the axis (axial orientation) with increasing the degree of annealing .

Similar studies were done on the low molecular weight IS62-27K copolymer. Figure 3.4 shows the TEM images of various coaxially electrospun IS62-27K copolymer fibers. It should be noted that it was very difficult to obtain uniform uniaxial fibers in the submicron diameter range via conventional uniaxial electrospinning because of the low molecular weight and high PI content of the copolymer. No annealing study was conducted on these fibers due to the collapse of fiber morphology at 80^{o}C. Figure 3.4a shows the TEM image of microtomed section of a uniaxially electrospun fiber whose diameter is larger than 3 μm. Coaxial electrospinning scheme was utilized to spin uniform, thin fibers using the block copolymer solution as the inner jet and silica precursor as the outer jet. Here, the outer jet silica precursor solution acts as a template to draw the polymer solution forming submicron scale fibers. TEM images of as-spun coaxial fibers (Figure 3.4b) show disordered structures similar to those in uniaxial fibers. The fibers were annealed at 125^{o}C and TEM images were taken at different annealing times. This copolymer seems to follow the same transition in the alignment of each layer as the IS53-143K except for a much shorter time scale of transition because of its low molecular weight and thus its higher chain mobility. Stacked disc morphology was obtained on annealing the fibers at 125^{o}C for only a few hrs (Figure 3.4c) and on annealing for 24 hrs at the same temperature, we obtain a complete transition to the alternating PS and PI concentric cylinder morphology (Figure 3.4d). Consistent with the ratio of the fiber core diameter and the equilibrium domain spacing of the copolymer, we obtain eight concentric rings of PI and PS.

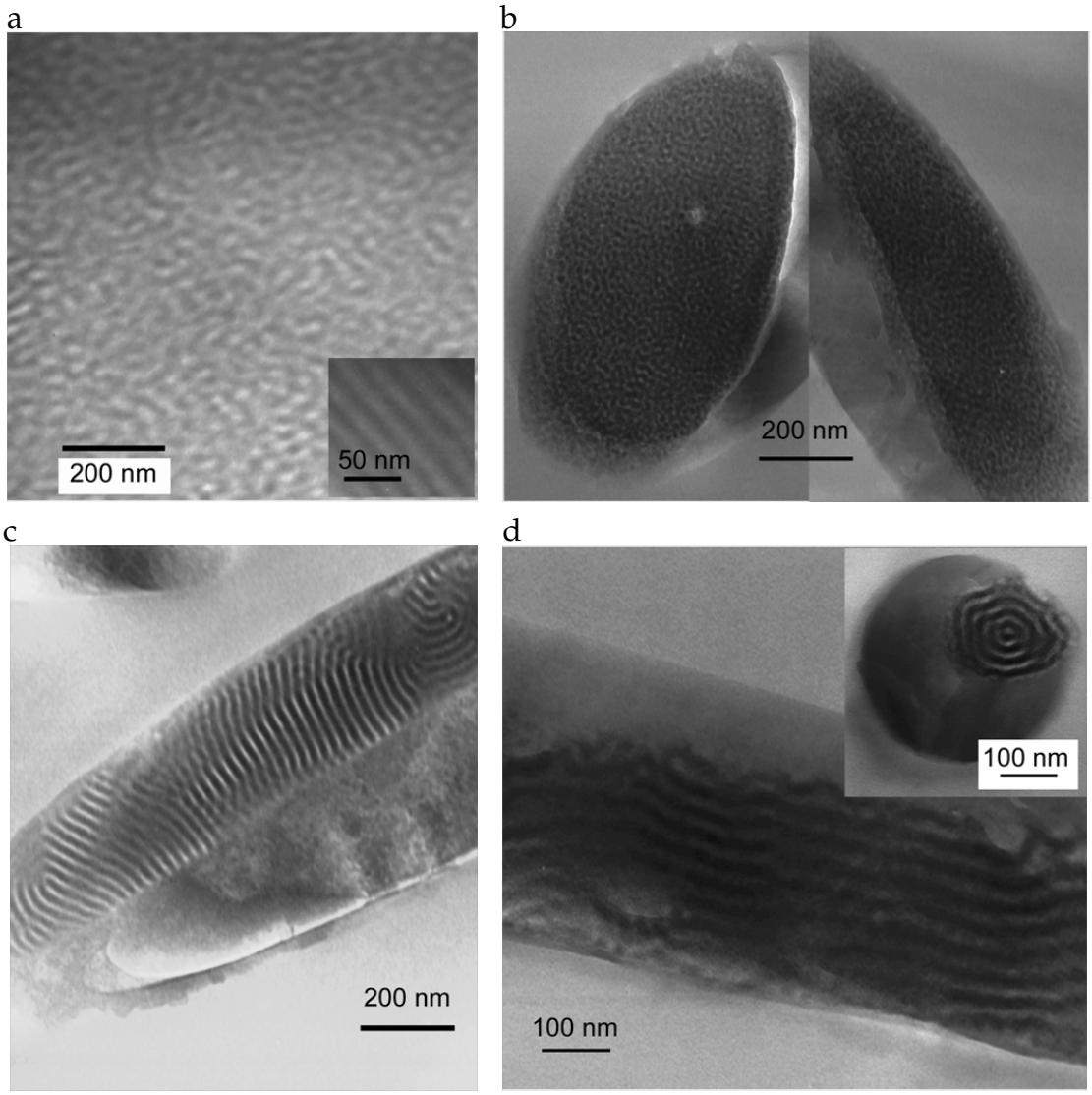

Figure 3.4: TEM images of IS62-27K fibers a) as-spun uniaxial fiber, inset is TEM image of film surface, (equilibrium domain spacing ~ 22 nm), b) as-spun coaxial fiber, c) coaxial fiber annealed at 125^{o}C for 5 hrs, longitudinal cut, d) coaxial fiber annealed at 125^{o}C, 24 hrs, cross sectional and longitudinal cut.

Electrospinning involves high deformation rates leading to a much smaller time scale of flow with respect to the time scale of block copolymer self-assembly. At this high deformation, the macromolecular response of the copolymer dominates causing integrated motion of the PS blocks towards a parallel

alignment [11, 12, 13, 14]. However, as suggested by Daniel *et al.* [21] and Pakula *et al.* [23], necking and rupture of domain structures takes place at very high elongational flows. Hence, with a combination of all these effects, we obtain very small and broken PS/PI domains with some evidence of parallel alignment in as-spun coaxial fibers. On annealing these fibers at 125^{o}C for 24 hrs, as the relaxation of deformation takes place, we see stacked lamellar structures normal to the fiber axis due to the cylindrical confinement of the silica shell. These structures are seen to be very stable, particularly in I62-143K copolymer irrespective of the fiber diameter (300 nm-1 μm) and its ratio to the lamellar repeat period. It is possibly due to its high molecular weight, making it extremely difficult for the long chains to undergo a change in lamellar orientation in the presence of cylindrical confinement. Finally, on annealing at high temperatures and higher times, integrated PS block motion leads to a morphology parallel to the silica wall. This result is in agreement with the findings of Xiang *et al.*[18] who obtained the same structure inside a cylindrical pore approximately 8 times the natural lamellar domain spacing.

Finally, coaxially electrospun PS-b-PI/silica fibers after the annealing process (at 175^{o}C for 24 hrs) were treated with NaOH solution at room temperature for 1 hr to selectively remove the silica skin layer and thus to obtain pure PS-b-PI fiber mats with confined assembly. As confirmed by the SEM image of IS53-143K copolymer fibers after the removal of the silica skin layer in Figure 3.5a, the resulting fibers exhibit slightly rougher fiber surfaces than coaxial fibers, but preserve continuous fiber morphology. The TEM images of IS53-143K copolymer fibers after the removal of the silica skin layer in Figure 3.5b and 3.5c confirm that the silica skin layer has been removed by NaOH solution and that the confined assembly developed during the annealing process remains largely

unperturbed after the treatment with NaOH solution. Hence, these results have demonstrated that pure PS-*b*-PI fiber mats with confined assembly can be obtained by selectively removing the silica skin layer after the annealing process.

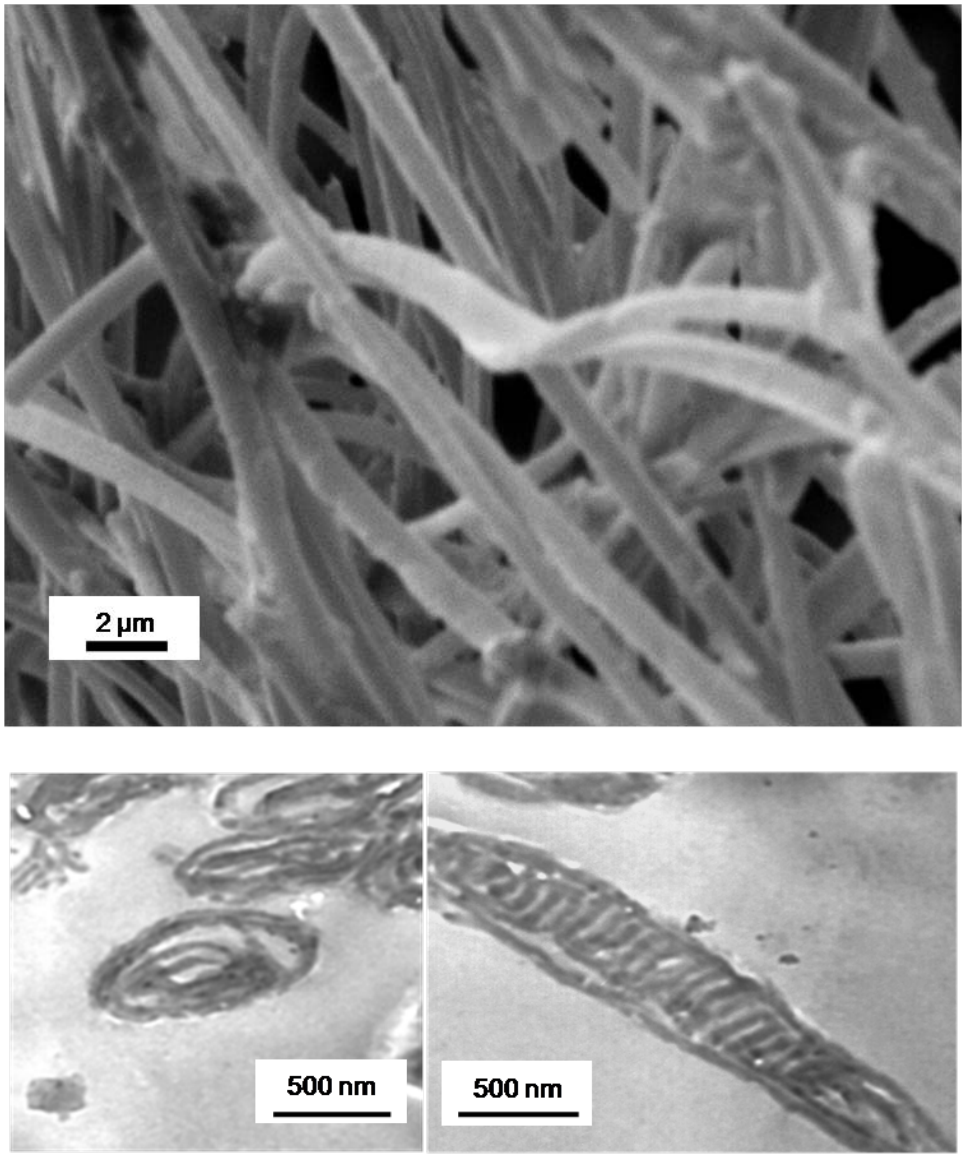

Figure 3.5: IS53-143K copolymer fibers after the removal of the silica skin layer. a) SEM image and TEM images b) a cross section normal to the fiber axis and c) section parallel to fiber axis. Fibers were annealed at 175^{o}C for 24 hrs prior to treatment with NaOH and hence show a mixed morphology of stacked disc and parallel lamellae.

3.5 Conclusion

In this paper, we have extended our studies of self assembled structures from uniaxial electrospun diblock copolymer nanofibers to coaxial nanofibers, where a PS-*b*–PI core is enveloped by a silica shell. Because of the presence of the thermally stable silica sheath in our present fibers, we are able to carry out a comprehensive annealing study to obtain long range ordered structures. Silica sol-gel precursor as a skin layer also enabled us to place a low molecular weight IS62-27K copolymer and obtain submicron scale fibers continuously, which was not possible in conventional, uniaxial electrospinning. Using TEM micrographs, we have shown the structure development in two different molecular weight samples both exhibiting lamellar morphology in the bulk. Coaxially electrospun fibers from both samples show the evolution of lamellar structures from stacked lamellar disc morphology with each disc perpendicular to fiber axis to parallel alternating concentric cylinders of PI and PS via annealing. Due to the high molecular weight and slow kinetics of the IS53-143K copolymer, we can easily control the structure development in these fibers via annealing, but it needs much higher annealing temperature and longer time to completely evolve into the parallel orientation.

We believe that fabrication of continuous coaxial fibers via electrospinning of self-assembling block copolymer and thermally stable silica as the core and the shell together with annealing can provide a useful means to develop optical materials like waveguiding structures [31]. By introducing nanoparticles in one of the blocks and eventually removing the silica via NaOH treatment we can easily manipulate their spatial distribution for use in gas sensing and catalytic applications with an enhanced efficiency.

BIBLIOGRAPHY

[1] Dzenis, Y. *Science* **2004**, 304, 1917.

[2] Li, B.D.; Xia, Y. *Adv. Mater.* **2004**, 16, 1151.

[3] Fong, H.; Reneker, D.H. *Structure Formation in Polymeric Fibers*, Hanser Gardner Publications, Cincinnati, 2001.

[4] Bognitzki, M.; Frese, T.; Steinhart, M.; Greiner, A.; Wendorff, J.H. *Polymer Engineering and Science* **2001**, 41, 982.

[5] Khandpur, A.K.; Foerster, S.; Bates, F.S.; Hamley, I.W.; Ryan, A.J.; Bras, W.; Almdal, K.; Mortensen, K. *Macromolecules* **1995**, 28, 8796.

[6] Bates, F.S.; Fredrickson, G.H. *Annu. Rev. Phys. Chem.* **1990**, 41, 525.

[7] Park, C.; Yoon, J.; Thomas, E.L. *Polymer* **2003**, 44, 6725.

[8] Hamley, I.W. *J Phys.: Condens. Matter* **2001**, 13, 643.

[9] Harada, T.; Bates, F.S.; Lodge, T. *Macromolecules* **2003**, 36, 5440.

[10] Okamoto, S.; Saijo, K.; Hashimoto, T. *Macromolecules* **1994**, 27, 5547.

[11] Maring, D.; Wiesner, U. *Macromolecules* **1997**, 30, 660.

[12] Leist, H.; Maring, D.; Albrecht, T.T.; Wiesner, U. *J. Chem. Phys.* **1999**, 110, 8225.

[13] Zhang, Y.; Wiesner, U.; Spiess, H.W. *Macromolecules* **1995**, 28, 778.

[14] Gupta, V.K.; Krishnamoorti, R.; Chen, Z.R.; Kornfield, J.A.; Smith, S. D.; Satkowski, M. M.; Grothaus, J. T. *Macromolecules* **1996**, 29, 875.

[15] Gupta, V.K.; Krishnamoorti, R.; Kornfield, J.A.; Smith, S.D. *Macromolecules* **1995**, 28, 4464.

[16] Zhang, Y.; Wiesner, U. *J. Chem. Phys.* **1995**, 103, 4784.

[17] Shin, K.; Xiang, H.; Moon, S.I.; Kim, T.; McCarthy, T.J.; Russel, T.P. *Science* **2004**, 306, 76.

[18] Xiang, H.; Shin, K.; Kim, T.; Moon, S.I.; McCarthy, T.J.; Russell, T.P. *Macromolecules* **2004**, 37, 5660.

[19] Wu, Y.; Cheng, G.; Katsov, K.; Sides, S.W.; Wang, J.; Tang, J.; Fredrickson, G.H.; Moskovits, M.; Stucky, G.D. *Nature Materials* **2004**, 3, 816.

[20] Kalra, V; Kakad, P.A.; Mendez, S.; Ivannikov, T.; Kamperman, M.; Joo, Y.L. *Macromolecules* **2006**, 39, 5453.

[21] Daniel, C.; Hamley, I.W.; Mortensen, K. *Polymer* **2000**, 41, 9239.

[22] Seguela, R.; Homme, J.P. *Macromolecules* **1981**, 14, 197.

[23] Pakula, T.; Saijo, K.; Kawai, H.; Hashimoto, T. *Macromolecules* **1985**, 18, 1294.

[24] Kim, G.; Libera, M. *Macromolecules* **1998**, 31, 2569.

[25] Fong, H.; Reneker, D.H. *J. Poly. Sc. Part B* **1999**, 37, 3488.

[26] Ma, M.; Hill, R.M.; Lowery, J.L.; Fridrikh, S.V.; Rutledge, G.C. *Langmuir* **2005**, 21, 5549.

[27] Ruotsalainen, T. *et al. Adv. Mater*. **2005**, 17, 1048.

[28] Loscertales, I.G.; Barrero, A.; Guerrero, I.; Cortijo, R.; Marquez, M.; Ganan-Calvo, A.M. *Science* **2002**, 295, 1695.

[29] Sun, Z.; Zussman, E.; Yarin, A.L.; Wendorff, J.H.; Greiner, A. *Adv. Mater.* **2003**, 15, 1929.

[30] Li, B.D.; Xia, Y. *Nano Letters*. **2004**, 4, 933.

[31] Yang, P.; Wirnsberger, G.; Huang, H.C.; Cordero, S.R. *Science* **2000**, 287, 465.

[32] Choi, S.S.; Lee, S.G.; Im, S.S.; Kim, S.H.; Joo, Y.L. *J. Mater. Sci. Lett.*, **2003**, 22, 891.

CHAPTER 4

CONTROLLING NANOPARTICLE LOCATION VIA CONFINED ASSEMBLY IN ELECTROSPUN BLOCK COPOLYMER NANOFIBERS

4.1 Abstract

Coaxial nanofibers with poly(styrene-*block*-isoprene) (PS-*b*−PI)/magnetite nanocomposite as core and silica as shell have been fabricated using electrospinning [1, 2, 3, 4]. Thermally stable silica helps to anneal the fibers above glass transition temperatures of PS-*b*−PI and form ordered nanocomposite morphologies. Monodisperse magnetite nanoparticles (4 nm) are synthesized and surface coated with oleic acid to provide marginal selectivity towards isoprene domain. When 4 wt% nanoparticles (NPs) are added to symmetric PS-*b*-PI, transmission electron microscopy (TEM) images of microtomed electrospun fibers reveal that NPs are uniformly dispersed only in the PI domain and that the confined lamellar assembly in the form of alternate concentric rings of PS and PI is preserved. For 10 wt% NPs, a morphology transition is seen from concentric rings to a co-continuous phase with NPs again uniformly dispersed in the PI domains. No aggregates or loss of PI selectivity is found in spite of inter-particle attractions due to surface ligand interactions. Magnetic properties are measured using a superconducting quantum interference device (SQUID) magnetometer and all nanocomposite fiber samples exhibit superparamagnetic behavior.

4.2 Introduction

Controlling the spatial location of nanoparticles in polymer matrices is the fundamental challenge surrounding the development of high end polymer nanocomposite materials. High particle surface energies and strong inter-particle interactions often lead to particle aggregates making it difficult to control their location. Typically, the nanoparticle surfaces are modified to avoid aggregates and ensure homogenous distribution throughout the polymer material. However, the effectiveness of these NPs can be enhanced if they are arranged periodically in three dimensions. One can combine the functionality of NPs with the phenomena of block copolymer self-assembly to achieve hierarchical spatial distributions of NPs [5].

Having the NPs periodically spaced can lead to synergistic effects of optical and mechanical properties, for example, and can potentially be used in novel applications such as magnetic storage media and catalysis [6, 7]. Recently, there has been a lot of work where self assembly in block copolymer/nanoparticle films is studied as a function of various parameters like NP surface modification, size of nanoparticles relative to polymer radius of gyration and volume fraction of nanoparticles in the composite. For example, Chui *et al.* [8] selectively placed gold nanoparticles in the polystyrene domain of symmetric Poly (styrene-*b*-2 vinyl pyridine) (PS-PVP) diblock copolymer by coating them with PS ligands. In contrast, particles coated with mixtures of PS and PVP localized at the interfaces between the PS-PVP blocks. Qualitatively similar predictions have also been reported by Schultz *et al.* [9] using discontinuous molecular dynamics simulations. While these works study the effect of enthalpic interactions between nanoparticles and polymer matrices, significant amount of effort has

also gone into the study of entropic contributions to the location of NPs. Two main competing entropic forces have been shown to play a role, namely, the entropic penalty of chain stretching and the translational entropy of nanoparticles. For example, for large selective particles, polymer chains must pay a significant stretching penalty if the particles are uniformly dispersed in the preferred domain, and thus they are usually pushed towards the chain ends at the center of the domain in spite of the loss of translational entropy of NPs. For nanoparticles that are small compared to the polymer radius of gyration, particle translational entropy dominates and they are uniformly dispersed in the preferred domain [7, 10].

Preferential wetting of one domain by surface modified NPs in block copolymers can cause a significant increase in its domain size and eventually induce phase transitions. Sides *et al.* [11] showed both experimentally and using hybrid particle-field simulations that on increasing the NP volume fraction in a lamellar forming diblock copolymer, the preferred domain becomes swollen and distorted and finally transforms into inverse hexagonal cylinder morphology to minimize interfacial energy. Although surface modification has played an important role in guiding NPs at desired locations in block copolymers for many metals like gold and silver, in case of magnetically active particles like magnetite, strong magnetic dipole interactions between particles often lead to clustering and aggregation [12, 15]. Magnetite can display high saturation magnetization and resistance to oxidation, attracting great interest in electrical and biomedical applications. Magnetite nanoparticles have also been shown to display supermagmagnetic behavior due to their small size making them ideal for magnetic field driven transport of drugs, bioseparations, electromagnetic shielding and magnetic sensing [12, 13, 14]. Park *et al.* [15] ex-

ploited the selectivity of film casting solvents to control the morphology of magnetic nanoparticle/polystyrene-*block*- polyisoprene (PS-*b*-PI) nanocomposite films. They used monodisperse γ-Fe_2O_3 nanoparticles of 7 nm diameter with surfaces modified with oleic acid making them marginally selective towards PI. For solvents like THF and toluene which are neutral for PS and PI, they reported the formation of lattice like NP aggregates inducing a BCP phase transition from cylindrical to spherical morphology beyond a small weight fraction of 0.02. For PI selective solvents like hexane, they were able to selectively incorporate NPs into the PI phase, however, aggregates were formed and selectivity of NPs was lost above a weight fraction of 0.05.

To develop desired high performance nanocomposite materials, it is not only critical to develop systems that can incorporate large fractions of functional nanoparticles at desired locations, but for applications such as catalysis or separations, it is important to obtain high exposed functional surface area and an open pore structure to prevent mass flow restrictions [15]. In the present work, we have used electrospinning as a template to fabricate high surface area (10-1000 m^2/g) nanofiber mats with selective incorporation of as high as 10 wt% magnetic nanoparticles in isoprene domains of poly(styrene-*block*-isoprene). Further removal of the styrene domain will increase the exposed surface area by many orders of magnitude.

Electrospinning is a simple and versatile method that uses strong electric fields to draw polymer solutions or melts to produce ultra thin fibers with diameters ranging from 50 to 500 nm [2, 3, 4]. Recently, we reported the formation of highly ordered lamellar morphologies in pure BCP electrospun fibers encapsulated with silica shells using coaxial electrospinning. Thermally stable

silica shell allowed us to anneal the fibers above the glass transition temperatures of the polymers in the BCP and obtain equilibrium-type morphologies [16, 17]. Lamellar structures in the form of stacked discs and alternate concentric rings of PS and PI are formed owing to the elongational deformation during electrospinning and cylindrical confinement of the BCP. Concentric ring structures have also been reported by Ma *et al.* [18] using high molecular weight poly(methylmethacrylate-co-methacrylic acid), P(MMA-co-MAA) as the shell and poly(styrene-*block*-isoprene-*block*-styrene) as the core material in coaxially electrospun fibers. From the materials application perspective, it would now be quite important to move to functionalized fiber materials. To this end, in the present study we demonstrate how to utilize confined assembly to effectively functionalize fibers with magnetic nanoparticles to develop materials for novel applications such as magnetic storage media, catalysis and bioseparations. We show that due to the inherent fast evaporation and strong deformation rates in the electrospinning process, the particles preferentially wet the PI domain and at the same time remain quite monodisperse for much higher particle fractions than what is usually observed in BCP/magnetic NP composite films. In addition, we demonstrate the formation of different BCP/NP self assemblies by changing parameters like annealing temperature and NP volume fraction. Finally, SQUID measurements are presented showing that all fiber samples exhibit superparamagnetic behavior.

4.3 Experimental Methods

4.3.1 Block Copolymer and Nanoparticles Synthesis

Polystyrene*b*-polyisoprene denoted as SI(54-70) with M_{PS} = 53500 g/mol and M_{PI} = 70000 g/mol, is synthesized using a two step living anionic polymerization [16]. The polydispersity of the polymer obtained by gel permeation chromatography is 1.04. Transmission Electron Microscopy (TEM) and small angle x-ray scattering (SAXS) studies were carried out to show the formation of lamellar morphology in films of SI(54-70) cast in THF (not shown here). Monodisperse 4.1$\pm$0.55 nm magnetite nanoparticles with surface coated with oleyl group were synthesized using a method similar to the one demonstrated by Sun *et al.* [19]. 2 mmol of Iron (III) acetylacetonate ($Fe(acac)_3$) was mixed in 20 ml of octadecene with 1,2-hexadecanediol (10 mmol), oleic acid (6 mmol), and oleylamine (6 mmol) under nitrogen and heated to 285 ^oC for 30 min (ramping rate: 3 ^oC/min). The solution was then cooled to room temperature and excess ethanol was added for precipitation. The precipitated magnetite nanoparticles were recovered by centrifugation. Figure 4.1 shows the transmission electron microscopy image and figure 4.2 shows the XRD pattern for magnetite nanoparticles used in the present study. The presence of oleyl group on the surface of particles makes them marginally selective towards PI phase of the BCP [15].

4.3.2 Nanofiber Fabrication via Electrospinning

Coaxial nanofibers were electrospun using 15-17 wt% solution of SI(54-70)/Fe_3O_4 NP mixtures in THF as the inner and silica sol gel precursor as the

outer solution. NP weight fractions in solid polymer were varied from 0-10 %. No significant change in conductivity of the inner solution was seen on addition of nanoparticles. The volumetric flow rates used for inner and outer solutions were 0.02 ml/min and 0.03 ml/min respectively. The fibers were spun at an electric potential if 20 kV with spinneret to collector distance of 4 inches. We refer the reader to our recent publications for a more detailed overview of the experimental set up [16, 17].

4.3.3 Nanofiber characterization

Nanofibers formed were characterized using Scanning electron microscopy (Leo 1550) and their diameters were found in the range from 300 nm to 1 μm with the fiber core diameter typically ranging from 200-500 nm. We refer the reader to our previous publications for the scanning electron microscopy images (SEM) for typical fiber morphology [16, 17]. Fibers, embedded in epoxy matrix, were microtomed into 60 nm thin cross-sectional and longitudinal sections at room temperature using Leica ultracut UCT. Fiber sections were stained in osmium tetraoxide vapors for 10 min and were viewed under Tecnai T12 transmission electron microscope (TEM) operated at 120 KV for further characterization. Magnetic property measurements were made using superconducting quantum interference device (SQUID) at temperatures from 5K to 300 K.

4.4 Results and Discussion

Figure 4.1 shows a transmission electron microscopy (TEM) image of the nanoparticles used in the present study. Details of the synthesis procedure are given in the experimental section. The particles are monodisperse with 4.1$\pm$0.55 nm diameter, as revealed by quantitative image analysis.

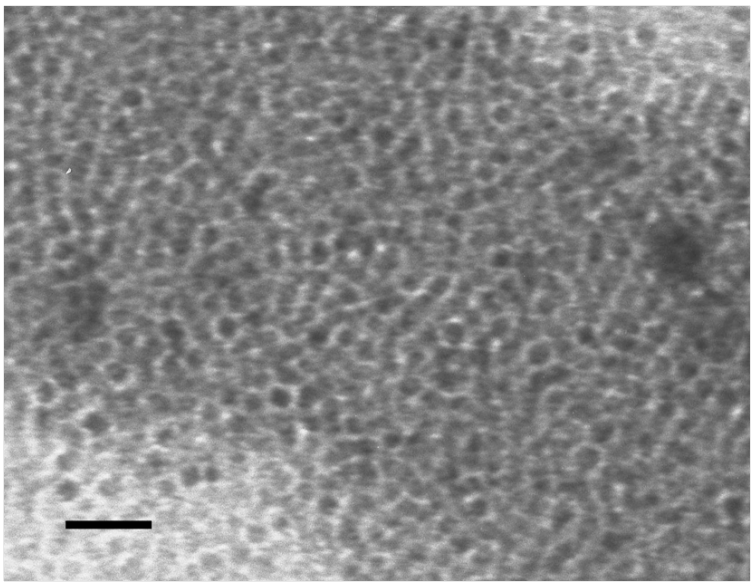

Figure 4.1: TEM image of 4 nm monodisperse magnetite nanoparticles coated with oleic acid. Scale bar is 20 nm.

Figure 4.2 shows the XRD pattern for magnetite nanoparticles. The presence of oleyl group on the surface of particles makes them marginally selective towards the PI phase of the PS-*b*−PI block copolymer as suggested from the Flory Huggins interaction parameter χ_{12} [15]. χ_{12} is proportional to the difference of solubility parameters, $(\delta_1 - \delta_2)^2$: the smaller the difference, the more miscible are the components (δ_{PS}=19.0 (MPa)$^{1/2}$, δ_{PI}=15.2 (MPa)$^{1/2}$, $\delta_{OleicAcid}$=16.0 (MPa)$^{1/2}$).

The PS-*b*−PI block copolymer (SI(54-70)) used in the present work forms a lamellar morphology in the bulk/film. Figure 4.3 shows TEM images of cross-

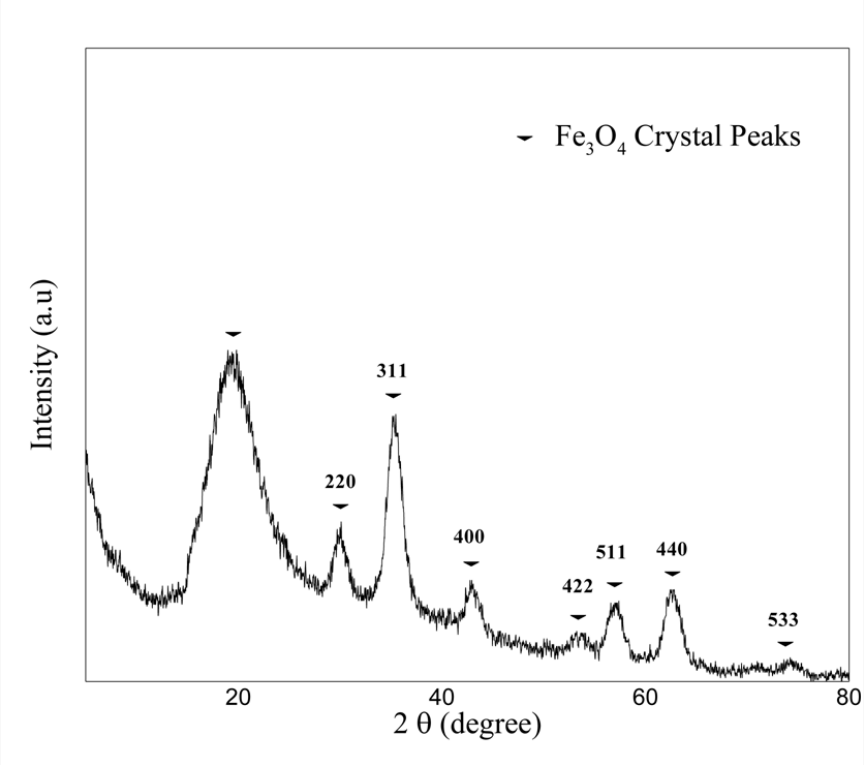

Figure 4.2: XRD pattern of 4 nm magnetite nanoparticles

sections and longitudinal sections of fibers electrospun using a solution of neat SI(54-70) in THF as the core material. All fiber samples in this study use a silica precursor solution as the shell material to provide thermal stability to the polymer core and allow us to anneal the fibers at temperatures higher than the BCP glass transition temperatures without causing the fiber to melt. A stacked disc morphology perpendicular to the fiber axis is formed in confined block copolymer fibers on annealing at 125 ^{o}C for 24 hrs as an effect of relaxation after strong deformation during electrospinning [17]. On further annealing at a temperature (175 ^{o}C, 50 hrs.) well above the glass transition temperature of the block copolymer, the morphology slowly relaxes to alternating concentric rings of PS (unstained, light regions) and PI (stained dark regions) due to the cylindrical confinement of the silica shell [17, 20]. We suggest that the perpendicular

lamellar morphology is a metastable state formed as the polymer chains orient along the fiber axis due to elongational deformation during electrospinning. On further annealing the lamellae relax into a parallel orientation owing to the interaction with the silica surface.

Figure 4.4 shows the corresponding results for 4 wt% NP/BCP composite self assembly. The nanoparticles (black dots in TEM images) are selectively and uniformly dispersed in the PI phase. As suggested by previous work the selectivity is due to the presence of oleyl groups on the particle surface [15]. No evidence of significant magnetic particle aggregation of was found in the TEM images possibly due to the fast solvent evaporation and strong elongational deformation during electrospinning. A similar transition from stacked disc structures (Figure 4.4a,b) to concentric ring morphologies (Figure 4.4c,d) is observed in 4 wt% NP/BCP composite fibers, although the transition is not as clear as in neat BCP fibers (Figure 4.3). The PI domains appear to be slightly swollen due to the addition of NPs, however, no significant effect is seen on the self-assembly or the time scale of change of lamellar orientation due to the low volume fraction of the particles.

In contrast, on addition of 10 wt % NPs in SI(54-70) a morphology transition is seen from concentric rings to a co-continuous phase (Figure 4.5). It should be noted that NPs still remain uniformly and selectively dispersed in the PI phase in spite of the high BCP particle loading. Due to the constraint of cylindrical confinement no clear order is seen in the continuous phase, but the PI domains with NPs are visibly expanded throughout the entire fiber. Nanofiber mats with co-continuous assembly and well dispersed NPs in one domain may be useful in fabrication of membrane materials with well connected pore structure after

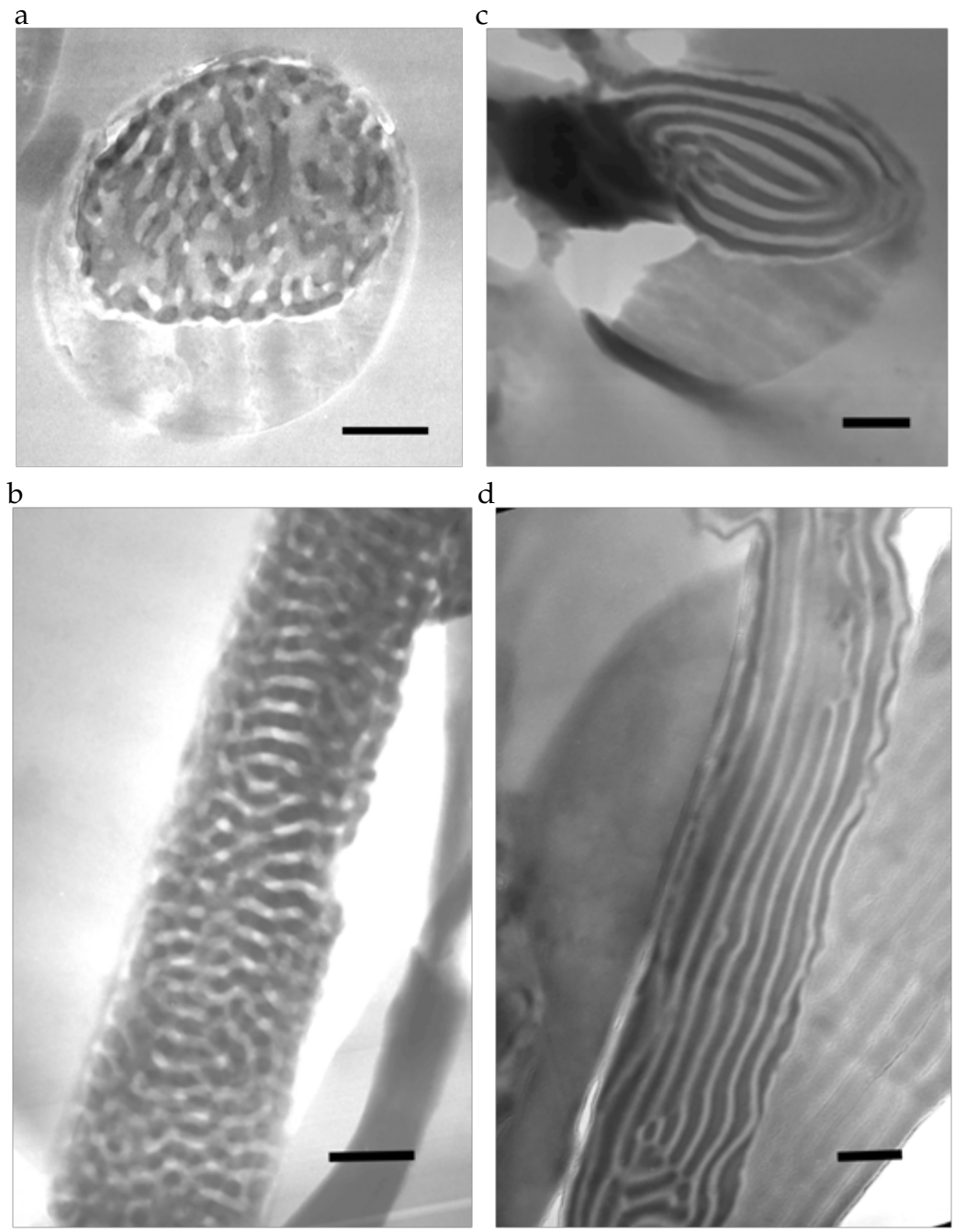

Figure 4.3: TEM images of microtomed coaxial nanofibers with neat SI(54-70)(0 wt% NP) as core and silica as shell (a) cross sectional cut of fiber, annealed at 125 ^{o}C, 24 hrs. (b) fiber cut along the axis, annealed at 125 ^{o}C, 24 hrs, (c) cross sectional cut of fiber annealed at 175 ^{o}C, 50 hrs and (d) fiber cut along the axis, , annealed at 175 ^{o}C, 50 hrs Grey shell region is silica, in the core, light regions are PS domains, dark regions are stained PI domains. All scale bars are 200 nm.

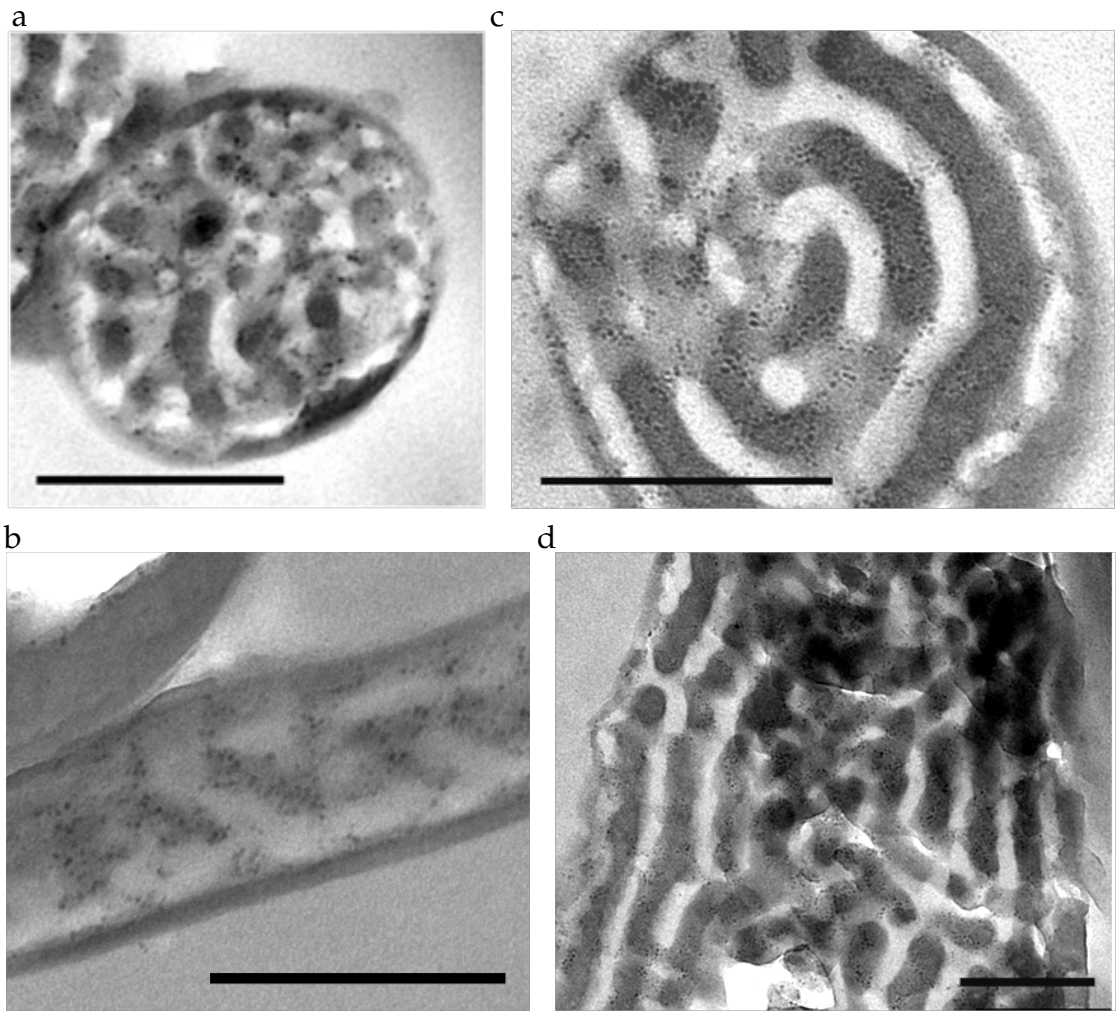

Figure 4.4: TEM images of microtomed coaxial nanofibers with 4 wt% magnetite NP/SI(54-70) as core and silica as shell (a) cross sectional cut of fiber annealed at 125 ^{o}C, 24 hrs (b) fiber cut along the axis annealed at 125 ^{o}C, 24 hrs (c) cross sectional cut of fiber, annealed at 175 ^{o}C, 50 hrs and (d) fiber cut along the axis, annealed at 175 ^{o}C, 50 hrs. Grey shell region is silica, in the core, light regions are PS domains, dark regions are stained PI domains and even darker dots are magnetite NPs. All scale bars are 200 nm.

selective etching of the other domain [21].

Figure 4.6 shows the magnetic properties of 10 wt% NP/SI(54-70) fibers annealed at 175 ^{o}C for 50 hrs measured using a superconducting quantum in-

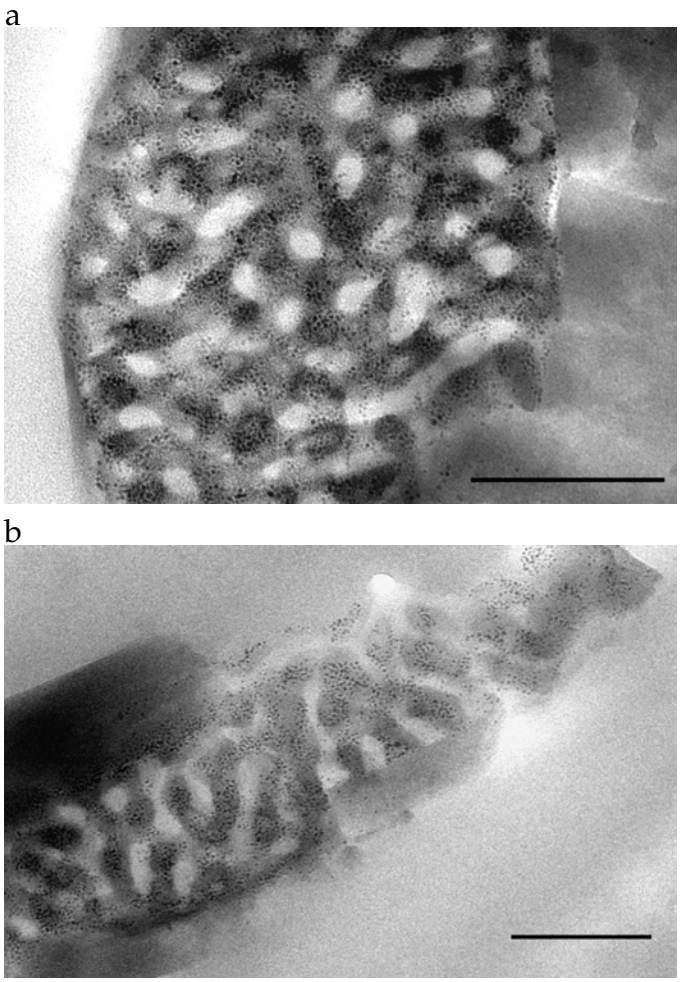

Figure 4.5: TEM images of microtomed coaxial nanofibers with 10 wt% magnetite NP/SI(54-70) as core and silica as shell annealed at 175 ^{o}C for 50 hrs. (a) cross sectional cut of fiber, (b) fiber cut along the axis. Grey shell region is silica, in the core, light regions are PS domains, dark regions are stained PI domains and even darker dots are magnetite NPs. All scale bars are 200 nm.

terference device (SQUID). Magnetic particles below a certain critical diameter show superparamagnetic behavior as thermal fluctuations are enough to randomize the magnetic moments thus resulting in a lack of magnetization at zero applied magnetic field [22]. Materials with monodisperse incorporation of such particles can be very useful for reducing the dissipated energy in applications where non uniform fields are needed or for use in magnetically assisted bioseparation devices. From the SQUID results, we find that the superparamagnetic behavior of these particles is preserved at room temperature.

Figure 4.6 also shows the hysteresis curve for the fibers at 5 K showing a remnant magnetization with a coercivity of 250 Oe due to the exponential increase in the relaxation time scale with decreasing temperature. We performed zero field cooling (ZFC) and field cooling experiments at 100 Oe and a blocking temperature (maxima of ZFC curve) of 13K was found. Samples exhibit superparamagnetic behavior above 13 K. This temperature agrees with the Arrhenius expression, Eq. (4.1), for 4 nm magnetite particles corroborating the TEM results that particles remain well dispersed in the fibers:

$$\frac{1}{\tau} = f_0 \exp\left(-\frac{KV}{k_B T_B}\right) \tag{4.1}$$

here τ is the experimental measurement time (= 100 sec) for SQUID magnetometer, f is the frequency constant characteristic of the material, K is the anisotropy constant, V is the volume of the magnetic particle, k_B is the Boltzmann constant and T_B is the blocking temperature. Values of f and K for magnetite were taken from Valenzuela, *et al.* [23]. The response of the mat of 10wt% BCP/NP nanofibers to the field provided by a small laboratory magnet, clearly exhibits the field responsive behavior of these materials (figure 4.7). The attraction of the magnetic fiber sample to a laboratory magnet compliments our SQUID measurement and shows that the magnetic nanoparticles experience a

a

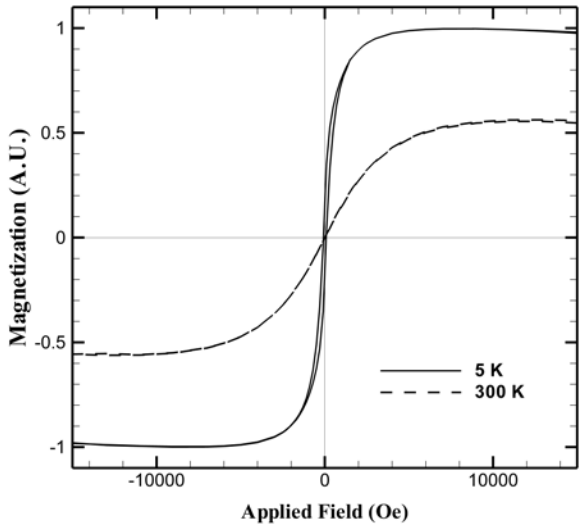

b

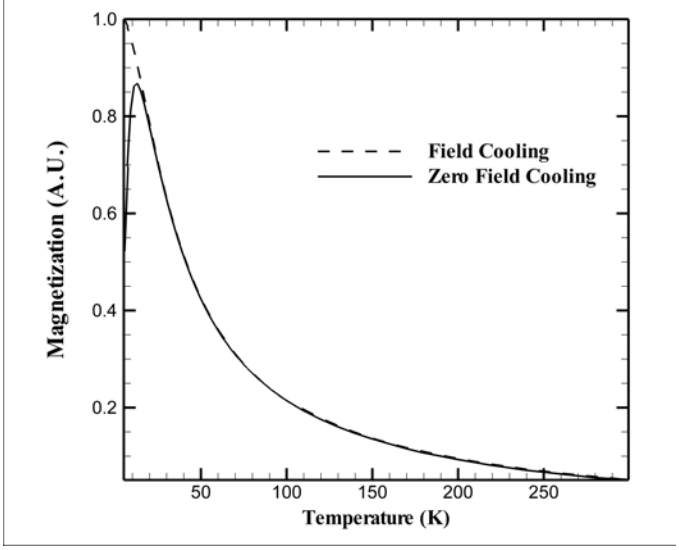

Figure 4.6: Magnetic properties of 10 wt% magnetite NP/SI(54-70) as core and silica as shell annealed at 175 ^{o}C for 50 hrs measured using SQUID. (a) hysteresis curves showing magnetization vs. applied field at 5 K and 300 K, (b) Zero field cooling and field cooling at 100 Oe showing a blocking temperature of 13 K.

visible translational force in the direction of the magnetic field gradient

Figure 4.7: Field responsive behavior of PS-*b*−PI/magnetite nanofiber mat using a laboratory magnet.

0-10 wt% of magnetic nanoparticles are incorporated into BCP nanofibers with uniform distribution of NPs in the desired block copolymer domain. From these results we suggest that the self assembly of NP/BCP nanocomposites in electrospun fibers can be controlled by the relative time scales of BCP ordering, selective incorporation of NP into PI and self aggregation of magnetite NPs. During the fast (~10^{-3} s) micro-phase separation of PS and PI due to high solvent evaporation rates (~ 200 nl/s) in electrospinning, NPs locally favor selective incorporation into the PI phase over self aggregation due to the low volume fraction of NPs [15]. This process is further aided by the strong deformation during the process due to the increase in the relative distance between particles and effect of deformation on particle diffusion as seen in some of our preliminary simulation work [28, 29]. The role of electrospinning in achieving these nanocomposites is also evident from the TEM images and SQUID measure-

ments (Figures 4.8, 4.9) of as-made BCP/nanoparticle nanofibers that show selective and uniform dispersion of magnetite NPs in the PI domain.

Well dispersed NPs in the PI domains even after annealing at high temperatures as shown in the above figures, suggest that the particles get trapped in the desired phase during electrospinning and move along with the domain during BCP melt ordering. For comparison, we have shown a TEM image of nanorods of the same nanocomposite system in figure 4.10. The nanorods were fabricated using a procedure used by Xiang *et al.* [20]. The image shows that aggregates of nanoparticles are formed and selectivity of NPs towards isoprene domain is lost. Due to slow solvent evaporation and quiescent conditions during nanorod fabrication process, NPs have enough time/mobility to aggregate. The strong NP-NP attraction negates any differences in NP solubility in isoprene or styrene and leads to loss in selectivity. We are currently in the process of understanding the effect of deformation during electrospinning on prevention of particle aggregation using particle based simulations [28, 29]. THF is a neutral solvent for PS and PI, so we do not expect any contribution of the solvent selectivity in selective placement of NPs in PI phase [15]. No evidence of column alignment of nanoparticles [26] was seen due to the electrospinning process possibly due to the low conductivity of the oleyl group covered magnetite NPs used in this work. The nanoparticles remain uniformly dispersed in the isoprene domain and do not prefer to arrange at the domain center (where most polymer chain ends lie) due to the small NP/domain (= 4nm/30nm = 0.13) size ratio [10]. The NP size lies in the regime where conformational entropy loss of the polymer chain upon particle sequestration is not significant and therefore the particles prefer to uniformly disperse in isoprene to gain translational entropy.

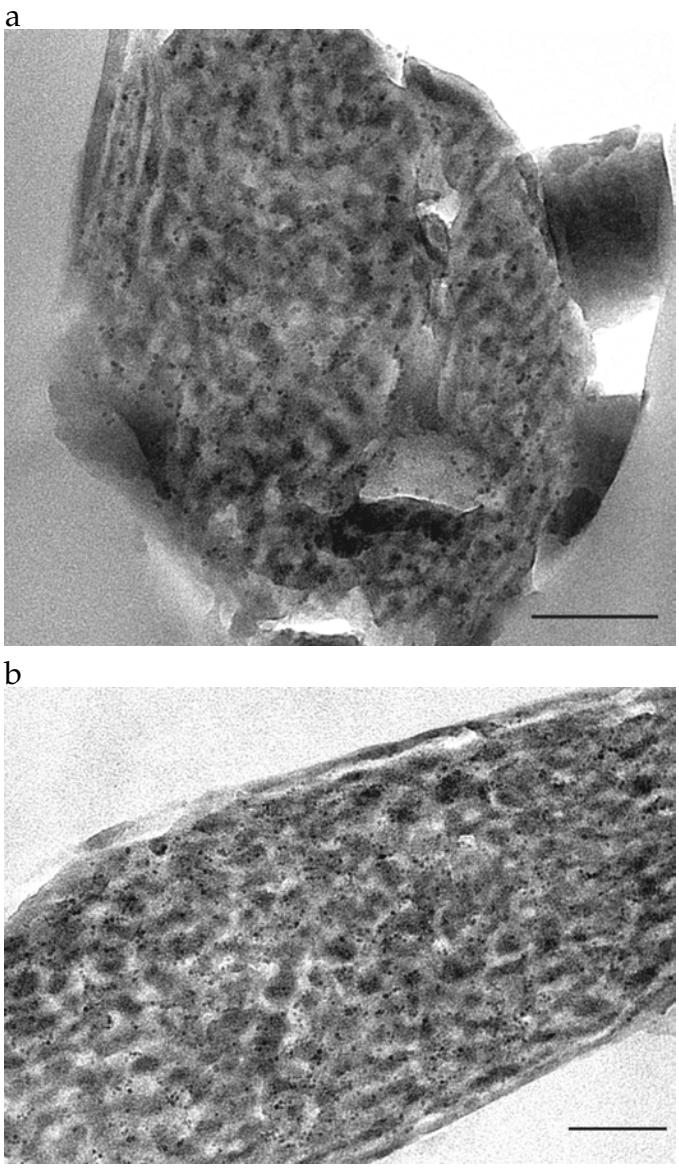

Figure 4.8: TEM images of as spun 4 wt% magnetite NP/PS-*b*–PI nanofibers. The self assembled structures are disordered due to the fast solvent evaporation and deformation during electrospinning [16].

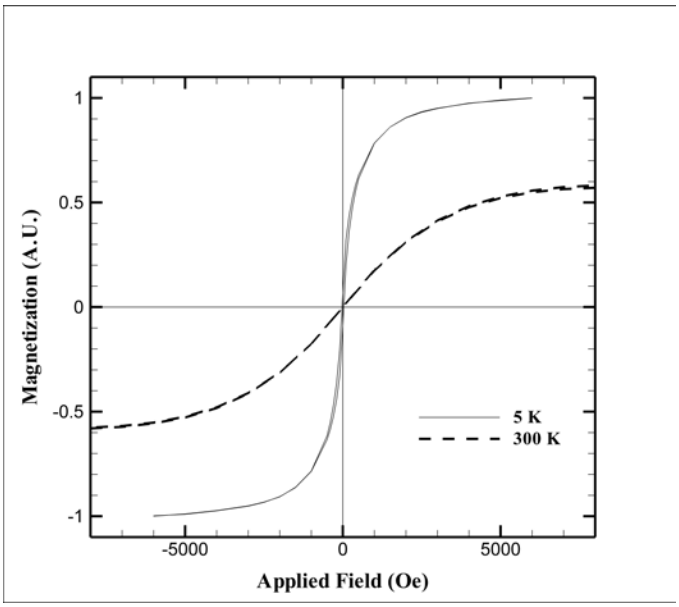

Figure 4.9: SQUID measurements showing superparamagnetic properties of as spun 4 wt% magnetite NP/PS-*b*−PI nanofibers.

4.5 Conclusions

In summary, up to 10 wt% magnetite nanoparticles have been selectively incorporated in PS-*b*-PI electrospun nanofibers with no evidence of aggregation. For low nanoparticles fraction, lamellar morphology in the form of alternate concentric rings of PS and PI is preserved and a flip of orientation from perpendicular to parallel relative to the walls is seen on using stronger annealing conditions. A transition of morphology from lamellar to a co-continuous structure is observed for high particle fractions. In all samples, selectivity of nanoparticles towards isoprene is maintained and particles remain non aggregated and monodisperse. Our results demonstrate that electrospinning can act as a good template to selectively and uniformly disperse nanoparticles such as magnetite which usually have a strong tendency to aggregate Our electrospun nanofibers exhibit superparamagnetic properties with a blocking temperature of 13 K. To the best of our

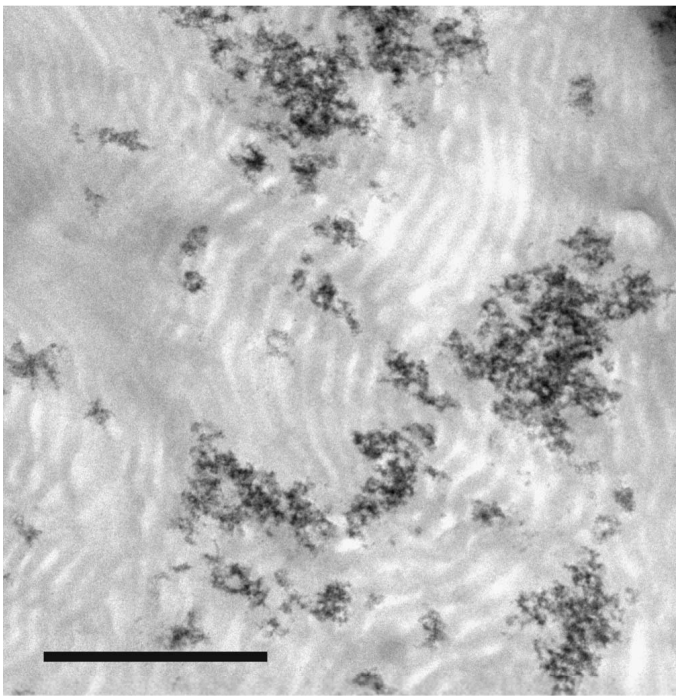

Figure 4.10: TEM image of 1 wt% magnetite NP/SI(54-70) nanorod. The image shows aggregates of nanoparticles are formed and selectivity of NPs towards isoprene domain is lost. Scale bar is 1 μm.

knowledge this is the first effort where precise control over the location and distribution of magnetic nanoparticles in block copolymer nanofibers with tunable confined self assembly has been demonstrated. Periodic magnetic grains only a few tens of nanometers across can give way to future generations of magnetic storage media and magnetic sensing [14]. Films of porous superparamagnetic nanofibers formed after removal of styrene domain can be used for the separation of magnetically labeled biological molecules combining size exclusion technique with magnetic interactions [27]. Furthermore, the ability to fabricate high

surface area nanocomposite materials and prevent nanoparticle aggregation is a first step towards fabrication of different types of nanocomposite materials using nanoparticles where any surface modification can lead to loss in activity. For example, catalytic membranes can be made with well dispersed nanoparticles with little or no surface modification. Furthermore, with the dispersion of such functional nanoparticles in high surface area nanofiber mats, catalytic efficiency, for example, may magnify many folds.

BIBLIOGRAPHY

[1] Loscertales, I.G.; Barrero, A.; Guerrero, I.; Cortijo, R.; Marquez, M.; Ganan-Calvo, A.M. *Science* **2002**, 295, 1695.

[2] Sun, Z.; Zussman, E.; Yarin, A.L.; Wendorff, J.H.; Greiner, A. *Adv. Mater.* **2003**, 15, 1929.

[3] Li, B.D.; Xia, Y. *Nano Letters*. **2004**, 4, 933.

[4] Yu, J.H.; Fridrikh, S.V.; Rutledge, G. C. *Adv. Mater.* **2004**, 16, 1562.

[5] Warren S.C.; Messina L.C.; Slaughter L.S.; Kamperman M.; Zhou Q.; Gruner S.M.; DiSalvo F.J.; Wiesner U. *Science* **2008**, 320, 1748.

[6] Balazs, A. C.; Emrick, T.; Russell, T. P. *Science* **2006**, 314, 1107.

[7] Bockstaller, M. R.; Mickiewicz, R. A.; Thomas, E. L. *Adv. Mater.* **1992**, 17, 1331.

[8] Chui, J. J.; Bumjoon, J. K.; Kramer, E. J.; Pine, D. J. *J Am. Chem. Soc.* **2005**, 127, 5036.

[9] Schultz, A. J.; Hall, C. K.; Genzer, J. *Macromolecules* **2005**, 38, 3007.

[10] Warren S.C.; DiSalvo F.J.; Wiesner U. *Nature Mater.* **2007**, 6, 156.

[11] Sides, S. W.; Bumjoon, J. K.; Kramer, E. J.; Fredrickson, G. H. *Phys. Rev. Lett.* **2006**, 96, 250601.

[12] Harris, L. A.; Goff, J. D.; Carmichael, A. Y.; Riffle, J. S.; Harburn, J. J.; St. Pierre, T. G.; Saunders, M. *Chem. Mater.* **2003**, 15, 1367.

[13] Park, J.; An, K.; Hwang, Y.; Park, J. G.; Noh, H. J.; Kim, J. Y.; Park, J. H.; Hwang, N. M.; Hyeon, T. *Nature Materials* **2003**, 3, 891.

[14] Jeong, U.; Teng, X.; Wang, Y.; Yang, H.; Xia, Y. *Adv. Mater.* **2007**, 19, 33.

[15] Park, M. J.; Char, K. *Langmuir* **2006**, 22, 1375.

[16] Kalra, V.; Kakad, P. A.; Mendez, S.; Ivannikov, T.; Kamperman, M.; Joo, Y. L. *Macromolecules* **2006**, 39, 5453.

[17] Kalra, V.; Mendez, S.; Lee, J. H.; Nguyen, H.; Marquez, M.; Joo, Y. L. *Adv. Mater.* **2006**, 18, 3299.

[18] Ma, M.; Krikorian, V.; Yu, J. H.; Thomas, E. L.; Rutledge, G. C. *Nano letters* **2006**, 6, 2969.

[19] Sun, S.; Zeng, H. *J. Am. Chem. Soc.* **2002**, 124, 8204.

[20] Xiang, H.; Shin, K.; Kim, T.; Moon, S. I.; McCarthy, T. J.; Russell, T. P. *Macromolecules* **2004**, 37, 5660.

[21] Uehara, H.; Yoshida, T.; Kakiage, M.; Yamanobe, T.; Komoto, T.; Nomura, K.; Nakajima, K.; Matsuda, M. *Macromolecules* **2006**, 39, 3971.

[22] Cullity, B. D. *Introduction to Magnetic Materials*; Addison-Wesley Publishing Co., 1972.

[23] Valenzuela, O. A.; Fannin, P. C.; Galindo, R. B.; Fernandez, O. R.; Aquino, J. M. *J. Magn. Magn. Mater.* **2007**, 311, 111.

[24] Fornes, T. D.; Yoon, P. J.; Keskkula, H.; Paul, D. R. *Polymer* **2001**, 42, 9929.

[25] Zhao, J.; Morgan, A. B.; Harris, J. D. *Polymer* **2005** 46, 8641.

[26] Mao, W.; Singh, H.; Hatton, T. A.; Rutledge, G. C. *Polymer* **2004**, 45, 5505.

[27] Garcia, C.; Zhang, Y.; DiSalvo, F.; Wiesner, U. *Angew. Chem. Int. Ed.* **2003**, 42, 1526.

[28] Kalra, V.; Mendez, S.; Escobedo, F.; Joo, Y.L. *Journal of Chemical Physics* **2008**, 128, 164909.

[29] Kalra V.; Joo, Y.L. *Proceedings of AIP Conferences* **2008**, 534, 1027.

CHAPTER 5

CONFINED ASSEMBLY OF ASYMMETRIC BLOCK COPOLYMER NANOFIBERS VIA MULTI-AXIAL JET ELECTROSPINNING

5.1 Abstract

Block copolymer (poly(styrene-*b*-isoprene), PS-*b*-PI) Nanofibers with various asymmetric compositions have been fabricated using multiaxial (triaxial/coaxial) electrospinning with silica as the shell and polymer solution(s) in the inner layer(s). For the case of coaxial nanofibers, cylinder-forming block copolymers with different volume fractions have been studied to understand the effect of physical confinement on self assembly of hexagonal cylinders. Various confined assemblies with coexisting cylinders and concentric lamellar rings have been obtained in electrospun block copolymer nanofibers. This confined assembly is then utilized as a template to guide the placement of functional nanoparticles such as magnetite selectively into the PI domain in self assembled nanofibers. To further investigate the effect of the interfacial interaction and frustration due to physically confined environment on the self assembly in electrospinning, triaxial configuration has been used where the middle layer with block copolymer is sandwiched by the innermost and outermost silica layers. Our results reveal that confined-assembly is significantly altered by the presence and interaction with both inner and outer silica layers. When nanoparticles are incorporated into PS-*b*-PI with PI cylinder morphology and placed as the middle layer, the PI phase with magnetite nanoparticles migrates next to the

silica layers. The migration of PI phase to the silica layers has been observed for the mixture of PS and PS-*b*-PI with PS cylinder morphology as the middle layer. These materials not only provide a platform to further study the effect of confinement and wall interactions on self assembly, but also can help develop an approach to fabricate multi-layered, multi-structured nanofibers for high end applications such as drug delivery.

5.2 Introduction

Electrospinning is a simple, top-down method that has earned enormous attention due to its versatility and capability to produce continuous nanofibers. Typically, a strong electric field is applied on a droplet of polymer solution/melt. When the electrostatic forces on induced charges on polymer liquid surface exceed surface tension, a thin polymer jet is ejected. The charged jet undergoes strong deformation (strain (extension) rate $\sim 10000\ s^{-1}$) and fast solvent evaporation (~ 200 nl/s) and gets deposited on a grounded collector placed $4 \sim 6$ inches away as a random non woven mat. We refer the reader to recent reviews that elaborate on the versatility and promise of this distinctive process [1, 2]. Owing to the ultrathin diameters, these fiber mats exhibit large surface area to mass ratios and are attractive materials for high performance separation, sensing and filtration devices, to name a few. Specific surface area ranges from 10 m^2/g for fiber diameters of 500 nm to 1000 m^2/g for diameters around 50 nm.

Recently, some work has been done to fabricate core/sheath nanofibers by coaxially electrospinning two different immiscible liquids through a coaxial spinneret system [3, 4, 5, 6]. Using ethylene glycol and photopolymer as in-

ner and outer jets, Loscertales *et al.* demonstrated the principles and design of stable, coaxial, electrified liquid nanojets towards the production of nanocapsules and nanofibers [3]. Sun *et al.* described the processing of core-shell nano-/mesofibers by coaxial electrospinning of polymer solutions or a combination of polymer solution and melt [4]. They demonstrated that undesirable mixing of the core and shell material can be prevented by slow diffusion rates of the polymer chains as compared to the fast solidification of the polymer jet in the electrospinning process. In the coaxial electrospinning process, the shell serves as a template for formation of fibers from the core material. Therefore, as demonstrated by Yu *et al.* [5], this process is particularly advantageous for core materials that are not viscoelastic enough to form fibers by themselves. Using coaxial electrospinning, Li and Xia produced hollow nanofibers with walls made of titanium oxide/poly(vinyl pyrrolidone) (TiO_2/PVP) composite or pure titania [6]. Recently, melt coaxial electrospinning has been demonstrated as a versatile method for the encapsulation of solid materials and fabrication of phase change nanofibers [7]. In this study we demonstrate the use of sol-gel technique to produce polymer-ceramic functional nanofibers. Silica sol-gel is prepared by a combination of hydrolysis and condensation reactions in a precursor solution formed with carefully chosen compositions of tetraethyl orthosilicate (TEOS), distilled water, ethanol and HCl. The solution gels over time due to the formation of linear networked structures rendering it spinnable at a viscosity of about 10 poise [8]. The presence of linear structures increases the extensional viscosity of these materials. The viscosity along with the high electric conductivity of the solvent helps the formation of very stable liquid jets in the presence of electric field and robust nanofibers [8]. Moreover, as we will see in the remaining part of the paper, the thermal stability of silica offers a useful means to induce self-

assembly of block copolymers during high temperature annealing. In this work, we wish to combine the advantages of nanofiber mats (e. g. high surface area, open pore structure, ability to be woven into a fabric) [2] with the functionalities of block copolymer self assembly to greatly widen the scope of potential applications.

Block copolymer (BCP) solutions and melts are known to self assemble into a variety of nanoscale morphologies including spheres, rods, micelles, lamellae, vesicle tubules, and cylinders (typically in the size range of few tens of nanometers) depending on the volume fraction and interaction parameter between different blocks [9, 10]. This phenomenon has been extensively studied for both solution and melt in bulk systems via theory [11, 12], experiments [13, 14, 15] and simulations [16, 17, 18, 19]. BCP self assembly has attracted increasing interest in recent years for applications in nanotechnology [14]. Precise control over the size, shape and periodicity of these nanoscale microdomains is the key factor in providing opportunities for realization of nanoscale systems.

In order to combine the two systems, we develop nanofibers using block copolymers. The main limitation in fabricating such materials is the inability to form ordered self assembly in-situ due to the fast solvent evaporation and strong deformation during electrospinning [20]. Furthermore, post annealing treatment is also difficult so as to preserve the fiber morphology.

To overcome this limitation, we fabricate polymer nanofibers with silica as a protective shell using multi-axial (coaxial/triaxial) electrospinning. The silica shell (synthesized using sol gel technique) provides thermal stability to the fibers and helps to anneal the materials at temperatures higher than core polymer glass transition to obtain equilibrium self assembly without destroying the

fiber morphology [20, 21]. It also serves as a process aid for low molecular weight unentangled polymers that are difficult or impossible to electropsin. Most of this paper is dedicated to our results on coaxial electrospinning with silica shell and block copolymer core. Towards the end, we present our recent work on triaxial electrospinning, also with silica as the outermost shell and different combinations of materials for the innermost and middle layers.

As shown in our previous study, the silica layer is later etched using HF solution to obtain continuous nanofibers (100-400 nm diameters) with periodic internal meso-structures. Furthermore, with selective removal of one of the BCP domains, mesoporous nanofibers can be fabricated with the ability to tailor the size and shape of the pores by using different molecular weight BCPs and block volume ratios respectively. Previously, highly porous fibers of various polymers were created by electrospinning with a modified collector where a bath of liquid nitrogen was used to freeze the fibers, inducing a phase separation between the polymer and the solvent [22]. Porous nanofibers can be very advantageous in applications such as tissue engineering, catalysis, filtration and drug delivery [2]. For example, internal fiber mesopores act as anchoring points for cells in tissue engineering. For filtration, catalysis or sensing applications, the mesopores increase the surface area, while the external large pores in fiber mats provide an open structure and prevent any mass flow restrictions of the inlet fluid. The walls of the pores can be functionalized for catalytic, sensing and separation applications by tailoring the location of nanoparticles such that they selectively wet only one of the BCP domains.

Our methodology provides an easy template to study the effect of cylindrical confinement or shell-core interaction on self assembly compared to nan-

otubes/nanorods [23, 24]. Nanorods are discontinuous objects and are therefore difficult to align, assemble and process. We had recently reported the effect of cylindrical confinement on bulk lamellar forming poly(styrene-*b*-isoprene) using the procedure mentioned above [20, 21]. Ma *et al*. had independently demonstrated a similar procedure using high molecular weight PMMA as the shell instead of silica and a relatively low molecular weight core polymer so that its relaxation temperature and time remains lower than the glass transition of the shell polymer [25].

In the current study, we present how the interfacial interaction and frustration due to physically confined environment affects the morphology of bulk cylinder and sphere forming block copolymers. The effect is particularly prominent in cylinder forming block copolymers; the cylinders tend to bend around the fiber axis due to stresses created at the outer BCP domains due to the physical confinement of the shell creating mixtures of hexagonal cylinders and concentric lamellar layers. The confinement effect is even more drastic and interesting in triaxial nanofibers with block copolymer as the middle layer and silica as the outermost and innermost layers. Finally, to incorporate functionalities into such self assembled materials, we have incorporated NPs into the PS-*b*-PI core material. Magnetite nanoparticles coated with oleic acid are selectively dispersed in the isoprene domain of PS-*b*-PI nanofibers (with silica shell). This provides a comprehensive approach for the fabrication of high performance multifunctional nanomaterials. For instance, nanofiber mats with both magnetic and florescent functionalities can combine size exclusion with magnetic interaction for collecting and separating proteins present in blood in small amounts that may have diagnostic value for an early detection of diseases. The presence of fluorescent nanoparticles will provide a sensitive marker for counting the sepa-

rated cells using fluorescence imaging.

5.3 Experimental Methods

5.3.1 Material Fabrication

Tetra(ethyl) ortho silicate (TEOS) was supplied by Aldrich. To produce the sol-gel solution, a molar ratio of TEOS:EtOH:H_2O:HCl of 1:2:2:0.01 was used. After vigorous mixing to produce a homogeneous solution, the solution was placed in a 50^{o}C oven to accelerate the sol-gel transition. After ripening for 3 - 5 hours, the solution is ready to be electrospun. An applied voltage of 20 kV was used, the outer jet flow rate was 0.03 ml/min and the inner jet flow rate was 0.02 ml/min, and the tip to collector distance was 4.5 inches. The polymer solution concentration (~0.1-0.15 weight fraction) and the above spinning conditions were carefully chosen to obtain a continuous production of sub-micron scale coaxial fibers. For triaxial electrospinning, the flow rates used were 0.02, 0.015, 0.02 ml/min, for innermost, middle and outermost layers, respectively. The rest of the conditions were same as above. The electropsun fibers were annealed at temperatures in the range of 125^{o}C to 180^{o}C (> polymer glass transition of 100^{o}C) to obtain equilibrium self assembled structures. Six different PS-*b*-PI polymers with asymmetric compositions were used in this study, with isoprene volume fraction of 0.09, 0.19, 0.28, 0.31, 0.33, and 0.74. They are denoted as SI-09, SI-19, SI-28, SI-31, SI-33, and SI-74, respectively, and have total molecular weights of 56200, 45750, 45800, 41800, 45000 and 34100 respectively. SI-09 forms spherical structures of the isoprene phase arranged in BCC lattice in

the bulk. SI-19, SI-28, SI-31 and SI-33 form hexagonal cylinders of the isoprene phase in the bulk while SI-74 forms hexagonal cylinders of the styrene in accordance with the PS-*b*-PI melt phase diagram [9], and also as seen in Transmission Electron Microscopy (TEM) studies. The information on various PS-*b*−PI used in this study is tabulated in Table 5.1. The polydispersity of these block copolymers determined by NMR and GPC is less than 1.04.

Table 5.1: Details of all PS-*b*−PI block copolymers used in this study.

Name	**Total MW**	**PI Vol. Fraction**	**Bulk Morphology**
SI-09	56200	0.09	Sphere (BCC)
SI-19	45750	0.19	Hexagonal Cylinders
SI-28	45800	0.28	Hexagonal Cylinders
SI-31	41800	0.31	Hexagonal Cylinders
SI-33	45000	0.33	Hexagonal Cylinders
SI-74	34100	0.74	Inverse Hexagonal Cylinders

Figure 5.1 shows the coaxial and triaxial arrangements used with a standard electrospinning set-up for this work. We refer the reader to our recent publications for a detailed overview of the electrospinning set up and conditions [20, 21].

5.3.2 Characterization

Scanning electron microscopy (SEM) was conducted using the LEICA 440, for which the samples were coated with Au-Pd. Transmission electron microscopy (TEM) was conducted using the Tecnai T-12. For the TEM images, the nanofibers

a

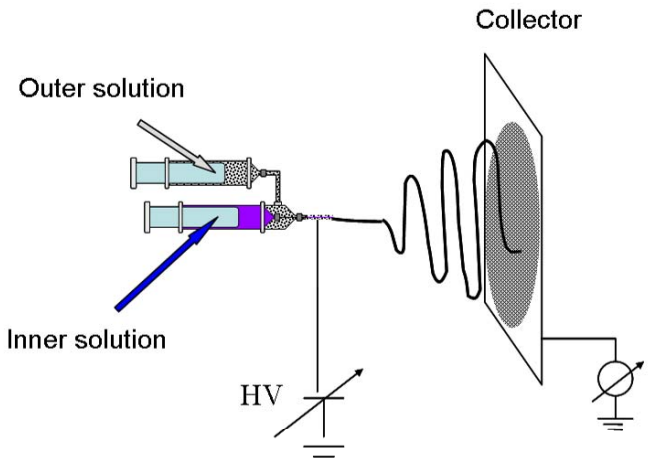

b

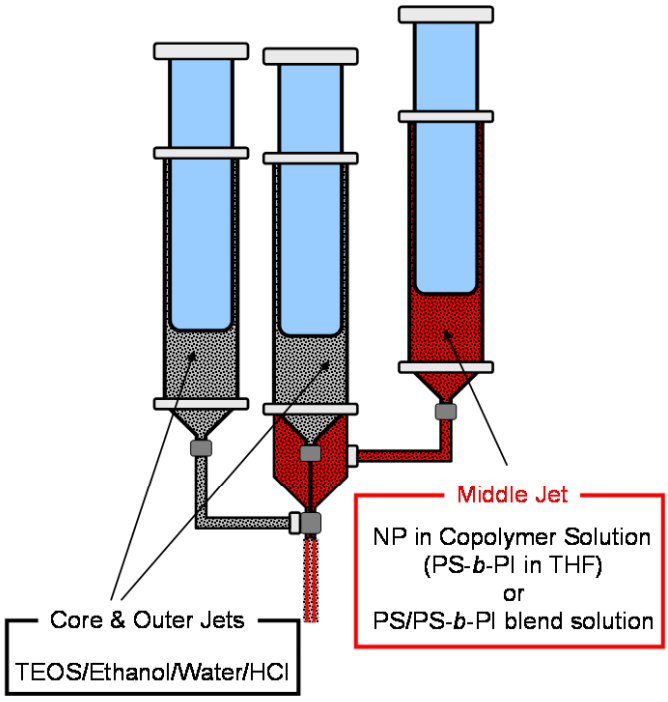

Figure 5.1: a) Coaxial Electrospinning setup. b) Triaxial configuration used in the study. The flow rates of the inner, middle, and outer jets are independently controlled by three micropumps.

were sliced into ~60 nm thick sections using an ultramicrotome along the fiber axis and perpendicular to the axis to view internal structures. All samples were stained with osmium tetroxide to differentiate between isoprene (dark regions) and styrene (light regions) domains. Hence, all the TEM figures presented in below are microtomed images either along the longitudinal or radial direction.

5.4 Results and Discussions

5.4.1 Study of Confined Block Copolymer Self Assembly via Coaxially Electrospun Nanafibers

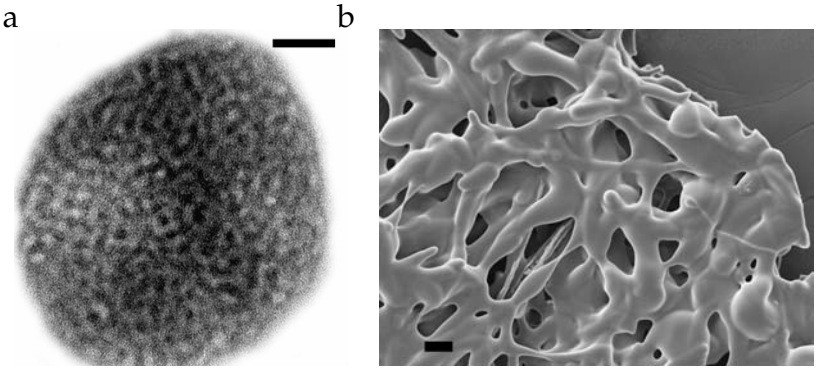

Figure 5.2: a) TEM image of cross-section of as-spun monoaxial SI-33 nanofiber showing disordered morphology; scale bar=100 nm. The dark regions are stained isoprene domains and the light regions are styrene domains, b) SEM image of monoaxial nanofibers annealed at 110^{o}C; scale bar = 20 μm

In order to justify the use of coaxial electrospinning and the silica shell in this work, we first show the TEM image of a cross-section of as-made monoaxial SI-33 fiber in Figure 5.2a. Although the structures are micro-phase separated, they

remain disordered due to the fast solvent evaporation and strong deformation during the electrospinning process [20]. In figure 5.2b, we show a SEM image of the monoaxial fibers annealed above the polymer glass transition (T_g) in an attempt to obtain ordered internal self-assembly and as expected the fibers melt.

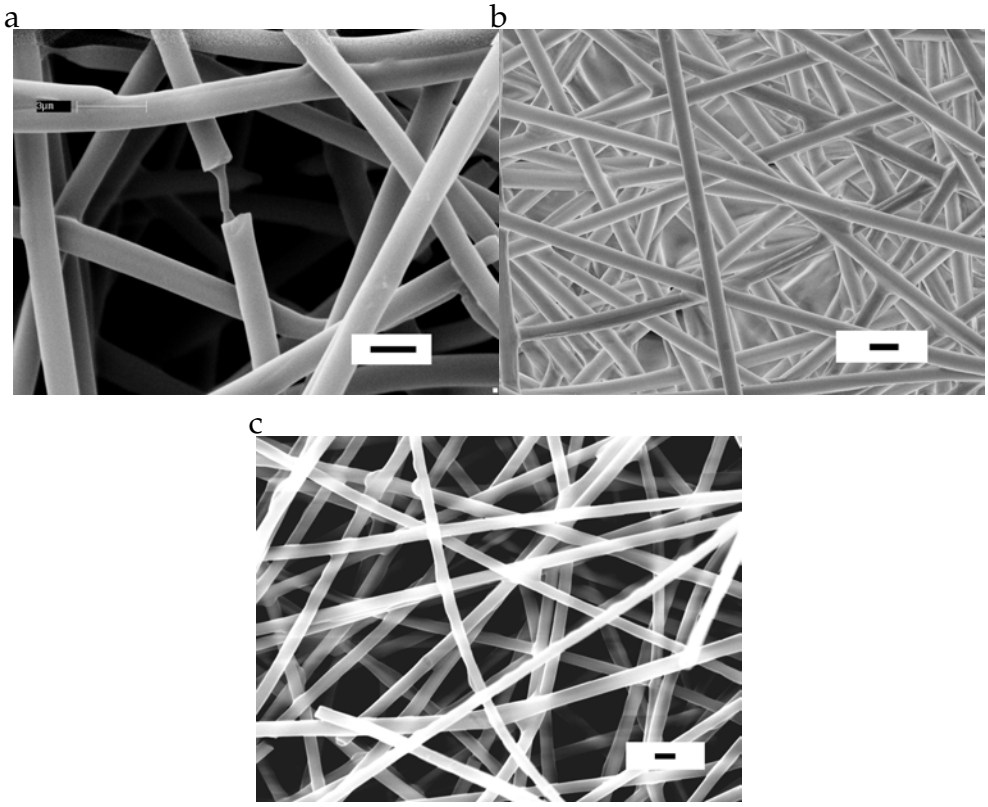

Figure 5.3: a) SEM images of coaxial fibers with silica and poly(styrene-*b*-isoprene) as shell and core respectively a) as spun b) annealed at 125^{o}C for 5 days c) annealed at 175^{o}C for 2 days. All scale bars are 2 μm.

In coaxial fibers the silica shell allows us to anneal the samples at high temperatures to obtain equilibrium morphology. Figure 5.3a shows the SEM image of a typical electrospun coaxial fiber. Figures 5.3b and c show the SEM images of coaxial fibers annealed at temperatures well above the Tg (~100^{o}C). These figures show no leakage of the polymer indicating a good cover of the silica

around the block copolymer fibers providing thermal stability.

All coaxial nanofiber samples shown in this paper were annealed at 175^{o}C for 2 days (post fabrication) to obtain equilibrium morphology. Figure 5.4 shows the annealed fibers spun using SI-09 as the core material. The block copolymer has 0.09 volume fraction of isoprene and forms body centered cubic (bcc) lattice of isoprene spheres in styrene matrix in the bulk (not shown). Figure 5.4 clearly shows the formation of isoprene spheres in styrene in the annealed nanofiber section. As seen from this image and other images shown later, it appears that the matrix domain, styrene, has favorable interaction with the silica shell and therefore prefers to stay close to the interface between core and shell layers. Therefore, we do not see the isoprene spheres lining up close to the silica shell, unlike the TEM images obtained by Ma *et al.* [25].

We then studied the effect of cylindrical confinement on diblock copolymers that form hexagonal cylinders in the bulk. We use two polymers, SI-33 and SI-31 with 0.33 and 0.31 isoprene volume fractions, respectively. For all SI-33 Nanofiber TEM images (Figure 5.5 and Figure 5.6, the structures at the outer edges close to the core-shell interface are lamellar layers (in the form of concentric layers due to cylindrical confinement [21] with the styrene domain next to the silica shell in both cross sections (Figure 5.5) and longitudinal sections (Figure 5.6). In some fiber cross sections, as seen in figure 5.5a, we see hexagonal cylinders as the inner structures (along with the lamellar layers close to polymer-silica interface, as mentioned above). It is worth noting that this polymer, SI-33 forms pure cylindrical morphology in the bulk (see table 5.1). Li *et al.* [26] recently studied different self assembled structures formed by a diblock copolymer in a cylindrical nanopore. They mapped out a phase diagram

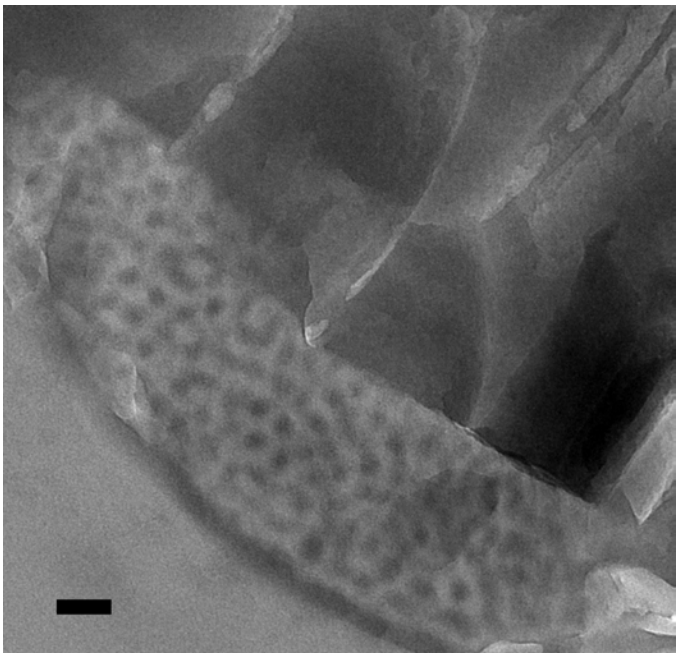

Figure 5.4: TEM image of microtomed cross-section of annealed coaxial fibers with SI-09 as the core material. The dark regions with spherical shapes are stained isoprene domains and the light regions are styrene domains. The outermost dark band is the silica layer. Scale bar=200 nm.

using real-space self consistent field theory. They also found mixtures of lamellae and cylinders for volume fractions that lie within the cylindrical regime in a bulk phase diagram. In addition, they found that most of such intermediate structures were formed for the case where the majority block is attracted to the nanopore wall similar to our system. The mixture of lamellae and cylindrical structures formed in our fibers are consistent with the results they found. (For example, figure 5.5a is similar to the structure LC_{1-6} in Li *et al.*, also formed for volume fractions between 0.3 and 0.4 [26].

Such structures are not formed in the bulk systems and to the best of our knowledge, this is the first time these structures have been found experimen-

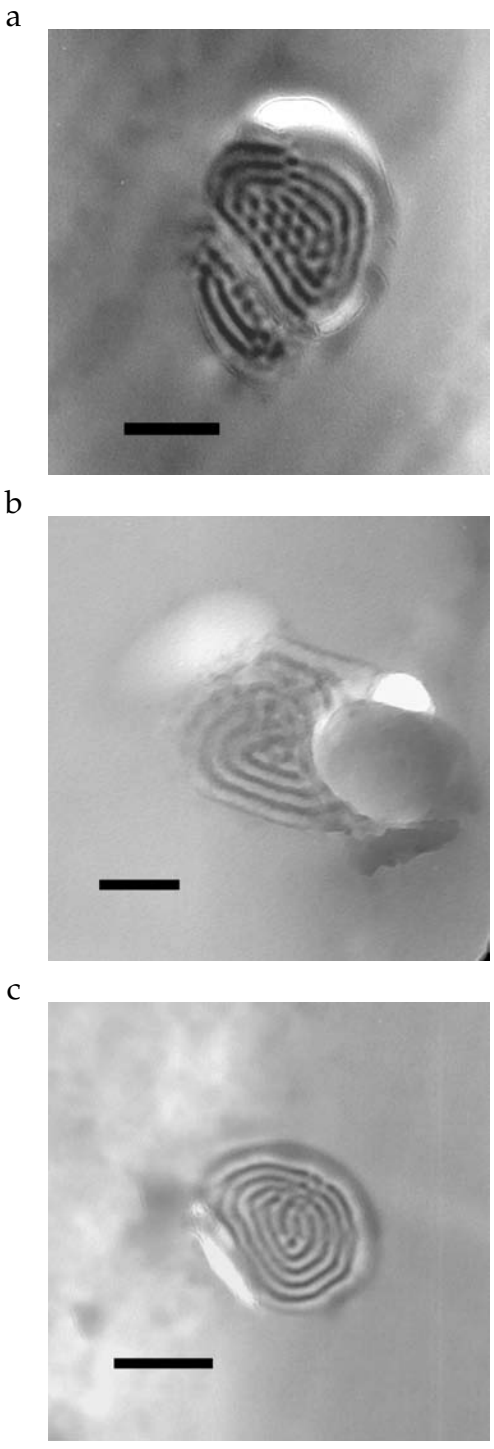

Figure 5.5: TEM images of microtomed cross-sections of annealed (180^{o}C, 2 days) fibers electrospun using SI-33 as the core material. The dark regions are stained isoprene domains, the light regions are styrene domains and the grey outer shell is silica. All scale bars are 200 nm.

tally. Interestingly, we found a few SI-33 fibers with pure lamellar rings (figure 5.5b) and a morphology similar to LC_{LL} [26] (Figure 5.5c). It is very interesting to note how the confinement created by a nanopore can force a pure cylindrical structure in the bulk into concentric lamellar ring morphology. Although, it is hard to provide to concrete explanation of how the same polymer gives different morphologies under cylindrical confinement in the present study, we believe it is the effect of variations in the fiber diameter and the actual temperature conditions each individual fiber is exposed to. One thing consistent in all of these results for SI-33 fibers is the formation of at least some lamellar rings. We anticipate that first the outermost layer coalesces into a single domain of PS due to favorable interactions between the PS domain and the silica wall, then due to the covalent bond between the two blocks the other domain just follows. However, the presence of multiple lamellar rings shows that the lamellar morphology also has lower free energy in the confined state and is not a mere effect of wall interactions. We expect the formation of pure lamellar rings to be more prevalent in smaller pore diameters, as we anticipate that the inner structures in a large diameter fiber would not feel any effect of the confinement and will exhibit bulk morphology.

In the fiber sections along the axis (Figure 5.6), we see isoprene cylinder cross-sections instead of the long cylinders, which indicates the presence of bent isoprene cylinders or helices formed due to the confinement of the silica shell. The helical structure is much clearer in the images we obtained for the annealed SI-31 polymer. Here in Figure 5.7a), we see pure cylindrical morphology. Pure cylindrical structures are not found in any SI-33 fibers probably due to the higher PI volume fraction in SI-33 than in SI-31. If we look at Figure 5.7a) more closely, we find that isoprene cylinders form a pentagon (not hexagon), a

structure absent from any bulk phase diagram.

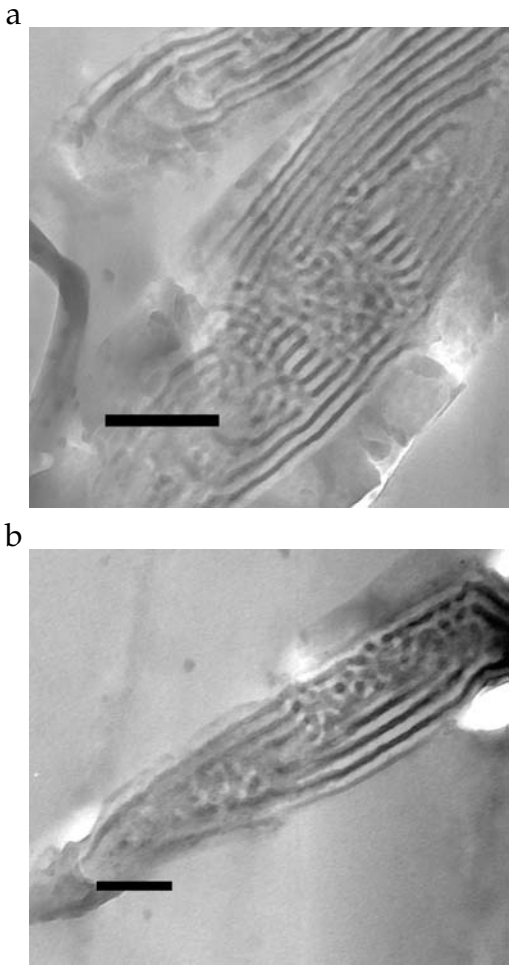

Figure 5.6: TEM images of microtomed longitudinal sections of annealed (180^{o}C, 2 days) fibers electrospun using SI-33 as the core material. All scale bars are 200 nm.

This, again, is an effect of the cylindrical confinement and is also seen in the phase diagram as LC_{1-5} by Li and Wickham [26]. We do find some SI-33 fibers with mixtures of lamellar and cylindrical morphology as well, though pure lamellar rings are not seen, unlike SI-33 fibers, demonstrating how the increasing volume fraction of isoprene in SI-33 compared to SI-31 favors lower curvature structures [26]. Figures 5.7b and c show the intermediate structures

similar to LC_4 (with only 4 isoprene cylinders) and LC_{LL} in Li and Wickham [26] phase diagram respectively. The SI-31 fiber sections cut along the axis in Figure 5.8 show mixtures of straight and curved cylinders evident from isoprene cylinder dots. In a study done by Wu *et al.* [27], it was found that the stresses imposed by confinement cause the cylinders to bend around the pore axis and form helices and doughnut type structures. Our longitudinal self assembly structures match very well with the images shown by Wu *et al.* [27]. Previous studies where helices have been found due to cylindrical confinement have used a much smaller pore size than our fibers. Our study shows that cylindrical pores even as large as 8-10 times the lamellar spacing can impose large enough stresses to significantly affect the self assembly of block copolymers. This work demonstrates that electrospun fibers provide a good template to study the effects of cylindrical confinement on self assembling materials such as block copolymers.

5.4.2 Using Block Copolymer Assembly as Template to Guide Nanoparticle Location within Nanofibers

To provide functionality to such self assembled materials, we incorporated magnetite nanoparticles into the PS-*b*-PI core. In addition, this study serves as a method to understand the effects of processing conditions during electrospinning on nanoparticle (NP) location and to explore if these effects can be used to an advantage for tailoring nanoparticle placement within nanofibers. Monodisperse magnetite NPs (4 nm) were synthesized and surface coated with oleic acid to provide slight selectivity towards isoprene domain, while preserving their

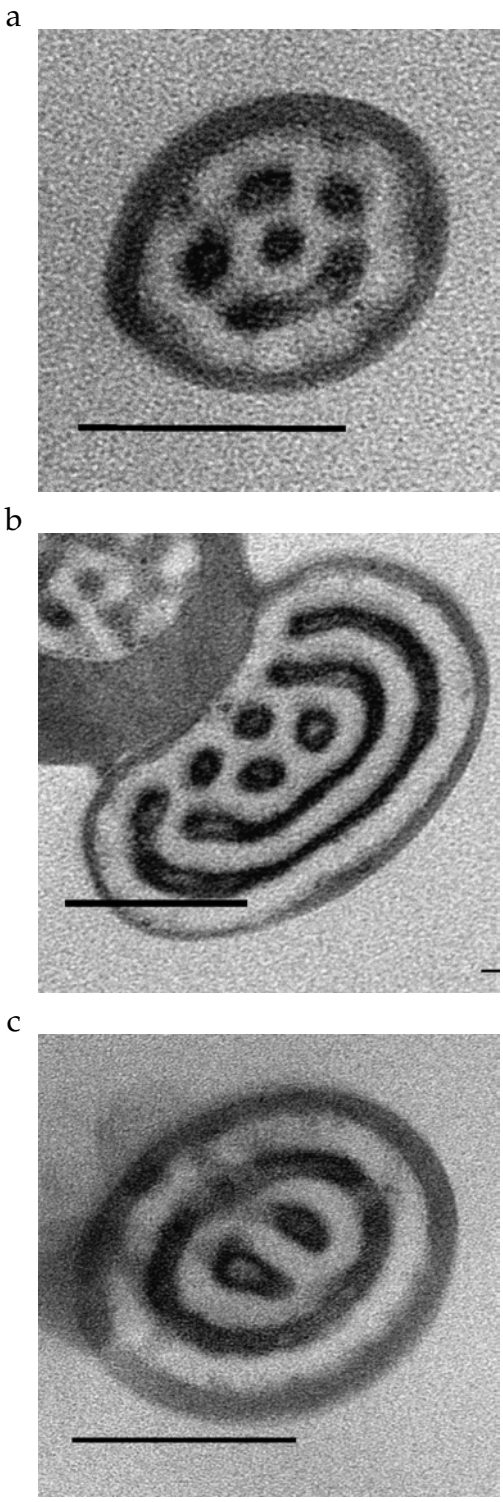

Figure 5.7: TEM images of microtomed cross-sections of annealed (180^{o}C, 2 days) fibers electrospun using SI-31 as the core material. All scale bars are 100 nm. The outermost gray region in each image is the silica skin layer.

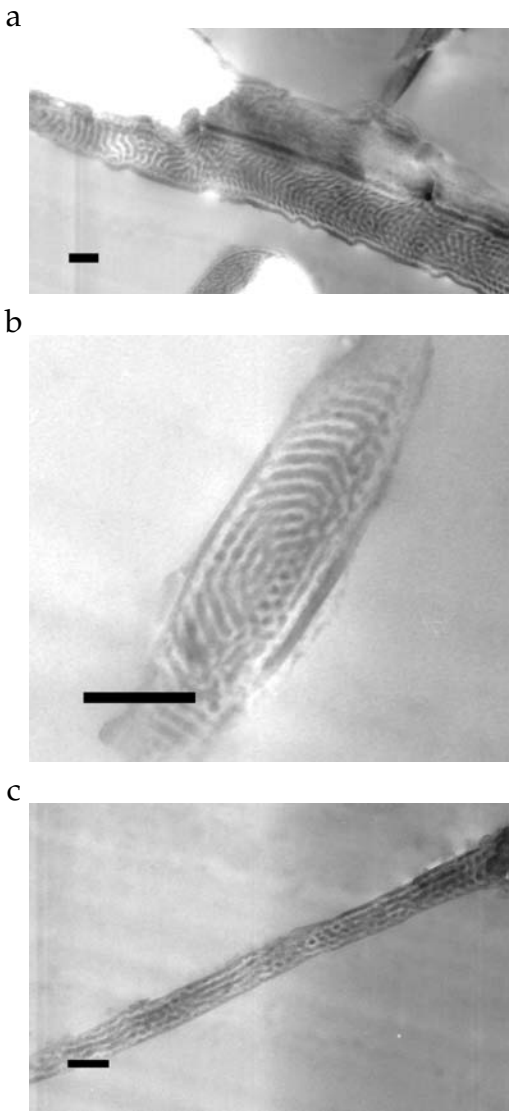

Figure 5.8: TEM images of microtomed longitudinal sections of annealed (180^{o}C, 2 days) fibers electrospun using SI-31 as the core material. All scale bars are 200 nm.

magnetic properties [28, 29]. Magnetite nanoparticles have been shown to display superparamagnetic behavior due to their small size making them ideal for magnetic field driven transport of drugs and bioseparations. Figure 5.9 shows the TEM images of sections cut perpendicular to and along the axis of a fiber electrospun using SI-19 with 0.05 weight fraction of magnetite nanoparticles. For the nanocomposite fiber study, we only use SI-19, that forms pure cylindrical morpohlogy both in the bulk and in nanofibers. The nanoparticles (black dots in TEM images) are selectively and uniformly dispersed in the PI phase. As suggested by previous work and solubility analysis [28, 29], the selectivity is due to the presence of oleyl groups on the particle surface. No evidence of magnetic particle aggregation was found in the TEM images. Previous studies on films of the same system have shown that aggregates of nanoparticles form beyond a weight fraction of 0.02 [29]. We anticipate that the strong deformation and fast solvent evaporation during the electrospinning process prevent the aggregation of magnetite nanoparticles even at such high particle loadings. We refer the reader to our recent publications for discussion on the effect of electrospinning conditions on nanoparticle dispersion and selectivity [28, 32]. Although it is not shown here, similar experiments with 0.1 weight fraction of quantum dots (Cadmium Sulphide, also coated with oleic acid) produced similar self assembly with NPs uniformly dispersed in the isoprene domain.

With the freedom to vary nanoparticle surface coating, block copolymer self assembly, processing conditions (e.g. deformation rate) and nanoparticle size, among other parameters, these results demonstrate the possibility of developing an entire spectrum of multifunctional materials with precisely controlled self assembly. This work provides a robust methodology to fabricate high surface area multifunctional nanocomposites including cases where particle-

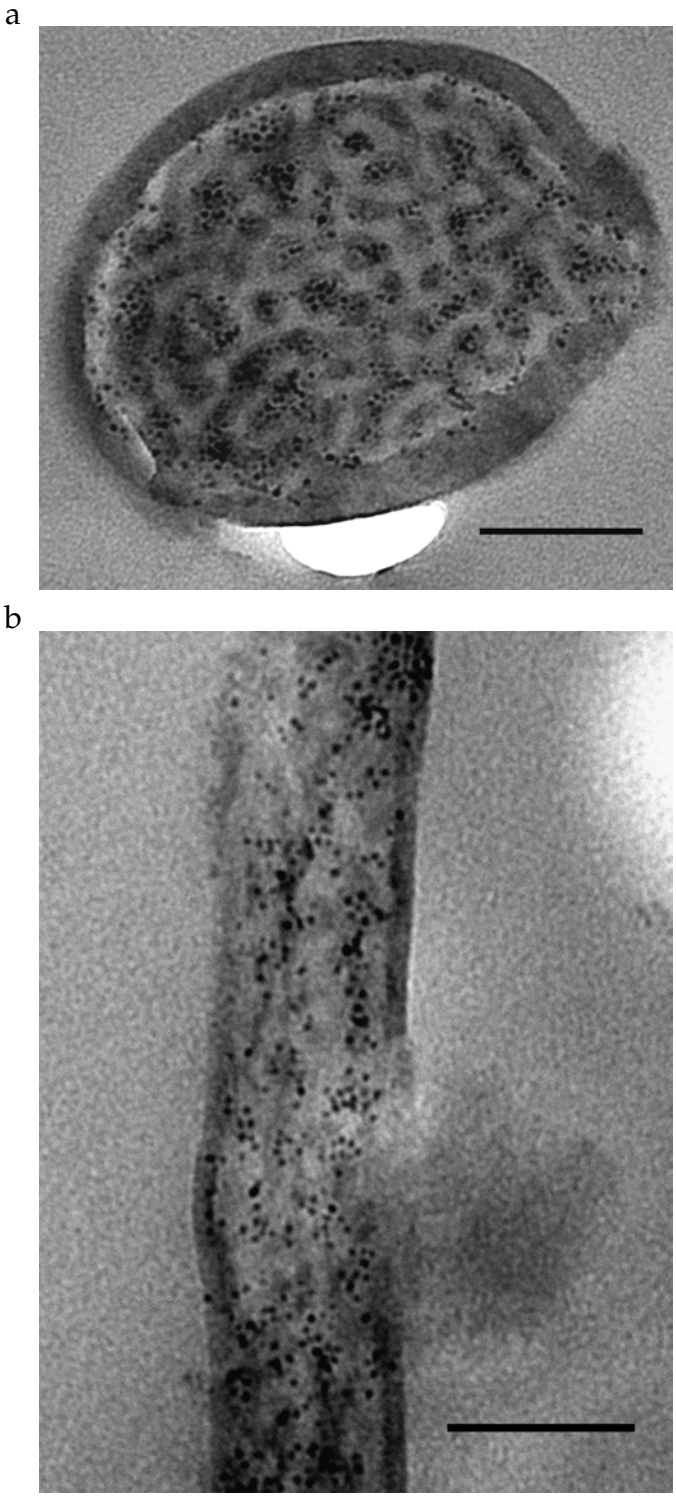

Figure 5.9: TEM images of annealed coaxial bulk cylinder forming PS-PI SI-19/magnetite NP fibers. The scale bars are 100 nm.

particle interactions are dominant. This would be particularly helpful in cases where surface functionalization of nanoparticles can lead to loss of material properties, such as catalytic particles or carbon nanotubes (for electrical property enhancement). The success of alternate methods such as deformation in preventing NP aggregation will lead to the path towards next generation functional materials.

5.4.3 Triaxial Electrospinning

As mentioned before, we conducted a new study on fabrication of triaxial nanofibers, with silica in both the innermost and outermost shells/layers and a self assembling polymeric material in the middle layer. We considered two cases with different materials in the middle layer. In the first, we fabricated nanofibers with block copolymer and nanoparticles in the middle layer. With this type of system, we hope to study the effect of confinement (on both sides, unlike coaxial nanofibers) on block copolymer self assembly and the effect of the presence of nanoparticles on block copolymer assembly within nanofibers. Figures 5.10 a, b and c show the cross-sections of annealed triaxial nanofibers using SI-28 as the block copolymer with increasing magnetite nanoparticle loading. TEM images clearly the formation of triaxial nanofibers with silica as the innermost and outermost layers and block copolymer with magnetite as the middle layer. These results also demonstrated the incorporation of magnetite nanoparticles (coated with oleic acid) selectively into the isoprene domain in the block copolymer layer. Here, the BCP layer thickness is only $\sim$ 40 nm and is indeed comparable to the block copolymer domain size and only a single domain fits into the available confined space. It is appears that the isoprene phase

with magnetite shows a preference to the silica walls, and thus most of isoprene and magnetite migrate to both inner and outer interfaces with silica. This is opposite to what we observe in the case of pure block copolymers, where styrene shows a preference for the wall. This aspect needs to be studied in more detail to understand the specific interactions of different blocks with the silica wall and how these interactions change with the presence of nanoparticles. A further study on these aspects is underway.

In the second case, the PS-*b*-PI block copolymer (SI-74) with PS hexagonal morphology (in the bulk) was mixed with polystyrene homopolymer (*Mw* = 13,000) (PS-*b*-PI:PS = 65:35), and was placed as the middle layer in triaxial electrospinning. In this system the PS domain in the block copolymer is the cylinder-forming minor phase, and the addition of PS homopolymer leads to a symmetric composition. The questions that can be raised here are i) Can the cylinder-forming PS-*b*-PI and PS homopolymer blend system form the confined assembly structures similar to symmetric block copolymers in electrospun nanofibers, and ii) How does the presence of PS homopolymer affect the interactions with the silica wall?. Again the presence of silica shell allowed us to anneal the materials and investigate the formation of equilibrium structures. Figure 5.11 shows the TEM images of microtomed triaxial fiber sections. Again, the middle layer thickness is only ~ 40 nm and is indeed comparable to the block copolymer domain size and only a single domain fits into the available confined space. These TEM images suggest that the isoprene phase prefers to the silica walls, and most of isoprene migrates to both inner and outer interfaces with silica, while the styrene phase resides between the isoprene phases. This is opposite to what we observe in the case of symmetric copolymers, where styrene shows a preference for the silica wall in the concentric ring morphology [21, 28].

a

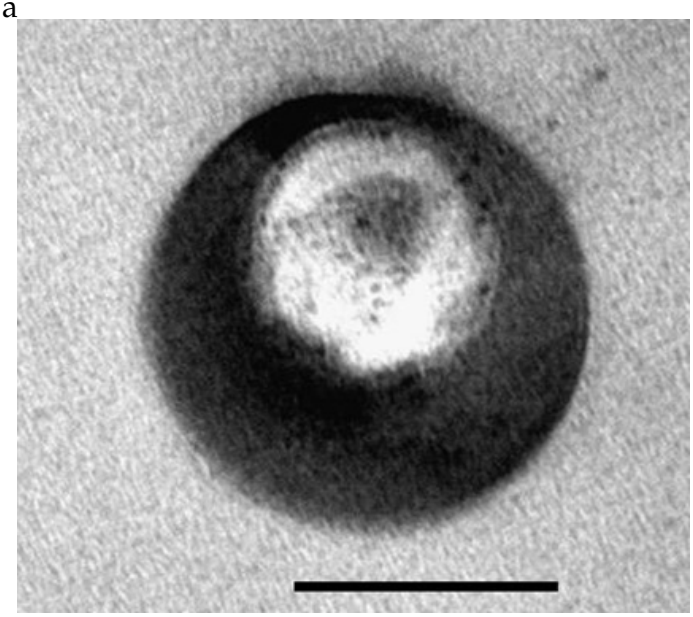

b

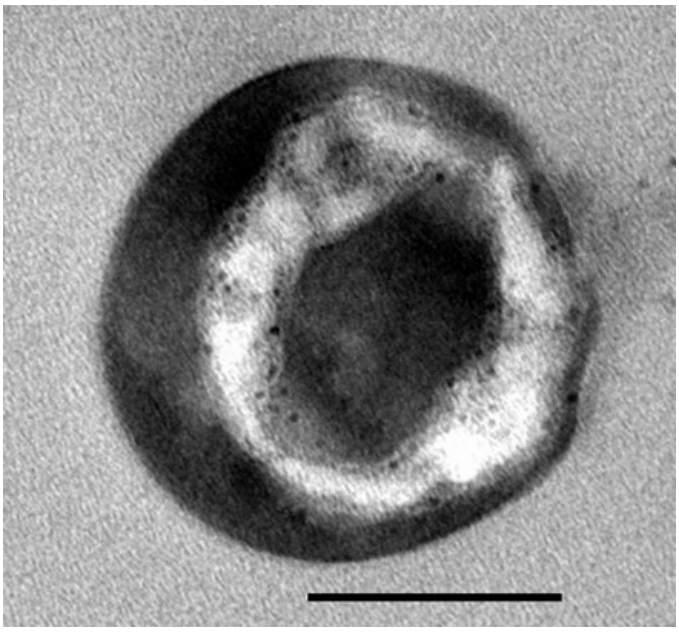

Figure 5.10: TEM image of cross-section of triaxial nanofiber with SI-28/magntite NPs sandwiched between two silica layers. The samples are annealed at 150^{o}C for 72 hours. The scale bar is 100 nm.

This aspect needs to be studied in more detail to understand the specific interactions of different blocks with the silica wall and how these interactions change with the presence of nanoparticles or the PS homopolymer. Further study on these aspects is also underway. Nonetheless, block copolymer/homopolymer systems offer a useful means to alter the assembly at the interface with silica.

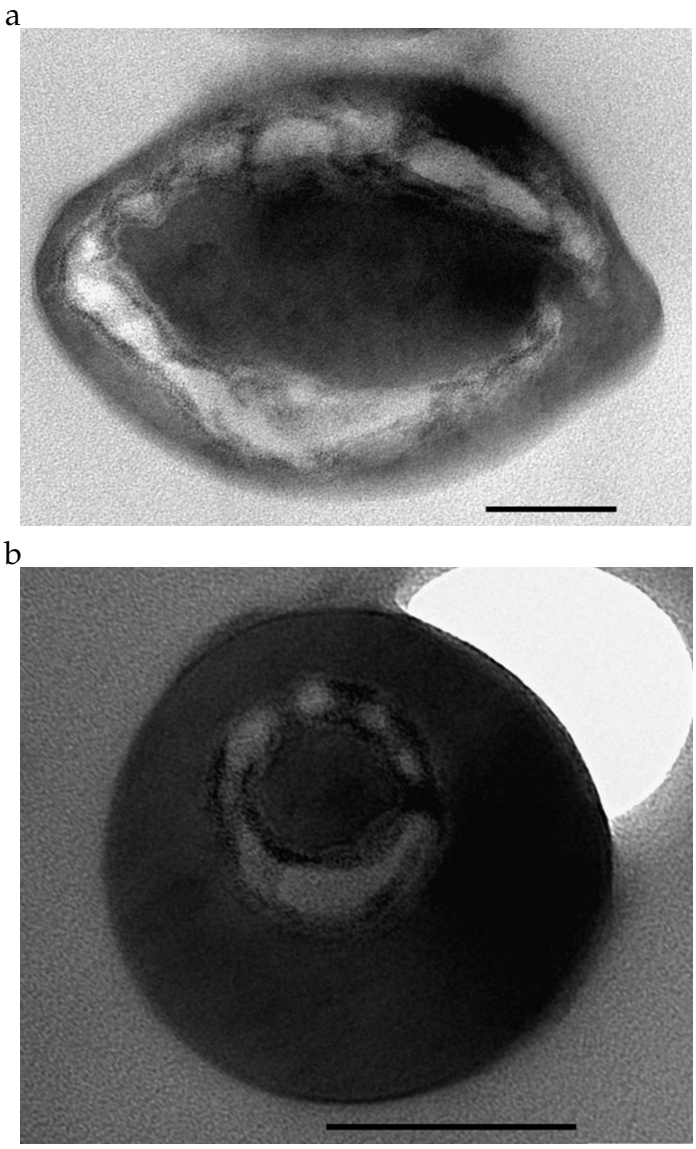

Figure 5.11: TEM images of cross-sections of as-made triaxial nanofibers SI-74/PS sandwiched between two silica layers. The samples are annealed at 150^{o}C for 48 hours. The scale bars are 100 nm.

Through our work on triaxial electrospinning, we have demonstrated the ability to develop multiaxial nanofibers with different combinations of materials. A more detailed and systematic study on effect of fiber diameter, wall interactions, nanoparticle inclusion etc. is underway. Such multi-layered materials provide a unique platform to study the effect of confinement and wall interactions on self assembly. Furthermore, hollow porous nanofibers, with potential applications in drug delivery can be formed after the dissolution of silica layers and the minor BCP phase. With the use of cylinder forming block copolymers, multichannel nanotubes can also be developed. Compared to single channel, multichannel structures may possess considerable advantages such as independent addressable channels, mechanical stability and larger surface to volume ratios [bio-mimic]. Potential applications of such materials include bio-mimic super-lightweight thermoinsulated textiles, vessels for nanofluidic devices, and multicomponent drug delivery. Moreover, the use of block copolymers to fabricate these multi-structured materials allows for an unprecedented control on pore/channel size and shape or on nanoparticle location in case of composites.

5.5 Effect of Cylindrical Confinement on Block Copolymer Self Assembly using Computational Simulations

Coarse-grained molecular dynamics simulations were conducted to study the effect of cylindrical confinement on block copolymer self assembly. The coarse graining methodology and the overall MD scheme used was similar to our previous simulation works [32, 34]. To study the confinement effect, we constructed a wall using the same beads as those used in the polymeric bead-spring model,

except now these beads are fixed at their initially defined lattice positions and do not move with time. The MD simulation box now consists of periodic boundary conditions only along the z-axis (or length of the cylinder). The distance between adjacent beads in the wall is kept fixed at 1.06 MD length units. To initialize the system, we used soft interaction potentials from Kremer and Grest [35] till the number of particles crossing the wall reduced to zero. We did preliminary work on both pure block copolymer and block copolymer/NP composite systems. For both cases, we modeled the system in such a way that block *A* in the *A*-*B* diblock copolymer has a selectivity towards the wall (*W*). *A*-*A*, *B*-*B*, and *A*-*W* interactions are defined using Lennard Jones (LJ) potential cut and shifted at a distance =2.5 MD units, while for *A*-*B* and *B*-*W* interactions, LJ potential is cut and shifted at a distance of $2^{1/6}$ MD units. We refer the reader to our recent publications for details of these potentials [32, 34]. For the case of nanocomposites, we study "selective nanoparticles". Here the nanoparticles (NP) preferentially wet the *B* domain. To do so, we use a cut off distance =2.5 for *B*-*P* interactions and a cut off distance =$2^{1/6}$ for *A*-*P* and *P*-*W* interactions. Such a interaction potential scheme is similar to our experimental system where the styrene block prefers the wall, while the nanoparticles prefer to stay in the isoprene domain.

5.5.1 Block Copolymer Melts under Cylindrical Confinement

Unlike the bulk phase diagram, we do not expect the confined phase diagram to be symmetric. Here it might be critical whether the block that wets the wall is the matrix domain or the minority domain. To study this effect, we investigated a range of *A*-block volume fractions from 0.2 to 0.8. Figure 5.12 shows

the simulation snapshot for a symmetric diblock copolymer with a 0.5 volume fraction of both blocks. Alternate concentric rings of block *A* and *B* are formed due to cylindrical confinement. This is consistent with our experimental results in electrospun PS-*b*-PI nanofibers [21]. In addition, we note that the *A*-domain width is the smallest adjacent to the wall. This is possibly because the cylinder diameter is not commensurate with the natural domain spacing of the diblock copolymer, therefore the outer layers, where the confinement is most prominent shrink.

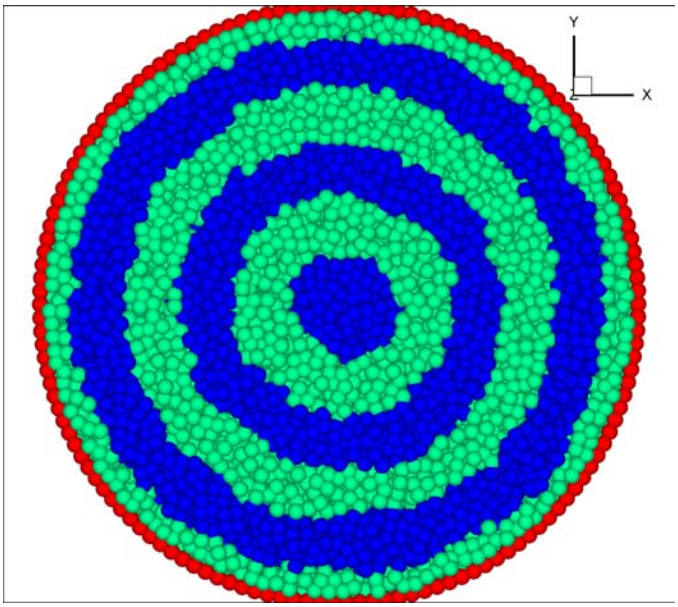

Figure 5.12: 2D Simulation snapshot of symmetric diblock copolymer under cylindrical confinement. The length of the confining cylinder extends into the paper. The red beads represent the wall, the green ones are block *A* beads and the blue ones are block *B* beads. *A* block preferentially wets the wall.

Figure 5.13 shows simulation snapshots of 0.4 and 0.6 *A*-block volume fraction. Again we see alternate concentric rings of the two blocks due to cylindrical confinement. In part a), the *A*-domain size reduces due to the lower volume fraction, while the *A*-domain size is larger in part b). Again, we find that the

domain size is smallest close to the wall.

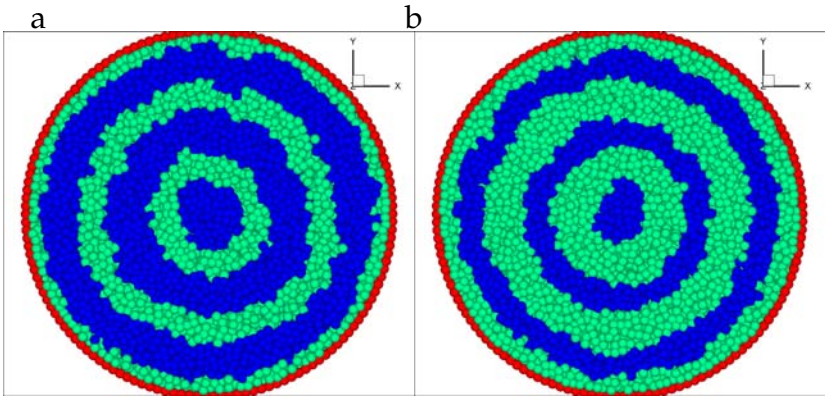

Figure 5.13: 2D Simulation snapshots of asymmetric diblock copolymers under cylindrical confinement. a) 0.4 *A*-volume fraction, b) 0.6 *A*-volume fraction. The length of the confining cylinder extends into the paper. The red beads represent the wall, the green ones are block *A* beads and the blue ones are block *B* beads. *A* block preferentially wets the wall.

Figure 5.14 shows simulation snapshots of 0.3 and 0.7 *A*-block volume fraction. In the bulk system, such volume fractions exhibit hexagonal cylindrical morphology as seen in literature using experiments, simulations and theory. However, we find here that there is a tendency to form lamellar rings on the outer edges and as we move towards inner structures, cylinders of minor block are formed. This effect is expected to be a result of both the favorable interaction of one block to the wall and cylindrical confinement. Formation of such hybrid structures is similar to what we saw above in electrospun nanofibers. In addition, consistent with our results above and the work by Li *et al.* [26], there appears to be a greater tendency to form such hybrid structures when the majority block likes the wall (in part b). One thing we'd like to point out here is, that although these lamellar rings on the outer edges appear to be broken, they are joint together as we go deeper along the length of the confining cylinder.

At this point, it is hard to comment whether this is an artifact of the simulation parameters, or its an effect of the confinement. A detailed study by using longer simulation box is needed to understand this aspect. Also, the minor block cylinders seen in the center are not totally separated at all depths, again due to the use of smaller simulation box length.

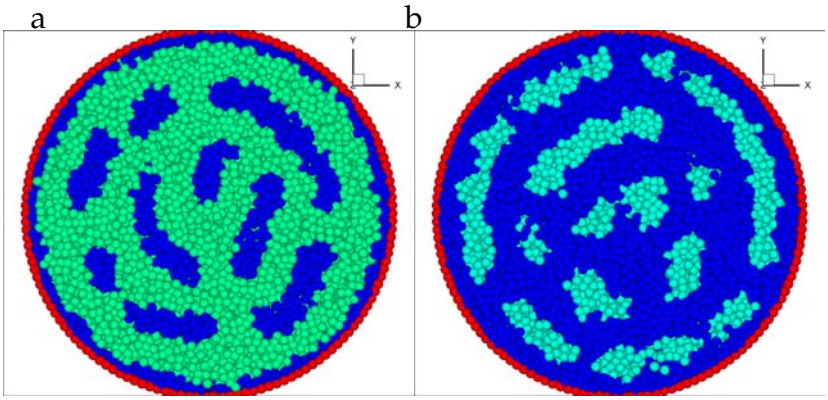

Figure 5.14: 2D Simulation snapshots of asymmetric diblock copolymers under cylindrical confinement. a) 0.3 *A*-volume fraction, b) 0.7 *A*-volume fraction. The length of the confining cylinder extends into the paper. The red beads represent the wall, the blue ones are block *A* beads and the green ones are block *B* beads. *A* block preferentially wets the wall.

Figure 5.15 shows simulation snapshots of 0.2 and 0.8 *A*-block volume fraction. Here we find purely cylindrical morphology consistent with our experimental results above for similar volume fractions. The hexagonal lattice structure is not seen due to the confinement. Again, we would like to point out here is that the minor block cylinders are not totally straight along the entire depth of the confining cylinder and are joint at certain *z*-locations. This needs to be studied in more detail with longer simulation box to avoid simulation artifacts. Furthermore, the system could be annelaed at high temperatures to form equilibrium morphology.

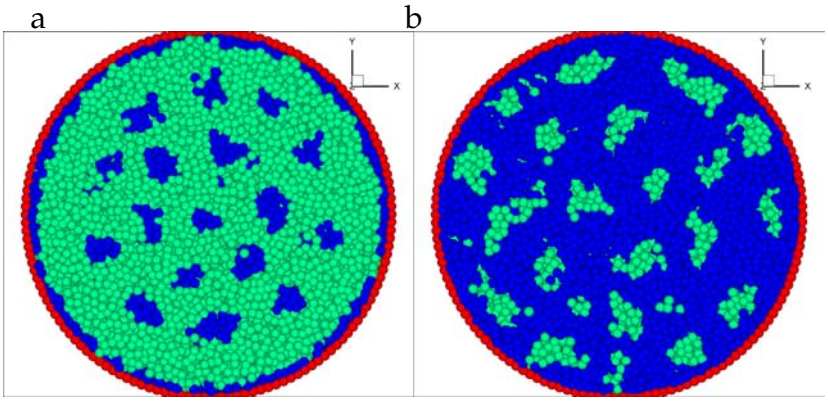

Figure 5.15: 2D Simulation snapshots of asymmetric diblock copolymers under cylindrical confinement. a) 0.2 *A*-volume fraction, b) 0.8 *A*-volume fraction. The length of the confining cylinder extends into the paper. The red beads represent the wall, the blue ones are block *A* beads and the green ones are block *B* beads. *A* block preferentially wets the wall.

5.5.2 Block Copolymer/Nanoparticle Composites under Cylindrical Confinement

As mentioned above, we use selective NPs that preferentially wet the *B*-domain. We first use a diblock copolymer with *A*-volume fraction of 0.4 with respect to the diblock copolymer and we add different fractions of nanoparticles (0.05, 0.1, 0.15 and 0.3) with respect to the entire nanocomposite. As seen above, the pure block copolymer with 0.4 *A*-fraction forms concentric lamellar morphology. Figure 5.16 shows snapshots of systems with NP volume fraction of 0.05, 0.1 and 0.3 respectively. For parts a) and b), the global volume fraction of combined *B* and NPs with respect to the entire system is 0.62 and 0.64 respectively. Due to this increase in the volume fraction, lamellar rings are not completely formed. Part a) appears to almost form lamellar rings, while the structure in part b) is similar to what we experimentally saw in figure 5.7c. For figure 5.16c, the

global volume fraction of combined B and NPs with respect to the entire system is 0.72 and therefore the morphology transitions from lamellar rings to cylinder-like morphology. Again, the hexagonal lattice is not seen due to the confinement.

Figure 5.17 shows the concentration profiles of the above systems with NP volume fraction of 0.1 and 0.15. Here the systems form lamellar ring morphology. The concentration peak values increase as we move towards the wall due to the increasing circumference and therefore increasing number of particles or beads per unit distance along the diameter. The NPs, as expected, stay only in the B-domain and exhibit a zero concentration in the A-domain. In addition, we note that the NPs have a tendency to place themselves at the center of the A-domain and therefore exhibit a concentration peak at this location. This is similar to what we have found in bulk systems previously. Since the nanoparticle size used in this study is comparable to the radius of gyration of the polymer chains, the chains prefer to push the particles away towards the chain ends (at the center of the domain) to prevent any loss of configurational entropy [34].

Lastly, we studied a system with A-volume fraction of 0.7 with respect to the diblock copolymer and 0.14 volume fraction of nanoparticles with respect to the entire nanocomposite (figure 5.18). The pure block copolymer with this composition forms hybrid structures as seen in figure 5.14. Here, the global volume fraction of combined B and NPs is 0.4 and therefore transitions into a lamellar ring morphology. The concentration profile again shows a NP concentration peak at the center of the B-domain.

To conclude, interesting self assembly structures have been seen under cylindrical confinement, including some that we experimentally found in electro-

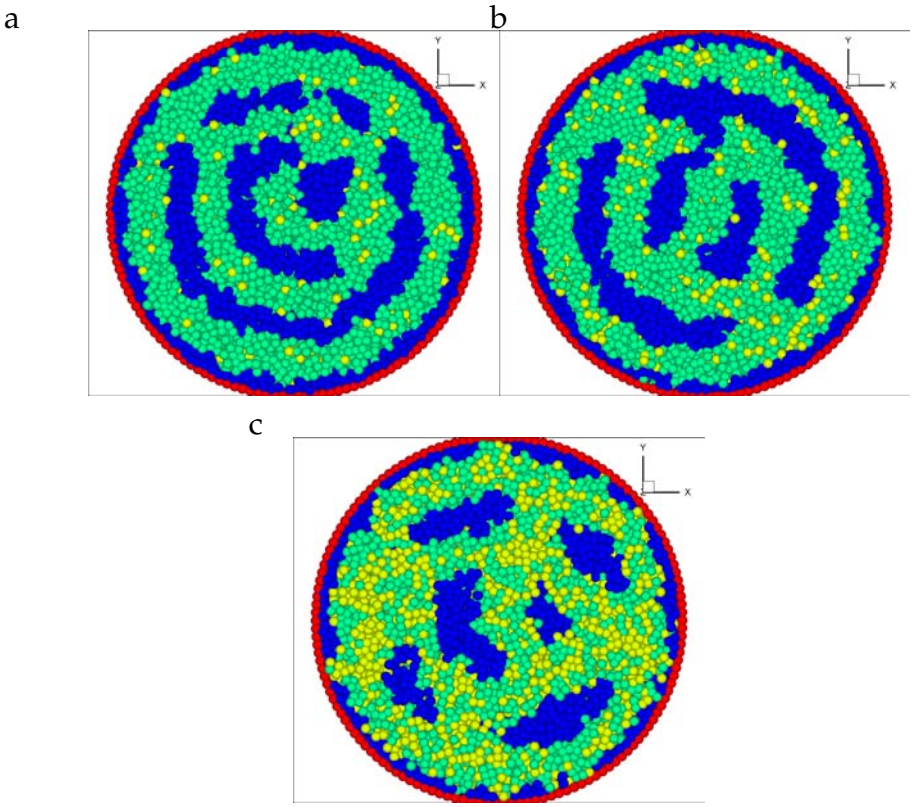

Figure 5.16: 2D Simulation snapshots of asymmetric diblock copolymer/NPs under cylindrical confinement. The block copolymer used has 0.4 volume fraction of *A*-block with respect to the block copolymer. a) 0.05 NP volume fraction with respect to the entire nanocomposite system, b) 0.1 NP volume fraction with respect to the entire nanocomposite system, c) 0.3 NP volume fraction with respect to the entire nanocomposite system. The length of the confining cylinder extends into the paper. The red beads represent the wall, the blue ones are block *A* beads, green ones are block *B* beads and yellow represents the nanoparticles. *A* block preferentially wets the wall.

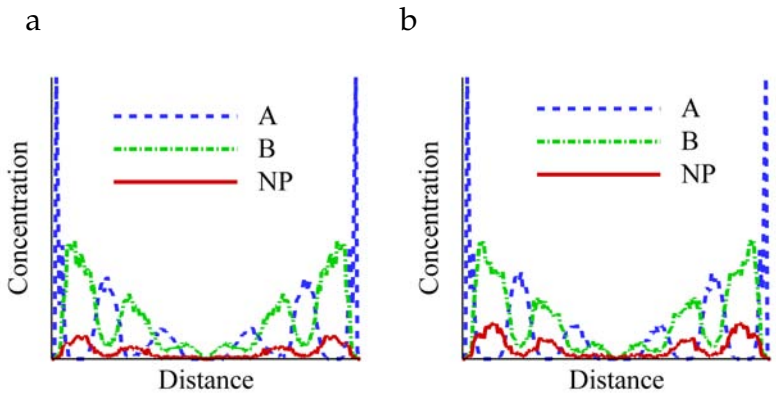

Figure 5.17: Concentration profile of blocks *A*, *B* and NPs along the diameter of the confining cylinder. a) NP volume fraction=0.1, b) NP volume fraction =0.15. Both form lamellar rings as seen in snapshots above. The system is same as figure 5.16.

spun nanofibers. Study of additional systems by varying the interaction potentials between different components and ratio of wall radius:domain spacing would be extremely useful. The absence of totally straight minor block cylinders along the length of the confining cylinder could be a result of one or both of the following two possible reasons, 1) the structure formed here is indeed the lowest free energy state under confinement (this structure in such a scenario should change if the ratio of polymer R_{gyr}: cylinder diameter is altered), 2) the structure is stuck in a metastable state and is a simulation artifact possibly due to the use of insufficient simulation box length. This needs to be studied in more detail with the use of larger box length and also by varying the ratio mentioned above. Study of systems with block copolymer sandwiched between two cylindrical walls could further add to the richness of the phase diagram. Such a system would serve as a predictive tool for fabrication of hollow porous nanofibers using triaxial nanofibers with self assembling block copolymer as the middle layer.

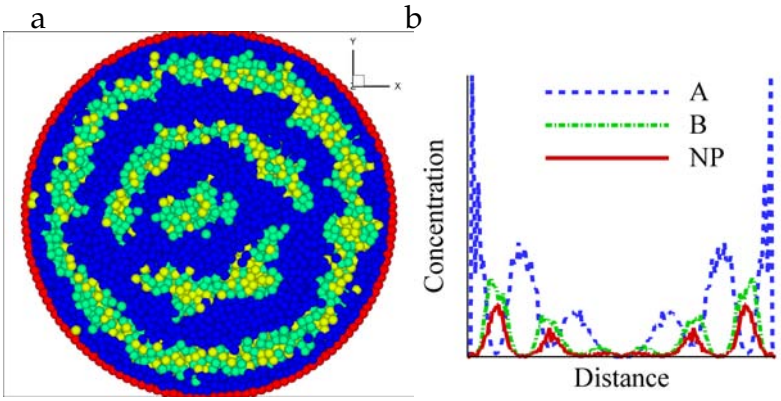

Figure 5.18: Asymmetric diblock copolymer/NPs under cylindrical confinement. The block copolymer used has 0.7 volume fraction of *A*-block with respect to the block copolymer and 0.14 NP volume fraction with respect to the entire nanocomposite system. a) 2D simulation snapshot. The length of the confining cylinder extends into the paper. The red beads represent the wall, the blue ones are block *A* beads, green ones are block *B* beads and yellow represents the nanoparticles. *A* block preferentially wets the wall. b) concentration profile.

5.6 Conclusions

In this work, we have presented a systematic methodology to develop multiaxial block copolymer nanofibers with confined self assembly. Effect of cylindrical confinement has been first studied on self assembly of asymmetric PS-*b*-PI with varying volume fractions of isoprene using coaxial electrospinning. A rich series of hybrid, self assembly structures have been obtained. These materials provide a great platform to control nanoparticle location within nanofibers for effective utilization in applications such as catalysis, sensing and smart textiles. Such example has been demonstrated by selectively placing magnetite nanoparticles in the isoprene domain of PS-*b*-PI nanofibers. Through this work, we demonstrated a novel methodology to combine the functionalities of block copolymer self assembly with the advantages of nanofiber mats (e. g. high sur-

face area, open pore structure, ability to be woven into a fabric) [2] to widen the scope of potential applications. Furthermore, we found that the strong deformation and fast solvent evaporation during electrospinning helps prevent nanoparticle aggregates. Good control over location of magnetic nanoparticles at such high loading opens up a plethora of potential future applications including electromagnetic shielding, high density memory, magnetic recording, drug delivery and separation aids. Further addition of quantum dots can be potentially helpful in bioseparation applications. For example, with selective dissolution of the styrene domain and fluorescent (quantum dots) and magnetic nanoparticles incorporated into the walls of the fiber structure can help fabricate next generation bioseparation devices for early detection of diseases. Here, dissolution of styrene domain will increase the functional surface area of the nanofiber mats by many folds, the magnetic nanoparticles will allow more sensitive magnetically assisted separation of biomolecules and the fluorescent nanoparticles will provide a sensitive marker for counting the separated cells using fluorescence imaging. In addition, we demonstrated the ability to fabricate triaxial nanofibers, where different self assembling polymeric materials are confined on both sides by silica layers. Interesting self assembly has been observed due to the small width of the middle layer and presence of silica on both sides. This methodology can serve as a simpler and more controlled way to produce bio-mimic multichannel microtubes [33]. Our study on triaxial nanofibers raises some intriguing questions regarding interaction effects in confined blends and composites and further work to understand these systems is underway.

BIBLIOGRAPHY

[1] Li, B.D.; Xia, Y. *Adv. Mater.* **2004**, 16, 1151.

[2] Dzenis, Y. *Science* **2004**, 304, 1917.

[3] Loscertales, I.G.; Barrero, A.; Guerrero, I.; Cortijo, R.; Marquez, M.; Ganan-Calvo, A.M. *Science* **2002**, 295, 1695.

[4] Sun, Z.; Zussman, E.; Yarin, A.L.; Wendorff, J.H.; Greiner, A. *Adv. Mater.* **2003**, 15, 1929.

[5] Yu, J.H.; Fridrikh, S.V.; Rutledge, G. C. *Adv. Mater.* **2004**, 16, 1562.

[6] Li, B.D.; Xia, Y. *Nano Letters*. **2004**, 4, 933.

[7] McCann, J. T.; Marquez, M; Xia, Y. *Nano Letters* **2006**, 6, 2868.

[8] Panels, J. E.; Joo, Y. L. *Journal of Nanomaterials* **2006**, 41327.

[9] Khandpur, A.K. *et al*. *Macromolecules* **1995**, 28, 8796.

[10] Bates, F.S.; Fredrickson, G.H. *Annu. Rev. Phys. Chem.* **1990**, 41, 525.

[11] Matsen, M.W.; Schick, M. *Phys. Rev. Lett.* **1994**, 72, 2660.

[12] Fredrickson, G.H.; Bates, F.S. *Annu. Rev. Mater. Sci.* **1996**, 26, 501.

[13] Almdal, K.; Koppi, K.A.; Bates, F.S.; Mortensen, K. *Macromolecules* **1992**, 25, 1743.

[14] Park, C.; Yoon, J.; Thomas, E. L. *Polymer* **2003**, 44, 6725.

[15] Sota, N.; Hashimoto, T. *Polymer* **2005**, 46, 10392.

[16] Hoffman, A.; Sommer, J.; Blumen, A. *J. Chem Phys.* **1997**, 106, 6709.

[17] Fraser; Denniston; Muser *J. Poly. Sc. Part B* **2005**, 43, 970.

[18] Srinivas, G.; Discher, D.; Klein, M.L. *Nature Materials* **2004**, 3, 638.

[19] Groot, R.D.; Madden, T.J.; Tildesley, D.J. *J. Chem. Phys.* **1999**, 110, 9739.

[20] Kalra, V.; Kakad, P. A.; Mendez, S.; Ivannikov, T.; Kamperman, M.; Joo, Y. L. *Macromolecules* **2006**, 39, 5453.

[21] Kalra, V.; Mendez, S.; Lee, J. H.; Nguyen, H.; Marquez, M.; Joo, Y. L. *Adv. Mater.* **2006**, 18, 3299.

[22] McCann, J. T.; Marquez, M; Xia, Y. *J. Am. Chem. Soc.* **2007**, 128, 1436.

[23] Xiang, H.; Shin, K.; Kim, T.; Moon, S. I.; McCarthy, T. J.; Russell, T. P. *Macromolecules* **2004**, 37, 5660.

[24] Shin, K.; Xiang, H.; Moon, S.I.; Kim, T.; McCarthy, T.J.; Russel, T.P. *Science* **2004**, 306, 76.

[25] Ma, M.; Krikorian, V.; Yu, J. H.; Thomas, E. L.; Rutledge, G. C. *Nano letters* **2006**, 6, 2969.

[26] Li, W.; Wickham, R.A.; Garbary, R.A. *Macromolecules* **2006**, 39, 806.

[27] Wu, Y.; Cheng, G.; Katsov, K.; Sides, S.W.; Wang, J.; Tang, J.; Fredrickson, G.H.; Moskovits, M.; Stucky, G.D. *Nature Materials* **2004**, 3, 816.

[28] Kalra, V.; Lee, J.; Lee, J.H.; Lee, S.G.; Marquez, M.; Wiesner, U.; Joo, Y.L. *Small* **2008**, 4, 2067.

[29] Park, M. J.; Char, K. *Langmuir* **2006**, 22, 1375.

[30] Sides, S. W.; Bumjoon, J. K.; Kramer, E. J.; Fredrickson, G. H. *Phys. Rev. Lett.* **2006**, 96, 250601.

[31] Schultz, A. J.; Hall, C. K.; Genzer, J. *Macromolecules* **2005**, 38, 3007.

[32] Kalra V.; Joo, Y.L. *Proceedings of AIP Conferences* **2008**, 534, 1027.

[33] Zhao, Y.; Cao, X.; Jiang, L. *J. Am. Chem. Soc.* **2007**, 129, 764.

[34] Kalra. V.; Mendez, S.; Escobedo, F.; Joo, Y.L. *J. Chem. Phys.* **2008**, 128, 164909.

[35] Kremer, K.; Grest, G.S. *J. Chem. Phys.* **1990**, 92, 5057.

CHAPTER 6

COARSE-GRAINED MOLECULAR DYNAMICS SIMULATION ON THE PLACEMENT OF NANOPARTICLES WITHIN SYMMETRIC DIBLOCK COPOLYMERS UNDER SHEAR FLOW

6.1 Abstract

We present molecular dynamics simulations coupled with a dissipative particle dynamics thermostat to model and simulate the behavior of symmetric diblock copolymer/nanoparticle systems under simple shear flow. We consider two categories of nanoparticles, one with selective interactions towards one of the blocks of a model diblock copolymer and the other with non selective interactions with both blocks. For the selective nanoparticles, we consider additional variants by changing the particle diameter and the particle-polymer interaction potential. The aim of our present study is to understand how the nanoparticles disperse in a block copolymer system under shear flow and how the presence of nanoparticles affects the rheology, structure and flow behavior of block copolymer systems. We keep the volume fraction of nanoparticles low (0.1) to preserve lamellar morphology in the nanocomposite. Our results show that shear can have a pronounced effect on the location of nanoparticles in block copolymers and can therefore be used as another parameter to control nanocomposite self assembly. In addition, we investigate the effect of nanoparticles on shear induced lamellar transition from parallel to perpendicular orientation to further elucidate nanocomposite behavior under shear, which is an important tool to induce long range order in self assembling materials like block copolymers.

6.2 Introduction

With modern synthetic techniques, the magnetic, electrical or optical properties of inorganic nanoparticles (NPs) can be tailored for a wide range of applications. Often significant effort must be made to avoid NP aggregation and thereby ensure a homogeneous distribution of NPs in a polymeric material. However, the effectiveness of these NPs can be enhanced if they are arranged periodically in three dimensions. One can combine the functionality of NPs with the phenomena of block copolymer self-assembly to achieve hierarchical spatial distributions of NPs. Having the NPs periodically spaced can lead to synergistic effects of optical [1] and mechanical properties [2, 3], for example, and can potentially be used in novel applications such as magnetic storage media and catalysis [4, 5, 6].

Recently there has been a flurry of reports that explore how various system parameters affect the equilibrium location of NPs within block copolymers (BCPs). Such systems have been studied with experiments, theory and computer simulations. In these studies, researchers varied parameters such as the interaction between the NP and the "A" or "B" monomer of an "AB" diblock copolymer or the size of the NPs (relative to the BCP end to end distance, R_0). In computer simulations or theory, the interaction between NP and monomers is relatively straightforward to define (e.g. pair-wise Lennard-Jones interactions). Experimentally, a panoply of procedures is available to chemically modify the surface of the NPs. In one possible scenario, short ligands, which are composed of the same monomer as one of the blocks of a copolymer, can be chemically tethered to the NP surface. In this case, the surface modified NP (at low volume fraction) would be completely miscible within one of the phases. In describing

a polymer solution, a solvent with these properties would be deemed as "selective". Another possible case would be to coat the NP surface with ligands that are made up of monomers that have the same composition as both blocks of the copolymer. This type of surface treatment would render the NPs miscible in either copolymer phase. From polymer solution terminology, the analogous label for this condition would be "nonselective".

As expected, the equilibrium location of the NPs within a block copolymer melt is dictated by thermodynamics, namely, by the balance between enthalpy and entropy. There are enthalpic interactions between the chemically altered NP and the copolymer blocks. The entropic contribution has two prominent components: the translational entropy of the NPs and the configurational entropy of the polymer chains. Chiu *et al* demonstrated that the NP surface chemistry could be used to direct the placement of NP within diblock copolymers [7]. The selective NPs gathered at the center of one domain, while the population of the non-selective NPs centered around the *AB* interface. These two cases were also studied with computer simulations by Schultz *et al*, and their results agree qualitatively with the experiments [8].

To study the effect of NP size on their equilibrium location, a mean field theory was used by Thompson *et al* [9]. They chose model systems where there is a selective interaction between the NP and one of the blocks. They found that for the case where the *A*-coated NP is small, the NPs are exclusively located throughout the *A* domain. For the other extreme of large NP, they tend to be located at the AB domain interface in spite of the loss of translational entropy. This loss is offset because if the large NP were throughout the *A* domain, then the *A* polymer segments would have to stretch around the NP thereby resulting

in loss in polymer configurational entropy. These theoretical predictions were affirmed by experimental observations [1] as well as the computer simulations of Schultz *et al* [8]. To summarize, the equilibrium location of NPs within BCPs can be controlled by the type of interaction between the NP and the copolymer blocks or by the size of the NP relative to the R_g of theBCP.

Besides investigating the spatial arrangement of NPs, there is interest in determining how the addition of NPs affects the formation of self-assembled structures or the phase diagram of block copolymers. The thermodynamics of BCP/NP mixtures was first studied with theory and simulation by Huh and coworkers [10]. Using a theory based on the strong segregation limit as well as lattice Monte Carlo simulations, they generated plots of the volume fraction of minority component of the BCP versus volume fraction of NPs at a fixed high value of χN and for various NP sizes. Here the NPs were selective towards monomers of one of the blocks. For these mixtures, it was found that the addition of NPs induced phase transitions between the thermodynamically stable self-assembled structures such as spheres, cylinders and lamellae. Schultz *et al* performed molecular dynamics simulations of symmetric block copolymers over a series of χN and volume fractions (ϕ_p) of NPs to map out a phase diagram [8]. They modeled NPs of various sizes with selective and nonselective interactions. The nonselective NPs had no dramatic effect on the self-assembled lamellae except that their presence shifted the χN ODT to higher values; moreover, for a given χN, above a certain ϕ_p, the structure transitioned from ordered to disordered. Addition of selective NPs to a symmetric BCP melt resulted in an interesting phase diagram: for a given χN at low ϕ_p, there were lamellae, then with increasing ϕ_p perforated lamellae, cylinders, and then an order-disorder transition in agreement with the earlier simulation results of Huh *et al* [10]. Hence, we

expect that keeping the volume fraction of NP low within the symmetric BCP matrix leads to the formation of lamellae when the χN value is sufficiently high.

BCPs can be subjected to external fields, such as electric fields or shear flow, to induce structural changes. Both of these fields have been demonstrated to produce favorable effects which include inducement of long-range order and order-disorder or order-order structural transitions, as well as the orientation of self-assembled structures. As documented in a review by Hamley [11], the effects of shear flow on self-assembled spheres, cylinders and lamellae have been well studied. In a more focused review, Wiesner surveyed the current progress in understanding how shear flow affects the lamellae formed by symmetric diblock copolymers [12]. When symmetric BCPs are annealed at high temperature, lamellae form but usually there is only local ordering and grain boundaries pervade throughout the bulk sample. Shear can help to remove these grain boundaries thus resulting in the formation of large lamellae. For BCPs that are at temperatures (or χN values) slightly above the order-disorder transition, shear can induce the formation of lamellae. The shear is thought to suppress concentration fluctuations and therefore stabilize the lamellae. Three lamella orientations have been observed: at low shear rates the lamellae are parallel to the flow direction and at higher shear rates the lamellae are perpendicular to the flow direction (with the lamellae normal pointing in the neutral direction); the more elusive orientation is called transverse where the lamellae normal is parallel to the flow direction. These transitions have been shown to depend on the shear rate (or frequency with oscillatory shear). Fraser *et al* used molecular dynamics simulations to model the shear-induced transition of lamellae in the parallel and perpendicular orientations [13, 14]. Based on our literature survey, only a handful of publications have directly addressed the dy-

namic behavior of BCP/NP mixtures. A relevant work was reported by Pozzo *et al* where they dispersed silica nanoparticles into Pluronic triblock copolymer systems that exhibited a micellar cubic morphology [15]. The thrust of their work was to test how the temperature profile during sample preparation or particle size and concentration affected their equilibrium placement within cubic matrix. Rheological measurements were performed to probe the structure that resulted from varying the aforementioned parameters. They did not utilize shear flow to induce the formation of a self-assembled structure or to guide the placement of NPs within the matrix. Similar work was reported independently by Castelletto *et al*. [16] and by Lee *et al.* [17] for BCPs mixed with silicate or clay particles.

In the current work, we present results on the computational simulations we performed to model BCP/NP mixtures that are subjected to simple shear flow. From what has already been reported in the literature, we can anticipate the equilibrium location of the NPs that are mixed with symmetric BCPs. The NP placement, as was noted earlier, can depend on the interaction between the NP and either of the two immiscible monomers of the diblock copolymer, or on the NP size. We narrow our investigation to probe the effect that shear flow has on the NP placement. To this end, we define potentials such that the NP is either selective to one block or non-selective to either of the two blocks, and we increment the shear rate over a range of a few orders of magnitude. To further limit the scope of the analysis, we model the NPs as spheres that have the Lennard-Jones diameter =1-1.5 times the monomers size, and we keep the volume fraction of NP fixed to 0.1. From these simulations we aim to address four questions: 1) *How does shear flow affect the spatial distribution of NPs?;* 2) *How does the presence of NPs affect the shear-induced transition in lamellae orientation?;*

3) *How is the rheology of the BCPs affected by the inclusion of NPs?; and 4) How does the effect of shear vary for NPs with different diameter and interaction potential?* Our ultimate goal is to elucidate the conditions that are necessary to gain even greater control of the highly ordered placement of NPs.

In the following section we describe the manner in which we modeled the block copolymer and the nanoparticles. We show the pair-wise potentials for all species, and we provide details on the computational method employed. In the Results Section, we present simulation results on the different nanocomposite systems that we studied under shear flow. Finally, in the Discussion Section, we suggest mechanisms that could explain our findings.

6.3 Model and Methods

6.3.1 Potentials

The copolymer chains in the current study are modeled as fully flexible bead-spring chains where the monomers are never allowed to overlap. Since we are dealing with a diblock copolymer, the chains consist of "A" and "B" blocks of monomers. The excluded volume interactions between the A and B monomers are accounted for by the purely repulsive, cut and shifted, Lennard-Jones (LJ) potential which is often referred to as the WCA potential [18],

$$u^{REP}(r) = 4\varepsilon\left[\left(\frac{\sigma}{r}\right)^{12} - \left(\frac{\sigma}{r}\right)^{6}\right] + \varepsilon = u^{LJ}(r) + \varepsilon, \quad r \leq 2^{1/6} \tag{6.1}$$

$$u^{REP}(r) = 0, \quad r > 2^{1/6}$$

where r is the separation distance between beads, and σ are ε are the Lennard Jones parameters, taken to be unity for the sake of simplicity. Within a polymer, the neighboring monomers are connected by a FENE (Finitely Extensible Nonlinear Elastic) potential [19],

$$u^{FENE}(r) = -\frac{1}{2}kR_{\max}^2 \ln\left[1 - \left(\frac{r}{R_{\max}}\right)^2\right] \tag{6.2}$$

where we set the spring constant, k, to 30, and the maximum extensibility, R_{max} , to 1.5 as described by Kremer and Grest [19].

To incorporate the physics of microscopic phase separation between the A and B species, we utilize an attractive potential between like monomers (i.e., $A-A$ or $B-B$). This interaction taken together with the repulsive $A-B$ potential ensures that phase separation will occur if the temperature is below the order-disorder transition temperature. We use the same attractive potential that was used by Horsch and coworkers [20] to model the equilibrium properties of diblock copolymer melts. This is again a LJ potential but now it is cut and shifted at values that differ from those presented in Eq. (6.1),

$$u^{ATT}(r) = 4\varepsilon\left[\left(\frac{\sigma}{r}\right)^{12} - \left(\frac{\sigma}{r}\right)^{6}\right] + u^{LJ}(2.5), \quad r \leq 2.5 \tag{6.3}$$

$$u^{ATT}(r) = 0, \quad r > 2.5$$

The higher cut-off means that this is not purely repulsive and that monomers of the same type are attracted to each other. With this potential, Horsch *et al* generated various points in the phase diagram, and found good agreement with the phase diagram from mean field theory. These authors derived the Flory-Huggins χ parameter between the A and B sites as a function of the simulation temperature [20]. In the present work, we performed all simulations at a temperature that results in χNgalue (~50) well above the order disorder transition.

For the nanoparticles, we model two different types of particles, namely selective and non selective. For selective particles, we use a purely repulsive potential between monomer "B" and particle "P" and for the interaction between monomer "A" and P, we consider two different cases of potential that are both attractive with k=1.0 and k=0.9 in the equation below. P-P potential is kept same in all systems =u^{ATT}.

$$\begin{aligned} u^{ATT}_{A-P}[k] \quad &= 4\varepsilon\left[\left(\frac{\sigma}{r}\right)^{12} - \left(\frac{\sigma}{r}\right)^{6}\right] + ecut, \;\; r \leq 2^{1/6} \\ = k * \{4\varepsilon&\left[\left(\frac{\sigma}{r}\right)^{12} - \left(\frac{\sigma}{r}\right)^{6}\right] + u^{LJ}(2.5)\}, \;\; 2^{1/6} \leq r \leq 2.5 \\ &= 0, \quad r > 2.5 \end{aligned} \tag{6.4}$$

Where, *ecut* is the value by which $u^{ATT}_{A-P}[k]$ needs to be shifted to make the potential continuous at r= $2^{1/6}$.

$u^{ATT}_{A-P}[1.0]$ is essentially the same as u^{ATT} and $u^{ATT}_{A-P}[0.9]$ represents an A-P potential that is slightly less attractive than $u^{ATT}_{A-P}[1.0]$. Any value of k below 0.9 causes the nanoparticles to get aggregated due to strong P-P attraction compared to the A-P attraction. For non selective particles, we use u^{ATT} for both A-P and B-P contacts. Table 6.1 summarizes the interactions between different elements in various systems.

Our simulation model neglects the effect of nanoparticle rotational dynamics on the rheological behavior of our systems. Note that although such rotational effects are irrelevant for thermodynamic behavior, they are important for flow behavior. It is expected, however, that such effects will become more significant the higher the concentration of nanoparticles in the system and the higher the shear rate. We assume that the nanoparticle surface functionalization

Table 6.1: Summary of interactions between the nanoparticles (P) and the A and B monomers of the diblock copolymer.

Selective[1]	u^{ATT} or $u^{ATT}_{A-P}[1.0]$	*A-A, B-B, P-P, A-P*
	u^{REP}	$A-B, B-P$
Selective[0.9]	$u^{ATT}_{A-P}[0.9]$	$A-P$
	u^{ATT}	*A-A, B-B, P-P*
	u^{REP}	$A-B, B-P$
Non Selective	u^{ATT}	*A-A, B-B, P-P, A-P, B-P*
	u^{REP}	$A-B$

is such that rotation modes tend to be suppressed and that for the relatively low nanoparticle concentration used in this work (10 vol%), such rotational effects are small compared to that of the translational modes. This is clearly an approximation but is expected not to greatly affect the qualitative response of our systems under shear flow.

6.3.2 Thermostat

We used a thermostat that preserves hydrodynamic interactions, i.e., the Dissipative Particle Dynamics (DPD) thermostat. DPD is a simulation technique that was originally conceived to model the interaction of mesoscopic units. The interactions between sites are treated as "soft" potentials meaning that the mesoscopic units can overlap. It was demonstrated by Soddemann *et al.* [22] that this thermostat is effective when using "hard" LJ potentials as is being used in this work. In DPD we solve the equations of motion,

$$\frac{dr_i}{dt} = \frac{p_i}{m_i} \tag{6.5}$$

$$\frac{d\vec{p}_i}{dt} = \sum_{i \neq j} \vec{F}^C_{ij} + \sum_{i \neq j} \vec{F}^D_{ij} + \sum_{i \neq j} \vec{F}^R_{ij}$$

where, $\vec{F}^D$ is a dissipative (or damping) force and $\vec{F}^R$ is a random force. These two terms act as a heat source and drain thus regulating the simulation cell temperature. $\vec{F}^C$ is the conservative force that acts between two particles. The dissipative force can be expressed as

$$\vec{F}^D_{ij} = -\zeta\, \omega^D(r_{ij})(\vec{v}_{ij} \cdot \hat{r}_{ij})\hat{r}_{ij} \tag{6.6}$$

where ζ is a friction parameter and $\omega^D(r)$ is a weight function. The random force is

$$\vec{F}^R_{ij} = \sigma_N \omega^R(r_{ij})\xi_{ij}\hat{r}_{ij} \tag{6.7}$$

where σ_N is a noise parameter and ξ is a white noise variable. From the fluctuation-dissipation theorem we have

$$\sigma_N = (2k_B T\zeta)^{1/2} \tag{6.8}$$

$$\omega^D(r) = [\omega^R(r)]^2$$

As reported by Fraser *et al.* [14], we used weight functions that have the form,

$$\omega^D(r) = \omega^R(r) = \omega(r) \tag{6.9}$$

$$\omega(r) = \begin{cases} 1 & if \quad r < r_c \\ 0 & if \quad r \geq r_c \end{cases}$$

6.3.3 Simple Shear Flow

Shear flow can be used to control the structure made from self-assembled molecules. This external field can induce order-disorder transitions or long-range ordering in relatively short amounts of time. In our MD code, we implemented shear flow with the SLODD algorithm using the following equations of motion [23]:

$$\frac{d\vec{r}_i}{dt} = \frac{\vec{p}_i}{m_i} + \hat{i}\,\dot{\gamma} y_i \tag{6.10}$$

$$\frac{d\vec{p}_i}{dt} = \vec{F}_i - \hat{i}\,\dot{\gamma} p_{yi} \tag{6.11}$$

where, $\vec{p}_i$is the peculiar momentum of particle/bead i, and $\dot{\gamma}$ is the shear rate, and $\hat{i}$is the unit vector in x direction. By this method we can impose a linear velocity profile in the x direction with a constant gradient in the y direction (with z as the neutral direction). These equations of motion are implemented with compatible Lee-Edwards periodic boundary conditions [24], wherein two opposing periodic images are incrementally moved in opposite directions consistent with the applied shear rate. Plots of shear viscosity versus shear rate for polymeric fluids have been widely published in the literature [25], and they clearly demonstrate these fluids exhibit a Newtonian regime at low shear rates and shear thinning at higher shear rates. The pressure tensor can be calculated from simulations using [26],

$$P = \frac{1}{V}\left(\sum_{i}^{nM} \frac{p_i p_j}{m_i} + \sum_{j>i}^{nM} r_{ij} F_{ij}\right) \tag{6.12}$$

From this, we can determine the shear viscosity by the following relationship,

$$\eta = -\frac{P_{xy}}{\dot{\gamma}} \tag{6.13}$$

6.3.4 Computational Details

Throughout these simulations we fixed the polymer chain length to 10 monomers/beads. The particle volume fraction was fixed at 0.1 for both selective and non selective NPs to preserve lamellar morphology in the nanocomposite [8]. The site density, ρ, was kept fixed at 0.85 and the temperature, k_BT, was kept at 1.0. Although the copolymer chain length adopted here is relatively short, it is considered appropriate to capture the essential behavior of symmetric copolymers [13, 27], since 5 beads ($\sim$ 5 Kuhn lengths) is about the minimum chain length that a block can have to possess oligomeric character (the shortest block in a "non symmetric" copolymer should also be $\sim$5 beads long). To prevent undue periodic boundary artifacts, we varied the system size from L= 36 down to L= 26 till the system attained its natural lamellar spacing [28]. Figure 6.1 shows a typical box size study performed for selective NP/BCP system at $\dot{\gamma}$ = 0.005. Due to the limited number of repeat units, the system is very sensitive to slight changes in the lamellar spacing caused by addition of NPs or by application of shear, therefore similar box size studies were conducted for various systems and shear rates. From our box size study, we do not find any effect of shear on the domain spacing in a particular system in the range of shear rates studied. The velocity verlet algorithm was used to integrate the equations of motion with a time step=0.01. To make the code efficient, we used a cell list algorithm [26]. The simulations were run for a sufficiently long time until variables such as pressure, potential energy, radius of gyration and mean squared end to end distance remained constant. In addition, we monitored the equilibration of order parameter O (see figure 6.2 for some test cases), which is the largest eigenvalue of the Saupe tensor, with time till it stabilized to an equilib-

rium value [29].

$$Q_{\alpha\beta} = \frac{3}{2N_P} \sum_{i=1}^{N_P} e_{i,\alpha} e_{i,\beta} - \frac{1}{2}\delta_{\alpha\beta} \tag{6.14}$$

where e_i is the unit vector along the end to end direction of a diblock copolymer i and $\delta_{\alpha\beta}$is the Kronecker delta. O is zero in a completely disordered state and it is unity if the system is perfectly aligned.

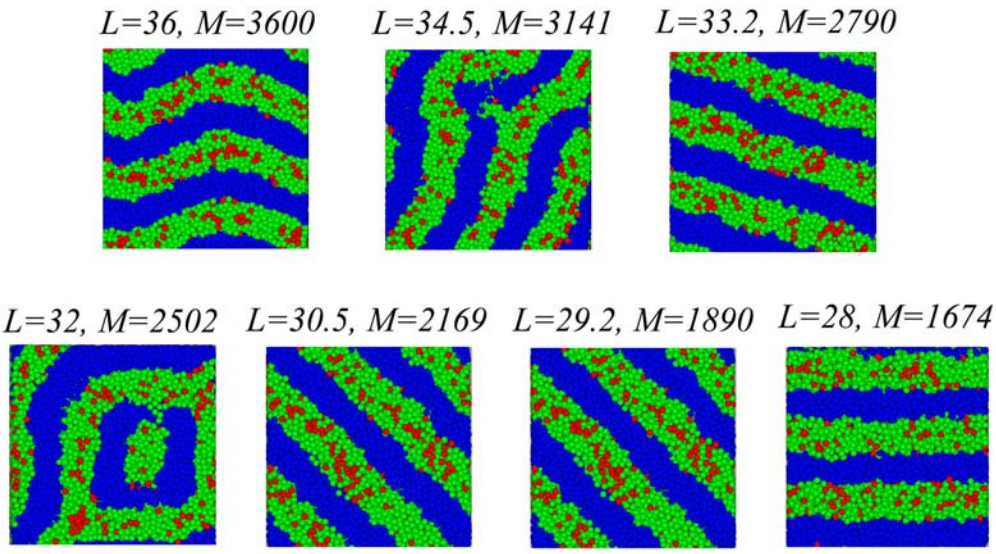

Figure 6.1: Box size study: Snapshots of Sel[1.0]-1.0 nanocomposite system started from disordered melts with different box sizes at $\dot{\gamma}$ = 0.005. L = length of cubic box, M = number of diblock copolymer chains with 5 A beads and 5 B beads, density is fixed at 0.85 and all systems have 10% selective particles. Similar studies were done for all systems at various shear rates.

We note that the NP size used for most part of the current work is same as the size of the Kuhn monomer and one could then consider such NPs to actually represent a solvent or small oligomer. However, the "NP size/polymer end to end distance" ratio corresponding to such small NPs has been found in practice in several instances [30, 31]. From our preliminary results, we find that the end to end distance of a copolymer chain in the pure block copolymer system used

in this work is R_0=4.62, corresponding to σ_P/R_0 = 0.216, where σ_P(NP size)=1. Moreover, using the entanglement length as reference, a bead-spring polymer chain with 10 beads would typically represent a molecular weight of ~6K [19] for a material like polystyrene, which corresponds to a domain spacing of ~9 nm for a symmetric diblock copolymer or an end to end distance of ~4.5 nm. This comparison leads a nanoparticle size of ~ 1nm in our simulations, which although on the borderline, does fall in the nanometer regime. To further ensure that our results are not peculiar to the particle size of one Kuhn monomer, we additionally studied selective-particle systems using NP diameter =1.2 and 1.5. The volume fraction of the NPs is kept fixed at 0.1 for all systems. Table 6.2 summarizes some of the parameters used in this work. Table 6.3 summarizes the different NP/BCP systems used in this work, specifying the potential and particle diameter.

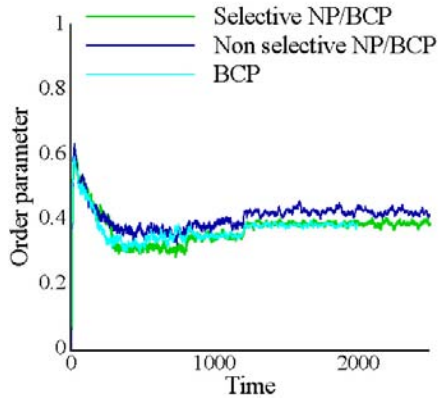

Figure 6.2: Orientation order parameter O as a function of time at $\dot{\gamma} = 0.125$ for Sel[1.0]-1.0, NonSel-1.0 and pure BCP systems.

[1]The values in MD units are understood to be multiplied by the appropriate combinations of three independent fundamental units of length, mass and energy [26].

Table 6.2: Simulation parameters.

Parameters	**Symbol**	**Value (MD units)**[1]
Temperature	k_BT	1
monomer size	gσ	1
NP diameter	σ_P	1-1.5
NP,monomer mass	m	1
Chain length	N	10
Bead density	ρ	0.85
Cubic box size	L	26-36
NP fraction	ϕ_P	0.1
Number of chains	M	1341-3600
Flory Huggins parameter*N [20]	χN	53.3
MD integration time step	Δt	0.01
Domain spacing	d	~ 9.1
Copolymer end to end distance	R_0	4.62
Shear rate	$\dot{\gamma}$	0-0.15

Table 6.3: Summary of all different types of nanoparticles used in this work

Type	**Name**	**Potential**	σ_P
Selective	Sel[1.0]-1.0	Selective[1]	1.0
	Sel[0.9]-1.0	Selective[0.9]	1.0
	Sel[1.0]-1.2	Selective[1]	1.2
	Sel[1.0]-1.5	Selective[1]	1.5
Non Selective	NonSel-1.0	Non Selective	1.0

6.4 Results

6.4.1 Spatial Distribution of Selective Particles within Diblock Copolymers

In Figure 6.3, we present results for the system that has a model block copolymer mixed with "Sel[1.0]-1.0" particles. For the volume fraction of selective particles used in this study, we expect the formation of lamellae [8]. Because there are attractions between the particles and the monomers of one of the blocks, we expect, at least under quiescent conditions (i.e. no shear flow), that the particles will segregate exclusively into one of the domains. As evident in Figure 6.3a ($\dot{\gamma}$ = 0.1), there is a negligible amount of particles in the domain where the particles do not have attractions. The information contained in the simulation cell snapshots can be made quantitative by calculating the concentration of each species as a function of distance across the simulation box (figure 6.3b). Both experimental and simulation studies with similar ratio of NP/polymer end to end distance (σ_P/R_0 = 0.216) have been conducted previously for quiescent systems [8, 30, 31] and it has been shown to lie in a regime where the decrease in conformational entropy of the polymer chain upon particle sequestration can be significant and therefore the nanoparticles prefer to stay close to the chain ends, i.e., the center of the preferred domain. Our results are qualitatively similar to previous results for $\dot{\gamma}$=0 [8, 30, 31]. In addition, we find that at all shear rates, the NP concentration profiles exhibit a maxima at the center of the preferred domain (figure 6.3b). In Figure 6.3c we present the particle concentration profiles that were obtained over a range of shear rates that covers three orders of magnitude. We find that the peaks become sharper with increasing shear rate

and despite the significant level of shear being imposed on the system, the particles do not mix into the domain where the interactions are not favorable. This could be attributed to the shear induced suppression of fluctuations [12] in the system morphology stabilizing the chain end density at the domain center and hence causing an increase in the NP concentration at the center of the preferred domain. These simulation results suggest that the entropic contributions play a significant role and indicate that shear flow can be used to further control the location of selective particles. To further elucidate our findings and understand the effect of A-P interaction and particle diameter, we studied concentration profiles as a function of shear rate for "Sel[0.9]-1.0" and "Sel[1.0]-1.5" and we found a similar sharpening of peak with increasing shear rate (figure 6.4). As expected, the volume fraction peak sharpens with increasing particle diameter (for a given shear rate) due to an increase in entropic penalty of chain stretching (around particles) for larger particles (figure 6.4c).

6.4.2 Spatial Distribution of Non-selective Particles within Diblock Copolymers

In Figure 6.5a we present a snapshot of the structure we obtained from our simulations of Non Selective NP/BCP system ("NonSel-1.0") at $\dot{\gamma} = 0.1$. This image indicates that the NPs are preferentially located at the interface between A and B domains. In Figure 6.5b we see distinct peaks in the concentration profiles which mean that the NPs are centered between the minima of the A and B monomer concentration profiles. As noted in Table 6.3, the non-selective particles are equally attracted to the monomers of both copolymer blocks, therefore,

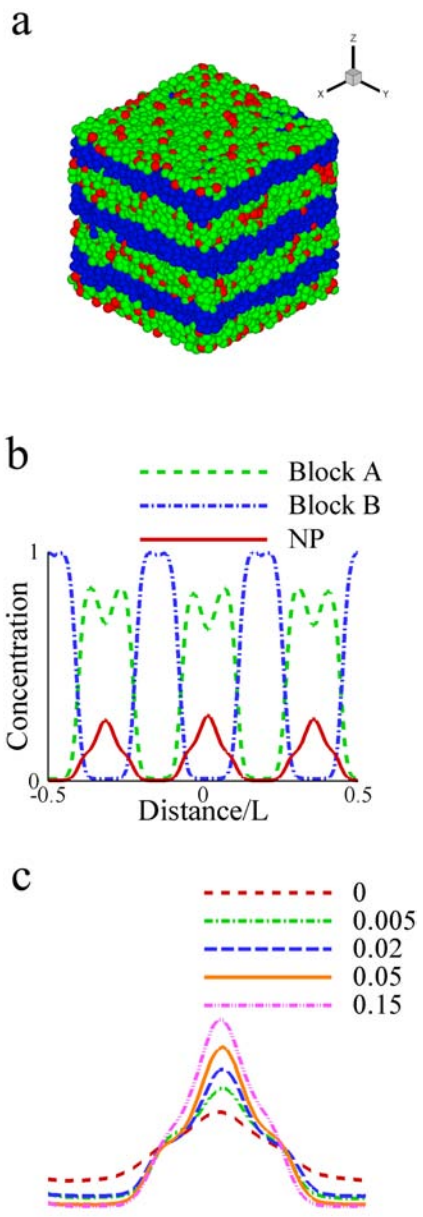

Figure 6.3: Symmetric diblock copolymers mixed with selective nanoparticles (Sel[1.0]-1.0). (a) Snapshot from a MD simulation with $\dot{\gamma}$ = 0.1. The block that is attracted to the nanoparticles is shown in blue, the other block is shown in green and the nanoparticles are shown in red. Concentration profiles of (b) the two copolymer blocks along with the profile of the selective particles where $\dot{\gamma}$ = 0.1. (c) Concentration profiles of the particles at various shear rates as shown in the legend. The peaks become sharper with increasing shear rate. L=box length.

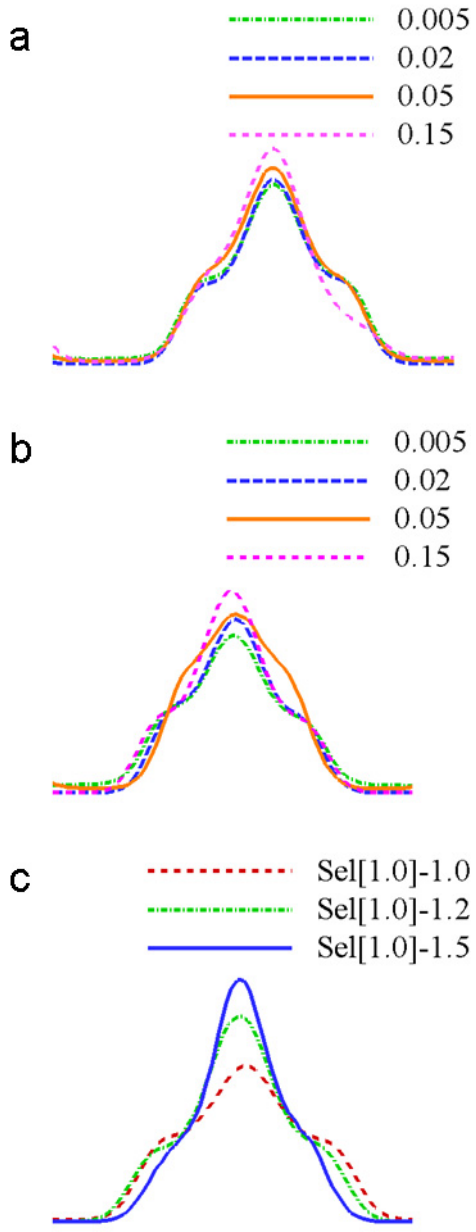

Figure 6.4: a, b) NP Concentration profiles at different shear rates for a) Sel[0.9]-1.0 and b) Sel[1.0]-1.5, and c) NP concentration profiles of different particle diameters for selective particle systems at $\dot{\gamma}$=0.01.

we expect that the particles show no enthalpic preference for either domain. The main driving force causing the particles to position at the *AB* interface is the reduction in interfacial tension arising from decrease in *AB* contacts [8, 32]. However, the particles are not zero in A and B domains due to the favorable interactions between NPs and *A* (and *B*) domains. Our results qualitatively agree with the findings of Schultz *et al* who studied similar systems under no flow conditions. In Figure 6.5c are concentration profiles for the particles taken over a range of shear rates. For the various flow rates, we observe that the non-selective particles remain segregated predominantly at the domain interface. Unlike the case of selective particles, the non selective NPs at the interface experience two competing forces; the first one trying to locate the NPs at the A-B interface to reduce the tension between strongly segregated (χN =53.3) blocks, the second force trying to push the particles towards the chain ends away from the interface to avoid the penalty of chain stretching. Therefore, shear effect is much more constrained, causing only small fluctuations in the NP concentration profile and no significant effect with increasing shear rate. This effect of shear, we believe would be dependent on both the NP size and the block copolymer segregation strength. These results indicate that the particle positions can be preserved while shear is applied to induce long range order in block copolymer nanocomposites.

6.4.3 Shear-induced Transitions in Lamellae Orientation

As noted in the introduction, shear flow can be used to control the lamellar orientation of symmetric diblock copolymers [12]. Moreover, the transitions between the various lamellar orientations can depend on the imposed shear rate.

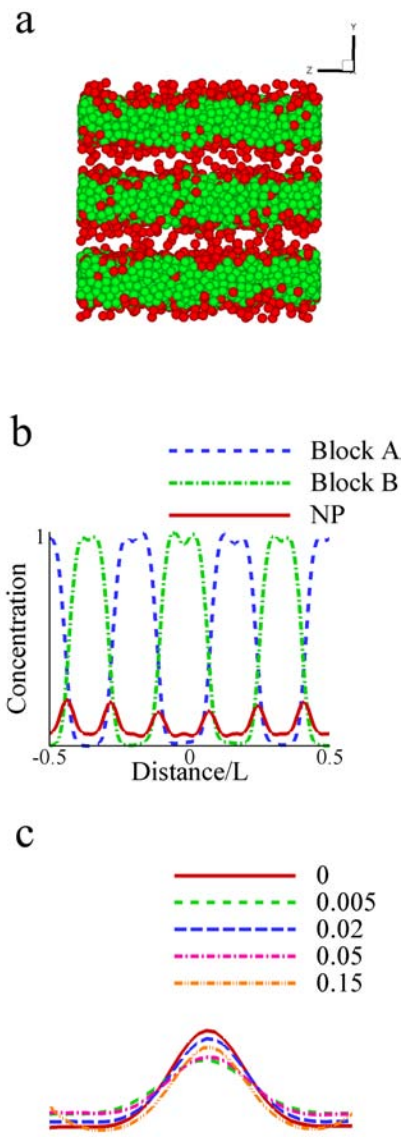

Figure 6.5: Symmetric diblock copolymers mixed with non-selective nanoparticles (NonSel-1.0). (a) Snapshot from a MD simulation with $\dot{\gamma} = 0.1$. One of the blocks is not shown for the sake of clarity, and the nanoparticles are shown in red. Concentration profiles of (b) the two copolymer blocks along with the profile of the non-selective particles where $\dot{\gamma} = 0.1$. In this case, the particles are equally attracted to both monomers. (c) Concentration profiles of the particles at various shear rates as shown in the legend. Shear has no significant effect on non selective nanoparticle concentration profiles. L= box length.

At low shear rates, the lamellae tend to align in a parallel configuration while at higher shear rates there can be a transition to the perpendicular alignment. Using a computational method very similar to the one used in this work, Fraser *et al* studied how simple shear flow affected the orientation of lamellar structures [14]. Starting with lamellae in both orientations, they plotted the potential energy as a function of shear rate. They found that shearing the lamellae that was initially perpendicular always resulted in lower potential energy and that the lamellae that was initially parallel converted to the perpendicular arrangement at higher shear rates. In this work, we sheared disordered systems which eventually evolved to either parallel or perpendicular lamellae. In Figure 6.6a and 6.6b, we show snapshots of the parallel configurations obtained for pure BCP systems at $\dot{\gamma} = 0$ and 0.001 respectively. In figure 6.6c, we show the perpendicular lamellar obtained at the critical shear rate ($\dot{\gamma} = 0.005$) where the transition from parallel to perpendicular lamellar takes place. Previous studies on the flip of lamellar orientation have reported a decrease in lamellar spacing in perpendicular orientation at shear rates much higher than the critical shear rate [38]. Both literature and our box size study confirm that there is no effect of shear on domain spacing around the critical shear rate value. Therefore, we do not expect the flip of orientation seen in this work to be a manifestation of stresses that could arise due to a box size that is incommensurate with the lamellar spacing.

Rheological measurements can be performed to resolve the structure of a self-assembled copolymer system. A sharp decrease in shear viscosity is seen at the critical shear rate where a transition from parallel to perpendicular takes place [33, 34]. In Figure 6.7, we present a log-log plot of the shear viscosity that was calculated with equations 6.12 and 6.13 as a function of shear rate for 4 systems from Table 6.3 and a pure block copolymer system. For pure block

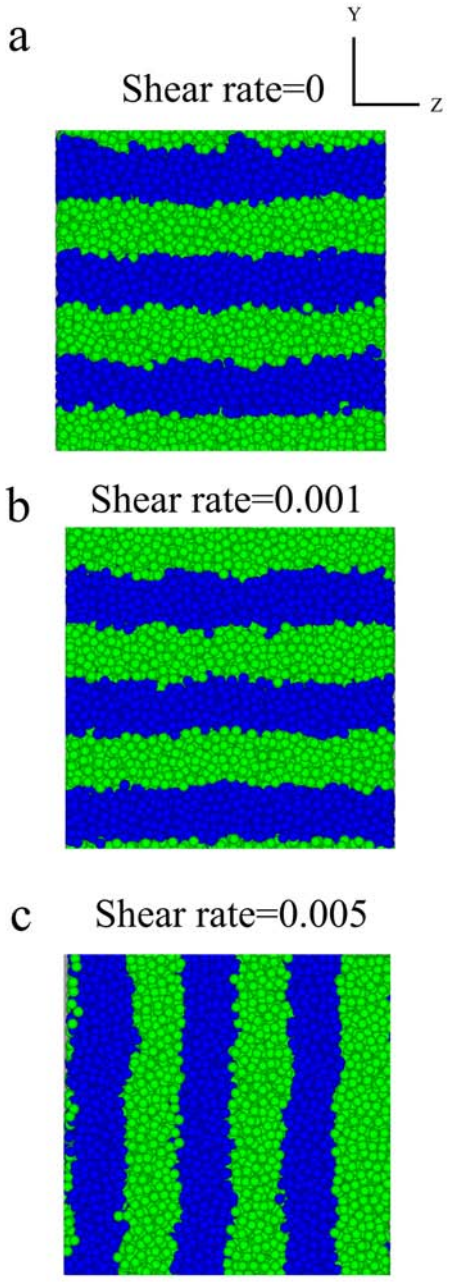

Figure 6.6: Snapshots of symmetric diblock copolymers at $\dot{\gamma}$= (a) 0, (b) 0.001 (parallel) and (c) critical shear rate $\dot{\gamma}$ = 0.005 (perpendicular) where orientation flip takes place.

copolymer system, the shear viscosity sharply drops at a shear rate of 0.005 indicating an orientation flip to perpendicular morphology, also seen from the snapshots in figure 6.6. Similar plots for nanocomposite systems show a shift

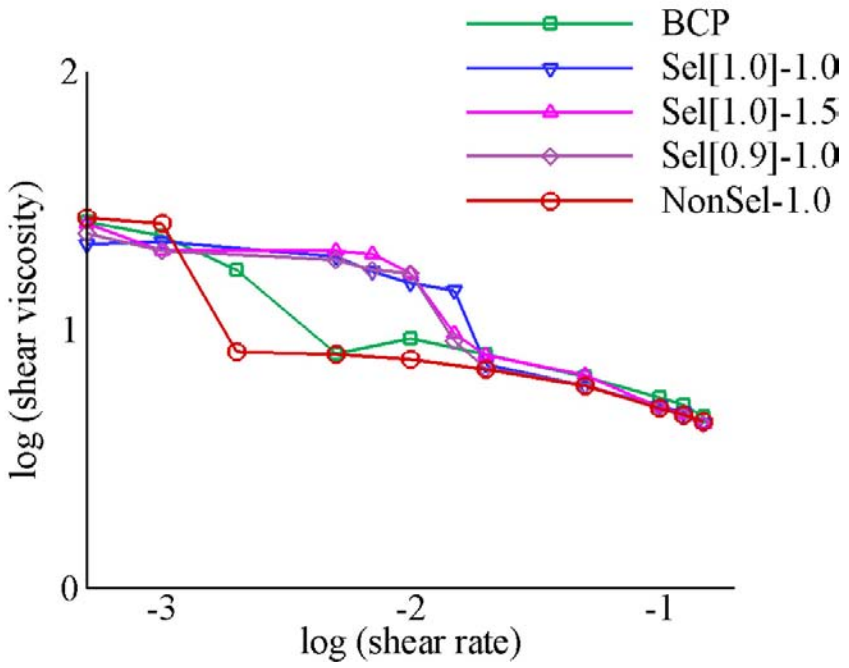

Figure 6.7: Log-log plots of the calculated shear viscosity versus imposed shear rate for pure copolymer, copolymer with selective and non-selective nanoparticles

of critical shear rate to a higher value (0.02) for selective NP/BCP ("Sel[1.0]-1.0") and a lower value (0.002) for non selective NP/BCP ("NonSel-1.0") as compared to a neat block copolymer. To further understand the effect of particle-polymer potential and particle diameter on the critical shear rate, we plotted the viscosity curves for "Sel[0.9]-1.0" and "Sel[1.0]-1.5" selective NP systems. For both cases, we find that the critical shear rate is higher compared to a pure block copolymer system, consistent with our earlier finding. However, the critical shear rate is lower for both a larger particle size and less attractive particle-polymer potential (=0.015) within selective particle systems. For the "Sel[1.0]-1.2 particles (not

shown in the figure), we find a similar viscosity curve as "Sel[1.0]-1.0" with critical shear rate =0.02. Figure 6.8a shows the root mean squared end to end distance in x direction for one selective, non selective and pure BCP system, and we find a sharp increase in $(< R_y^2 >)^{1/2}$ at the critical shear rates. $(< R_x^2 >)^{1/2}$ grows steadily with increasing shear rate, showing an orientation of chains along the flow direction. Finally, figure 6.9 shows the snapshots of two nanocomposite systems ("Sel[1.0]-1.0", "NonSel-1.0") for $\dot{\gamma}$ = 0, 0.001 and at respective critical shear rates for the two systems (=0.02 for Sel[1.0]-1.0 and 0.002 for NonSel-1.0) confirming the results obtained from Figures 6.7 and 6.8. Guo studied the effect of segregation strength between the two blocks in a diblock copolymer on the critical shear rate for symmetric diblock copolymers [33, 35]. He found that the critical shear rate decreases as the segregation between two blocks decreases. A similar analogy can be drawn for our system as the addition of nanoparticles is seen to affect the segregation between repelling blocks. We discuss this aspect in more detail in the following section. We note that shear viscosity plots for all systems collapse on the same curve for high shear rates similar to the findings of Kroger *et al* for polymers of different chain length [25].

6.5 Discussion

In the first part of our results section, we considered the effect of shear on two qualitatively different kinds of particles in a symmetric diblock copolymer melt system, namely, selective and non selective NPs. For the case of selective particles, we studied 4 systems to examine the effect of different particle-polymer potential and NP size. For all selective particles, we find that the NP concentration profile exhibits a maxima at the center of the preferred domain A where

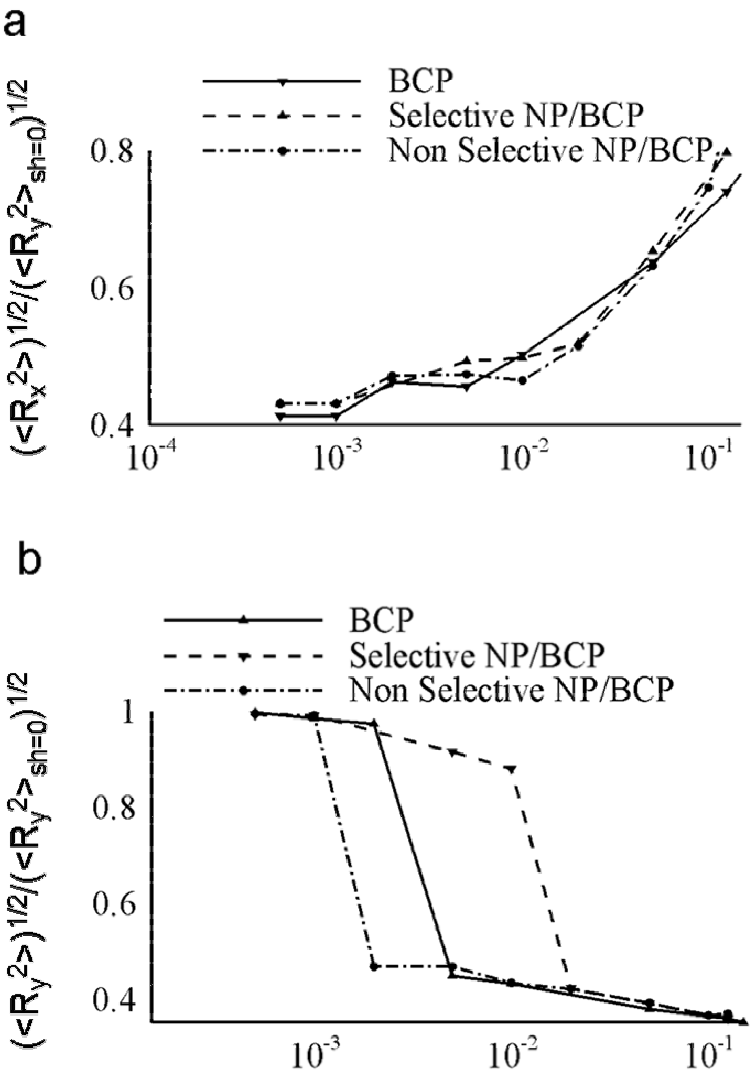

Figure 6.8: Normalized root mean squared end to end distances of polymer chains for Sel[1.0]-1.0, NonSel-1.0 and pure BCp systems in (a) *x*, and (b) *y* directions. Y axis is normalized using end to end distance in y direction at shear rate=0.

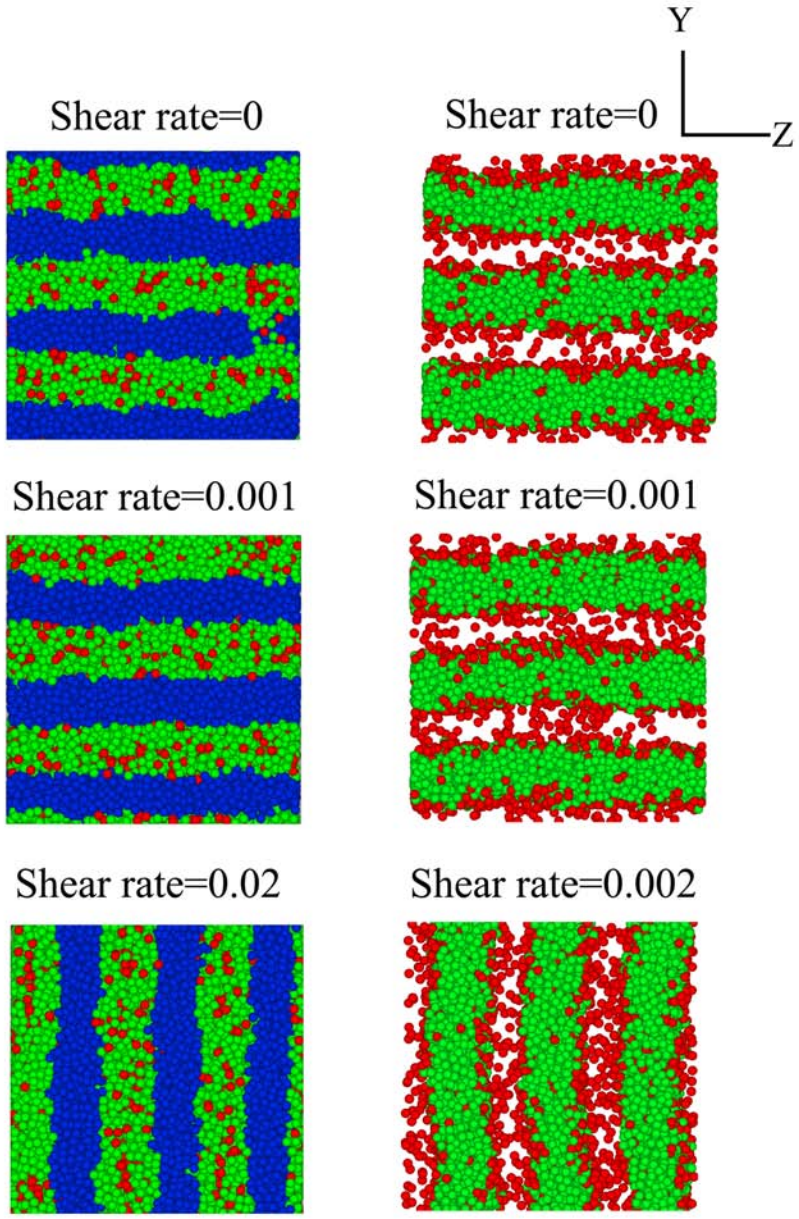

Figure 6.9: Snapshots of nanocomposites with (left) Sel[1.0]-1.0 NPs at $\dot{\gamma}$ = 0, 0.001 (parallel) and critical shear rate $\dot{\gamma}$ = 0.02 (perpendicular) and (right) NonSel-1.0 NPs at $\dot{\gamma}$ = 0, 0.001(parallel) and critical shear rate, $\dot{\gamma}$ = 0.002 (perpendicular). Perpendicular morphologies are shown at respective critical shear rates where a transition from parallel to perpendicular lamellar takes place. For Non selective particle system, one of the blocks is not shown for the sake of clarity and particles are shown in red.

most chain ends lie. This finding is in agreement with literature results (for quiescent systems i.e $\dot{\gamma}$=0) for the NP size to polymer ratios considered in this work [8, 30, 31]. Here, the entropic contribution plays a dominant role and pushes the NPs close to the chain ends, since the energetics remain the same for NPs throughout the A domain. A sharpening of these peaks is seen with the application of shear. We suggested that this finding can be attributed to the shear induced suppression of fluctuations causing the particle layer to get more defined at the domain center. To further support this argument, we plotted the concentration profiles of the "A chain end" both for a pure block copolymer system and Sel[1.0]-1.0 nanocomposite and we found a similar trend as the NP profile (figure 6.10). From these curves, it is clear that shear tends to reduce conformational fluctuations and localizes the A-block chain ends at the A-A interface (i.e. the middle of the A domain) This effect of shear is justified for it facilitates the A domains to slide past one another during shear flow. For the non selective particles, however, there is a competition between energetic and entropic contributions. The former tries to place the particles at the interface between strongly segregated blocks to reduce A-B contacts and interfacial tension, while the latter tries to push the particles away from the interface towards the chain ends to avoid the penalty of chain stretching. The localization of particles at the A-B interface (as seen in the figure 6.5b) is a consequence of greater energetic effect than entropic contribution. However, unlike the case for selective NPs, the dominant force (energetic for non selective particles) faces a competition and hence its effect is much more restricted. So even though, we expect similar fluctuation suppression for the case of non selective particles, the effect of shear is much more constrained and therefore, no clear shear dependence is seen. Please note that in the arguments considered above for both kinds of par-

ticles, we neglect the effect of translational entropy of the nanoparticles, as we believe that in both cases, it tries to disperse the particles away from the peak and hence does not provide a basis for comparison.

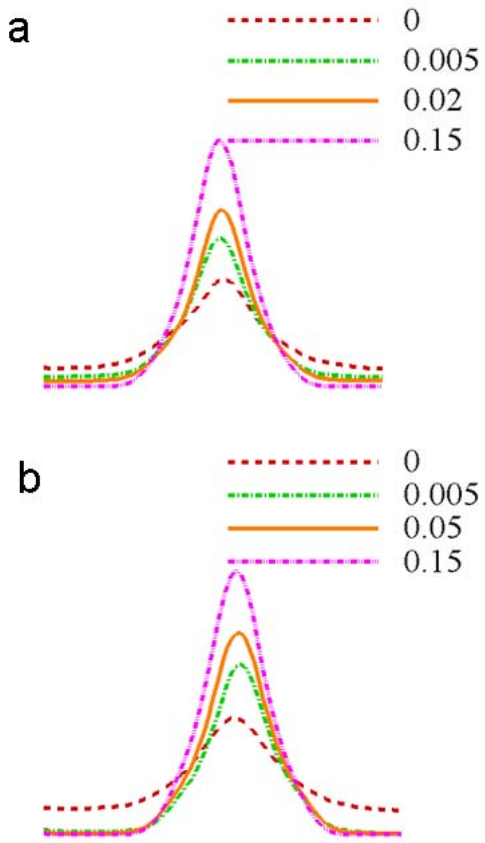

Figure 6.10: Concentration profiles of the A-block chain end for different shear rates for a) pure BCP and b) Sel[1.0]-1.0 nanocomposite system of selective NPs.

In the second part of the results section, we study how the presence of particles affects the shear rheology of such block copolymer systems; in particular, the shear induced transition from parallel to perpendicular lamellar. For selective particles, we consistently find that the critical shear rate (at which the parallel lamellar switches to a perpendicular orientation) increases compared to

a pure block copolymer system. We suggest that the NPs help in bridging different A chains and strengthening the cohesive forces within block A, thereby increasing the $(\chi N)_{eff}$ between block A and B causing a rise in the critical shear rate, similar to the one found by Guo [33, 35]. Increase in A-B incompatibility can be viewed as an increase in the order-disorder transition temperature T_{ODT}, thereby resulting in a "colder" system (with a larger effective gap from the T_{ODT}) which makes the transition to perpendicular orientation more difficult. This effect of temperature on the critical shear rate has been often seen in experimental lamellar systems by Wiesner and coworkers [41, 42] and Kornfield and coworkers [43, 44, 45]. Previous studies on the rheology of polymer nanocomposites have suggested that due to the comparable sizes of polymers and interparticle distances, NPs act as nodes of association for the polymer resulting in the formation of transient networks and slower dynamics of polymer chains in the presence of particles [39, 40]. Such kinetic constraints join together with the effect on $(\chi N)_{eff}$ between A and B blocks mentioned above to delay the orientation switch to a higher shear rate for selective nanoparticles. Contribution of selective NPs on $(\chi N)_{eff}$ is also evident from the shear viscosity plots for two different particle-polymer potentials for selective particles (Sel[1.0]-1.0, Sel[0.9]-1.0). As the attractive potential between particle and polymer reduces, the bridging effect is weakened causing a slight decrease in critical shear rate. We note that the transition shear rate is still much larger than that for a pure block copolymer system. A similar decrease in critical shear rate is also seen for the case of larger sized particles. With a 1.5 times increase in particle diameter, the interfacial area between NPs and polymer chains is reduced by 33%. This leads to a smaller polymer-particle interface and a weakening of the effect of both transient network formation and rise in $(\chi N)_{eff}$, thereby decreasing the

critical shear rate compared to smaller particle diameter.

For the case of non selective particles, NPs prefer to place themselves close to the interface between opposing blocks to reduce the number of A-B contacts. They work to decrease the interfacial tension between A and B and effectively reduce the segregation strength between the two blocks. By a similar analysis as for selective particles, a decrease in $(\chi N)_{eff}$ leads to a decrease in the critical shear rate. However, unlike selective particles, the effect on $(\chi N)_{eff}$and the kinetic constraints posed due to the presence of non selective NPs work in opposite directions. The former would reduce the critical shear rate, while the latter would work to increase it by slowing the dynamics of the system. This could possibly explain the little effect seen on critical shear rate on addition of non selective particles compared to a neat BCP. Moreover, for the selective particles, since the particles only go into one domain and prefer to stay close to chain ends, their role as network nodes would be stronger and more concentrated.

To conclude our discussion, we would like to draw a comparison of our system with the vast literature available for block copolymer in solvent systems. This comparison is valid as our system consists of nanoparticles that are comparable in size to the Kuhn segment of our polymer chains. Hanley *et al*, found a significant increase in T_{ODT}on addition of a strong styrene-selective solvent in poly (styrene-*b*−isoprene) ($\chi_{AS} << \chi_{BS}$) due to an increase in the degree of segregation of an A-B diblock copolymer [36]. This is also analogous to an increase in segregation between A and B blocks found on addition of "A" homopolymer by Matsen [37]. Similarly, it was found that a neutral solvent dilutes the monomer-monomer contacts and reduce the effective segregation. This analogy further validates our findings and widens the scope of this work.

6.6 Summary and Conclusions

In this work we have performed molecular dynamics simulations to model the behavior of copolymer/nanoparticle systems subjected to simple shear flow. Specifically, we investigated symmetric diblock copolymers with nanoparticles that had either selective or nonselective interactions with the copolymer. For selective NPs, we studied additional cases with different particle diameter and particle-polymer interaction to clarify the mechanisms behind our findings. We kept the volume fraction of particles relatively low so that we could maintain lamellar structures for all systems. Our aims were to determine how the particles were dispersed within the self-assembled copolymer matrix while under flow. We also wanted to know how the presence of the particles affected the shear-induced transition of the lamellar orientation.

For all of the systems at equilibrium, we found qualitative agreement between our simulation results and the results reported in the literature. The selective nanoparticles exclusively gathered within the domain where there were attractive interactions between the NPs and monomers. The concentration profiles exhibited a maximum at the center of the domain and the concentration was zero in the other domain. We varied the shear rate and our simulation results show that the concentration peaks become sharper as the shear rate increases for all selective particle systems. We also studied non-selective NPs and we found that they segregate to the interface between the *AB* domains. For the range of shear rates and the NP size studied, the shape of the NP concentration profiles remained similar. For the pure copolymer, we found that at low shear rates the stable structures were lamellae oriented parallel to the flow direction. At higher shear rates, the lamellae changed to the perpendicular orientation.

These transitions were observed in the snapshots and they were also monitored with plots of the shear viscosity versus shear rate and mean squared end to end distance in y direction vs. shear rate. The transition found for pure copolymers were likewise observed when NPs were introduced into the BCP. Specifically, selective NPs shifted the transition to higher shear rate while the non-selective NPs shifted it to lower values. Further, we found that among the selective NP composites, larger NP size and lower particle-polymer interaction shifted the critical shear rate to a lower value.

It is widely known that shear flow can have beneficial effects on the self-assembled structures, and that self-assembling copolymers can be used as a nanoscale template to control the 3-dimensional arrangement of nanoparticles. In this paper, we married these two concepts and, based on our modeling and simulation, we speculate that shear rate can be used as another parameter to further control nanoparticle location.

BIBLIOGRAPHY

[1] Bockstaller, M.R.; Mickiewicz, R.A.; Thomas, E.L. *Adv. Mater.* **2005**, 17, 1331.

[2] Buxton, G.A.; Balazs, A.C. *Phys Rev. E* **2003**, 67, 031802.

[3] Pryamitsyn, V.; Ganesan, V. *Macromolecules* **2006**, 39, 8499.

[4] Balazs, A. C.; Emrick, T.; Russell, T. P. *Science* **2006**, 314, 1107.

[5] Hamley, I.W. *Angew. Chem. Int. Ed.* **2003**, 42, 1692.

[6] Shenhar, R.; Norsten, T.B.; Rotello, V. *Adv. Mater.* **2005**, 17, 657.

[7] Chui, J. J.; Bumjoon, J. K.; Kramer, E. J.; Pine, D. J. *J Am. Chem. Soc.* **2005**, 127, 5036.

[8] Schultz, A. J.; Hall, C. K.; Genzer, J. *Macromolecules* **2005**, 38, 3007.

[9] Thompson, R.B.; Ginzburg, V.V; Matsen, M.W.; Balazs, A.C. *Science* **2001**, 292, 2469.

[10] Huh, H.; Ginzburg, V.V; Balazs, A.C. *Macromolecules* **2000**, 33, 8085.

[11] Hamley, I.W. *J Phys.: Condens. Matter* **2001**, 13, R643.

[12] Wiesner, U. *Macromol. Chem. Phys.* **1997**, 198, 3319.

[13] Fraser, B.; Denniston, C.; Muser, M. H. *J. Polym. Sci: B: Polym. Phys.* **2005**, 43, 970.

[14] Fraser, B.; Denniston, C.; Muser, M.H. *J. Chem. Phys.* **2006**, 124, 104902.

[15] Pozzo, D.C.; Hollabaugh, K.R.; Walker, L.M. *J. Rheol.* **2005**, 49, 759.

[16] Castelletto, V.; Ansari, I.A.; Hamley, I.W. *Macromolecules* **2003**, 36, 1694.

[17] Lee, C.H.; Kim, B.H.; Lim, S.T.; Kim, H.S.; Kwon, Y.K.; Choi, H.J. *J. Macromol. Chem. Phys.* **2006**, 207, 444.

[18] Weeks, J.D.; Chandler, D.; Anderson, H.C. *J. Chem. Phys.* **1971**, 54, 5237.

[19] Kremer, K.; Grest, G.S. *J. Chem. Phys.* **1990**, 92, 5057.

[20] Horsch, M.A.; Zhang, Z.; Iacovella, C.R.; Glotzer, S. *J. Chem. Phys.* **2004**, 121, 11456.

[21] Schultz, A. J.; Hall, C. K.; Genzer, J. *J. Chem. Phys.* **2002**, 117, 10329.

[22] Soddemann, T.; Dunweg, B.; Kremer, K. *Phys Rev. E* **2003**, 68, 046702.

[23] Evans, D.J.; Morris, G.P. *Statistical Machanics of Non Equilibrium Liquids*; Academic Press, California, 1990.

[24] Lees, A.W.; Edwards, S.F.; *J. Phys. C* **1972**, 5, 1921.

[25] Kroger, M.; Hess, S.; *Physical Review Letters* **2000**, 85, 1128.

[26] Allen, M.P.; Tildesley, D.J. *Computer Simulation of Liquids*; Oxford University Press, New York, 1987.

[27] Murat, M.; Grest, G.S.; Kremer, K. *Macromolecules* **1999**, 32, 595.

[28] Lisal, M.; Brennan, J.K. *Langmuir* **2007**, 23, 4809.

[29] DeGennes, P.G. *The Physics of Liquid Crystals, 2nd ed*; Oxford University Press, New York, 1993.

[30] Bockstaller, M.R.; Lapetnikov, Y.; Margel, S.; Thomas, E.L. *J. Am. Chem. Soc.* **2003**, 125, 5276.

[31] Lauter-Pasyuk, V.; Lauter, H.J.; Ausserre, D.; Gallot, Y.; Cabuil, V.; Kornilov, E.I.; Hamdoun, B. *Physica B* **1998**, 241, 1092.

[32] Pryamitsyn, V.; Ganesan, V. *Macromolecules* **2006**, 39, 8499.

[33] Guo, H. *The Journal of Chemical Physics* **2006**, 124, 054902.

[34] Zipfel, J.; lindner, P.; Tsianou, M.; Alexandridis, P.; Richtering, W. *Langmuir* **1999**, 15, 2599.

[35] Guo, H. *The Journal of Chemical Physics* **2006**, 125, 214902.

[36] Hanley, K.J.; Lodge, T.P. *Macromolecules* **2000**, 33, 5918.

[37] Matsen, M.W. *Macromolecules* **1995**, 28, 5765.

[38] Rychkov *Macromolecular Theory and Simulations* **2005**, 14, 207.

[39] Pryamitsyn, V.; Ganesan, V. *Macromolecules* **2006**, 39, 844.

[40] Pryamitsyn, V.; Ganesan, V. *J. Rheol.* **2006**, 50, 655.

[41] Zhang, Y.; Wiesner, U.; Spiess, H.W. *Macromolecules* **1995**, 28, 778.

[42] Leist, H.; Maring, D.; Thurn-Albrecht, T.; Wiesner, U. *J. Chem. Phys.* **1999**, 110, 8225.

[43] Gupta, V.K.; Krishnamoorti, R.; Kornfield, J.A. Smith, S.D. *Macromolecules* **1995**, 28, 4464.

[44] Gupta, V.K.; Krishnamoorti, R.; Chen, Z-R.; Kornfield, J.A.; Smith, S.D.; Satkowski, M.M.; Grothaus, J.T. *Macromolecules* **1996**, 29, 875.

[45] Chen, Z-R.; Kornfield, J.A.; Smith, S.D.; Grothaus, J.T.; Satkowski, M.M. *Science* **1997**, 277, 1248.

CHAPTER 7

EFFECT OF SHEAR ON NANOPARTICLE DISPERSION IN POLYMER MELTS: A COARSE-GRAINED MOLECULAR DYNAMICS STUDY

7.1 Abstract

Coarse-grained, molecular dynamics simulations have been conducted to study the effect of shear flow on polymer nanocomposite systems. In particular, the interactions between different components have been tuned such that the nanoparticle-nanoparticle attraction is stronger than nanoparticle-polymer interaction, and therefore, the final equilibrium state for such systems is one with clustered nanoparticles. In the current study, we focus on how shear flow affects the kinetics of particle aggregation in systems with polymers of different chain lengths. The particle volume fraction and size are kept fixed at 0.1 and 1.7 MD units, respectively. Through this work, shear has been shown to significantly slow down nanoparticle aggregation, an effect that was found to be a strong function of both polymer chain length and shear rate. To understand our findings, a systematic study on effect of shear on particle diffusion and an analysis of relative time scales of different mechanisms causing particle aggregation have been conducted. The aggregation rate obtained from the time scale analysis is in good agreement with that determined from the aggregation time derived from the pair correlation function monitored during simulations.

7.2 Introduction

Polymer nanocomposites offer a new spectrum of materials that combine novel functionalities such as optical, electrical, and magnetic, while maintaining the manufacturing and processing flexibility inherent to plastics [1]. Often significant effort must be made to avoid the aggregation of nanoparticles (NPs) and thereby ensure a homogeneous dispersion of NPs in a polymeric material. Typically, one would modify the surface of nanoparticles to enhance the interaction between polymer and filler, and reduce particle-particle attraction. Advanced synthetic strategies have been developed to fine tune the chemical nature of the surface ligands and control NP aggregation [2, 3]. The modified chemical surface, along with other secondary parameters such as ratio of NP to radius gyration of polymer matrix chain, aspect ratio and volume fraction of NPs, will then define the effective inter-particle interactions and their state of dispersion in the polymer matrix. However, one needs to be careful before surface modifying NPs used to augment properties such as catalytic, magnetic or electrical. NP surface modification can often lead to loss of material properties. For example, it is well known that chemical functionalization disrupts the extended π conjugation of carbon nanotubes and reduces the electrical conductivity of isolated nanotubes [4]. A second example of such nanoparticles whose surface modification disrupts their functionalities is catalytic NPs, which for example, makes the development of low cost, commercially viable fuel cells contingent upon prevention of catalyst nanoparticle aggregation and their dispersion throughout the triple point surfaces. Yet, the development of techniques for NP dispersion without sacrificing their inherent properties has remained a significant challenge.

Balazs and coworkers [5, 6] developed a strategy to disperse sheets of clay in a polymer matrix using self consistent field theory and density functional theory. They added a small volume fraction of end-functionalized polymer chains to the polymer/clay composite such that the end group is attracted to the sheets of clay, while the remaining chain is identical to the bulk polymer chains. Mechanical stresses such as shear have been shown to cause the breakdown of NP agglomerates and subsequent individualization and dispersion of the particles. Anderson *et al* [7] used molecular dynamics simulations to show how shear can break up silicate tactoids in a polymer matrix by its sliding mechanism, similar to a shear-induced breakdown of carbon black superstructure observed during processing of filled rubbers [8]. However, no such breakdown has been observed for carbon nanotube aggregates due to strong inter-tube interaction. This has prevented the use of shear to obtain NP dispersions for other applications where particles with unmodified surfaces (and hence strong inter-particle interactions) need to be used, such as catalysis. In such systems, if we can devise ways to manipulate aggregation time scale vs. the time scale of material fabrication/processing (from the solution state), we can develop advanced materials with improved dispersion of nanoparticles.

We recently obtained some exciting results on nanocomposite nanofibers, where we used weakly modified (making them isoprene selective) magnetite NPs with poly(styrene-*b*−isoprene) (PS-*b*−PI) nanofibers [9]. These nanoparticles formed aggregates for as small as 0.01 NP weight fraction in solvent cast films and nanorods of PS-PI due to strong NP-NP attraction. While for the case of nanofibers, we were able to place 20 wt% NPs selectively to the isoprene domain. We speculated that this is an effect of deformation and fast solvent evaporation during the electrospinning process used to fabricate our materials.

We believe that the deformation can have beneficial effects on kinetics of particle aggregation. This, combined with fast solvent evaporation, that restricts the time scale of the process to an order of 10^{-3}seconds, helps to freeze the morphology in a state of dispersion. Although, such a state of dispersion is the desired one, it is believed to be a metastable state given the interaction potentials within the system.

In this work, we study the effect of shear flow in controlling the kinetics of the aggregation process of NPs that have strong inter-particle interaction using coarse grained molecular dynamics. We would refer to these particles as 'self attracting'. We aim to understand what role shear plays in delaying the aggregation of self attracting NPs to design processes for fabricating nanocomposites with well dispersed unmodified nanoparticles, while retaining the inherent properties of the fillers. With this study, we hope to outline different conditions where shear would be most beneficial. For this purpose, we study the effects of polymer matrix chain length, NP-NP attraction strength and shear rate on nanoparticle dispersion and discuss the mechanisms responsible for such effects. To the best of our knowledge, this is first molecular dynamics simulation study where effect of shear is being used to control the kinetics of self attracting NP aggregation in polymer nanocomposites.

A proper experimental characterization of these systems is rather complicated as the physically relevant length scales range from macroscopic down to molecular dimensions. Molecular dynamics is a powerful tool that can provide insight into basic scientific phenomena at different length and time scales. Furthermore, it offers direct access to particle coordinates and helps to quantify the state of dispersion, unlike experimental techniques where quantification at such

levels is a major challenge.

Although shear flow, studied in this work, does not represent dominant elongational deformation, it serves as a first step towards understanding our results on electrospun nanocomposite nanofibers [9]. Furthermore, this work will open pathways to utilize shear as a dispersion strategy for self-attracting nanoparticles and optimize processing technologies. In addition, shear being an industrially important process, this study will help to understand how nanocomposites with self attracting NPs behave under standard industrial processing conditions and will help to integrate optimized conditions into existing processes. With this work, we hope to provide a step towards development of generalized principles for dispersion of arbitrary particles differing in chemical nature, size and shape.

In the following section we describe the manner in which we modeled the block copolymer and the nanoparticles. We show the pair-wise potentials for all species, and we provide details on the computational method employed. In the Results and Discussion Section, we present simulation results on the polymer nanocomposites with self attracting NPs under shear flow. In particular, we probe the effect of polymer matrix chain length, and shear rate on NP state of dispersion and aggregation kinetics, and quantify our results using system properties such as NP pair correlation function and non bonded potential energy. Finally, we suggest mechanisms responsible for our findings via studies such as effect of shear on NP diffusion.

7.3 Model and Methods

7.3.1 Potentials

The polymer chains in the current study are modeled as fully flexible bead-spring chains where the monomers are never allowed to overlap. The excluded volume interactions between different monomer beads are accounted for by the purely repulsive, cut and shifted, Lennard-Jones (LJ) potential which is often referred to as the WCA potential [10],

$$u^{REP}(r) = 4\varepsilon\left[\left(\frac{\sigma}{r}\right)^{12} - \left(\frac{\sigma}{r}\right)^{6}\right] + \varepsilon = u^{LJ}(r) + \varepsilon, \quad r \leq 2^{1/6}\sigma \tag{7.1}$$

$$u^{REP}(r) = 0, \quad r > 2^{1/6}\sigma$$

where r is the separation distance between beads, and σ are ε are the Lennard Jones parameters, taken to be unity for the sake of simplicity. Within a polymer, the neighboring monomers are connected by a FENE (Finitely Extensible Nonlinear Elastic) potential [11],

$$u^{FENE}(r) = -\frac{1}{2}kR_{\max}^2 \ln\left[1 - \left(\frac{r}{R_{\max}}\right)^2\right] \tag{7.2}$$

where we set the spring constant, k, to 30, and the maximum extensibility, R_{max} , to 1.5 as described by Kremer and Grest [11].

Nanoparticles are modeled as spherical beads with σ=1.7 MD units. The interaction between NP and monomer is also modeled using fully repulsive WCA potential (equation 7.1) with σ adjusted according to NP and monomer

size. For NP-NP interaction, we use a slightly modified LJ potential cut and shifted at r =2.5σ (equation 7.3) to include a repulsive core for excluded volume and an attractive tail to model self attracting NPs. The NP-NP attraction is adjusted using the k value in equation 7.2. For k =1, the equation generates the conventional LJ attractive potential and for k=0, we obtain a purely repulsive WCA potential.

$$\begin{aligned} u^{ATT}[k] \quad &= 4\varepsilon\left[\left(\frac{\sigma}{r}\right)^{12} - \left(\frac{\sigma}{r}\right)^{6}\right] + ecut, \quad r \le 2^{1/6}\sigma \\ &= k * \left\{4\varepsilon\left[\left(\frac{\sigma}{r}\right)^{12} - \left(\frac{\sigma}{r}\right)^{6}\right] + u^{LJ}(2.5)\right\}, \quad 2^{1/6}\sigma \le r \le 2.5\sigma \\ &= 0, \quad r > 2.5\sigma \end{aligned} \tag{7.3}$$

where, *ecut* is the value by which $u^{ATT}[k]$ needs to be shifted to make the potential continuous at r= $2^{1/6}\sigma$.

NP-polymer and polymer-polymer interaction potentials are kept fixed for this work using equation 7.1. For NP-NP interaction, we use k =0, 0.5 or 0.8 in equation 7.3.

Our current simulation model neglects the effect of nanoparticle rotational dynamics on the rheological behavior of our systems. Note that although such rotational effects are irrelevant for thermodynamic behavior, they are important for flow behavior. It is expected, however, that such effects will become more significant the higher the concentration of nanoparticles in the system and the higher the shear rate. We assume that the nanoparticle surface functionalization is such that rotation modes tend to be suppressed and that for the relatively low nanoparticle concentration used in this work (10 vol%), such rotational effects are small compared to that of the translational modes. This is clearly an approximation but is expected not to greatly affect the qualitative response of our systems under shear flow.

7.3.2 Thermostat

We used a thermostat that preserves hydrodynamic interactions, i.e., the Dissipative Particle Dynamics (DPD) thermostat. DPD is a simulation technique that was originally conceived to model the interaction of mesoscopic units. The interactions between sites are treated as "soft" potentials meaning that the mesoscopic units can overlap. It was demonstrated by Soddemann *et al.* [12] that this thermostat is effective when using "hard" LJ potentials as is being used in this work. For details on the thermostat, we request the reader to refer to our recent paper on coarse-grained MD simulations of block copolymer nanocomposites [13].

7.3.3 Simple Shear Flow

In our MD code, we implemented shear flow with the SLODD algorithm using the following equations of motion [14]:

$$\frac{d\vec{r}_i}{dt} = \frac{\vec{p}_i}{m_i} + \hat{i}\,\dot{\gamma} y_i \tag{7.4}$$

$$\frac{d\vec{p}_i}{dt} = \vec{F}_i - \hat{i}\,\dot{\gamma} p_{yi} \tag{7.5}$$

where, $\vec{p}_i$ is the peculiar momentum of particle/bead i, and $\dot{\gamma}$ is the shear rate, and $\hat{i}$ is the unit vector in x direction. By this method we can impose a linear velocity profile in the x direction with a constant gradient in the y direction (with z as the neutral direction). These equations of motion are implemented with compatible Lee-Edwards periodic boundary conditions [15], wherein two opposing periodic images are incrementally moved in opposite directions consistent with the applied shear rate. Plots of shear viscosity versus shear rate

for polymeric fluids have been widely published in the literature [16], and they clearly demonstrate these fluids exhibit a Newtonian regime at low shear rates and shear thinning at higher shear rates. The pressure tensor can be calculated from simulations using [17],

$$P = \frac{1}{V}\left(\sum_{i}^{nM}\frac{p_i p_j}{m_i} + \sum_{j>i}^{nM} r_{ij}F_{ij}\right) \tag{7.6}$$

From this, we can determine the shear viscosity by the following relationship,

$$\eta = -\frac{P_{xy}}{\dot{\gamma}} \tag{7.7}$$

7.3.4 Computational Details

The particle volume fraction was fixed at 0.1 for all systems. The site density, ρ, was kept fixed at 0.85 and the temperature, k_BT, was kept at 1.0. The velocity verlet algorithm was used to integrate the equations of motion with a time step=0.01 for low shear rates and 0.005 for high shear rates. To make the code efficient, we used a cell list algorithm [17]. The system was initialized such that the chains were well equilibrated and particles were well dispersed in the polymer melt as seen from the NP pair correlation function (g(r)) [11, 17]. To calculate the diffusivity of nanoparticles during shear flow, we calculated the unconvected mean squared displacement of NPs in y and z direction such that:

$$< r^2 >=< r_y^2 + r_z^2 >= 4D_{NP}t \tag{7.8}$$

Where D_{NP} is the diffusivity of nanoparticles and t is the time. All diffusion coefficients in this work are calculated for a system with $k = 0$ (in equation 7.3), i.e NP-NP interaction is same as NP-polymer. This, we believe is a valid approximation as we monitor time scales and dynamics of different systems

before the actual onset of aggregation. Hence, we do not expect any effect of NP-NP attraction on NP diffusion in any system. We discuss this in more detail in the results section.

The NP diameter used for the current work is 1.7 MD units, which has been shown to have an approximate real diameter of 1.18 nm by Kairn *et al.* [18]. Although quite small, the particles do lie in the nanoparticle regime. We varied the polymer chain size from 1 to 400 beads and shear rate from 0 to 0.15 MD units. To keep NP volume fraction at 0.1, we used 2 NPs (size=1.7) for every 90 monomer beads (size=1.0). To quantify the state of dispersion of nanoparticles, we used a fixed peak value of NP pair correlation function as a reference point, which is identified as the onset of aggregation using simulation snapshots. The aim of the current study is to devise methods that can help in increasing the time scale of self attracting NP aggregation beyond the fabrication time scale itself in order to obtain well dispersed systems of self attracting NPs. Therefore, we concentrate on nanocomposite properties such as NP diffusion mostly at the initial stages before the onset of aggregation and t_{agg} is defined as the time elapsed before the onset of aggregation. The initial condition used in all runs is a well dispersed system. The idea is to be able to use shear flow in solution based material fabrication where the NPs are initially well dispersed (either due to stabilization by solvent in case of weakly modified particles or due to techniques such as ultrsonication used for pure nanoparticle solution) and later start to aggregate as the solvent evaporates. However, in this work we use a simplified system by using a polymer melt and not taking into account any effect of solvent evaporation. Table 7.1 summarizes some of the parameters used in this work.

Table 7.1: Simulation Parameters

Parameters	**Symbol**	**Value (MD units)**[1]
Temperature	k_BT	1
monomer size	σ	1
NP diameter	σ_P	1.7
Chain length	N	1-400
Bead density	ρ	0.85
NP fraction	ϕ_P	0.1
Number of chains	M	100-2000
MD integration time step	Δt	0.005-0.01
NP-NP attraction parameter	k	0.5, 0.8
Shear rate	$\dot{\gamma}$	0-0.15

[1]The values in MD units are understood to be multiplied by the appropriate combinations of three independent fundamental units of length, mass and energy [17].

7.4 Results and Discussion

As mentioned above, this work has been initiated as a step towards understanding the effect of deformation on controlling (self-attracting) nanoparticle location in electrospun nanofibers [9]. In addition to providing a reasonable mechanism responsible for our experimental findings, this work will provide a systematic computational study on the effect of deformation on polymer nanocomposites with focus on the kinetics of aggregation, and will establish the possibility

of beneficial use of flow to fabricate well dispersed nanoparticle-based systems. Figure 7.1 shows snapshots of a polymer nanocomposite melt under quiescent condition ($\dot{\gamma}$=0) for N=10 and k =0.5 (NP-NP interaction). The polymer chains are blanked out for clarity and only nanparticles are shown in the figure. The figure shows how the particles aggregate into clusters in 1500 MD time units.

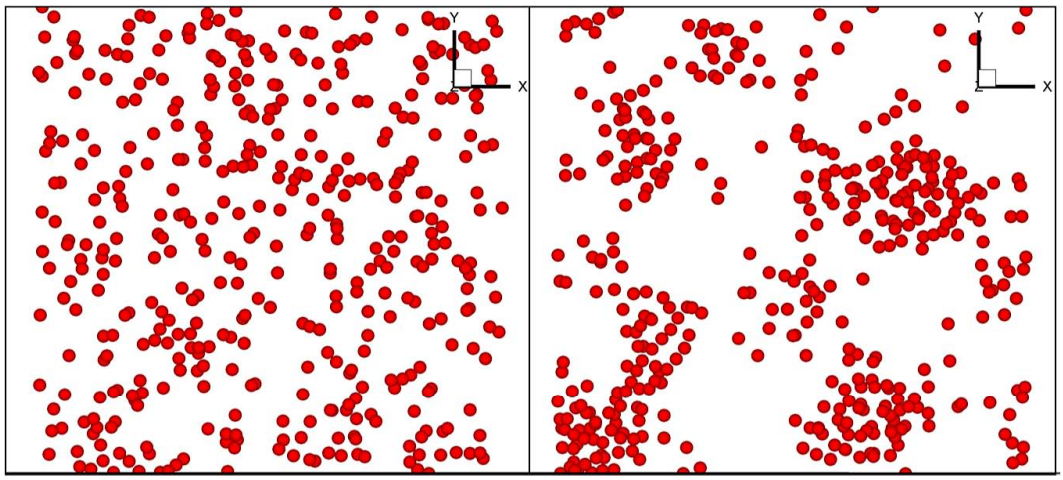

Figure 7.1: Self attracting NP polymer nanocomposites. (a) Snapshots for $\dot{\gamma}$ =0 at (left) t=0, and (right) t=1500 MD units. Matrix chain length is N=10 and k=0.5 for NP-NP attraction. Polymer chains have been removed for clarity.

Figure 7.2 shows similar snapshots for systems under different shear rates. At t=1500 MD units, no trace of aggregation is seen for both $\dot{\gamma}$ = 0.05 and $\dot{\gamma}$=0.1. Slight onset of aggregation is seen for $\dot{\gamma}$=0.05 at t=3000, while for $\dot{\gamma}$=0.1, NPs are still well dispersed.

These results are quantified in figure 7.3 using pair correlation function for different shear rates at different times. A strong second order peak for $\dot{\gamma}$ =0 (starting at t=500) shows the formation of NP aggregates [19]. The absence of a second order peak clearly shows that the particles are well dispersed for $\dot{\gamma}$=0.1 even at t=3000, while a small second peak for $\dot{\gamma}$=0.05 at t=3000 shows the onset of aggregation. We would like to point out here that even at $\dot{\gamma}$=0.1, the NPs do eventually aggregate, but they do so at a much later time. These results demonstrate that shear can significantly slow down the aggregation process, and the higher the shear rate, slower is the aggregation.

We note that under shear flow the pair correlation function peaks always grow with time and stabilize once all particles cluster into a single aggregate. This shows that no shear induced rupture or breakage of particle clusters takes place. This effect, we believe is a strong function of NP-NP attraction and shear rate. For the inter-particle attraction (relative to shear rate) used in this work, adhesive forces between any two particles overpower the shear forces resisting any breakage of clusters. The shear effect, in such a system, is most prominent in the initial stages of the aggregation process where the nanoparticles are relatively far away from each other and the process is diffusion limited. Such a system is experimentally very relevant, since the surface energies of most inorganic fillers are many orders of magnitude higher than polymer surface energies making the inter-particle attractions very strong.

Similar studies were conducted for stronger NP-NP attraction (k=0.8). Figure 7.4a shows the pair correlation function for different shear rates at various times for k =0.8. The matrix chain length is kept fixed at N=10. For $\dot{\gamma}$=0.1, the shear effect is not as drastic as for k=0.5 system due to stronger NP-NP attrac-

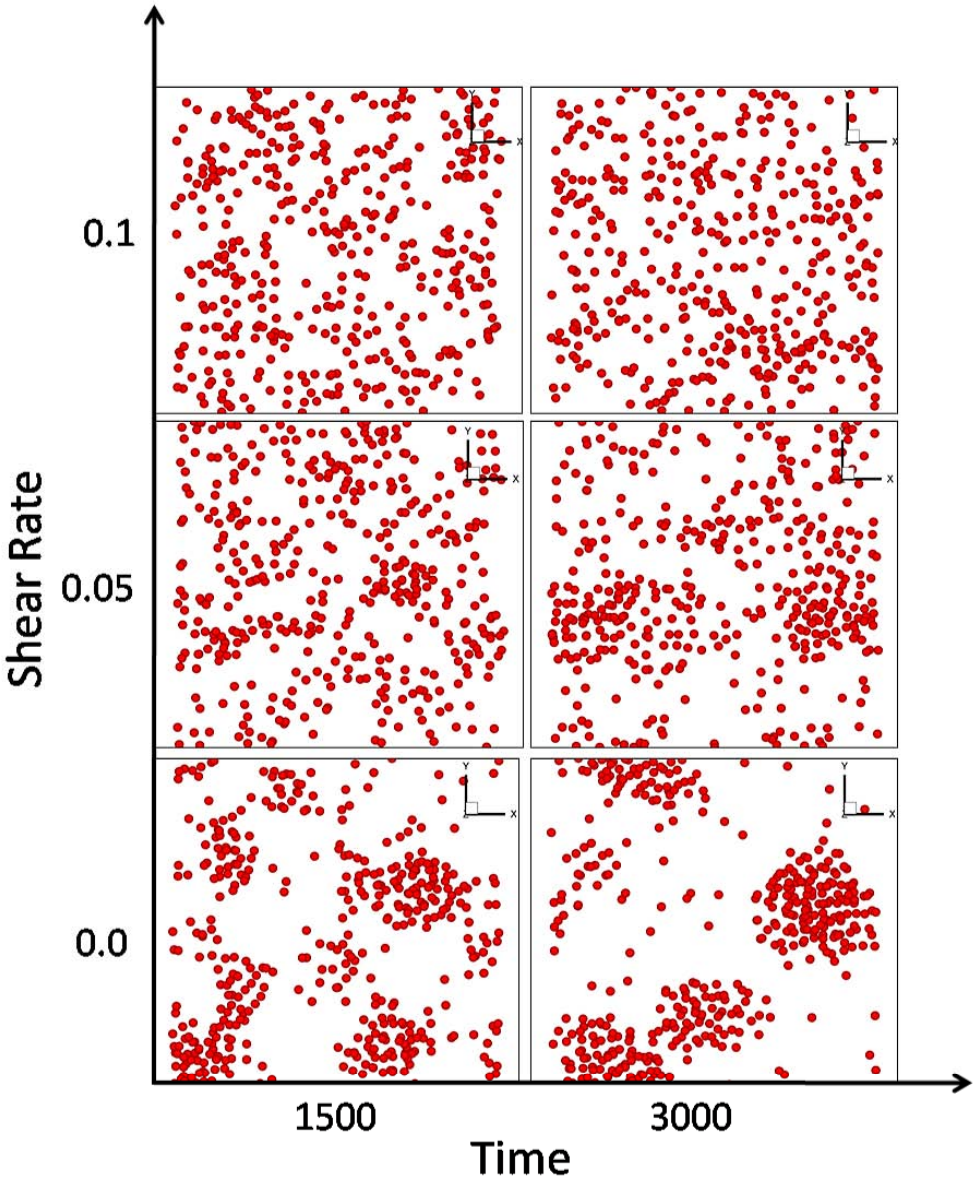

Figure 7.2: Self attracting NP polymer nanocomposites. Snapshots of systems at $\dot{\gamma}$=0.0, 0.05, and 0.1 at different elapsed MD times. For all figure parts, matrix chain length is N=10 and k=0.5 for NP-NP attraction. Polymer chains have been removed for clarity .

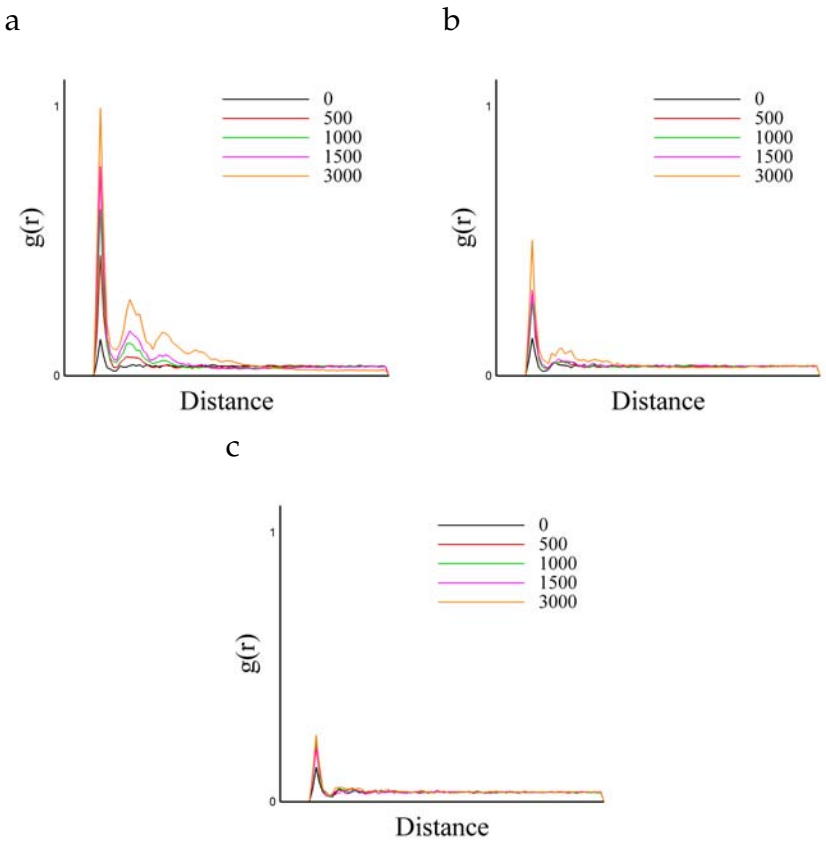

Figure 7.3: NP pair correlation function at $\dot{\gamma}$= a) 0.0, b) 0.05 and c) 0.1 at different elapsed times. For all figure parts, matrix chain length is N=10 and k=0.5 for NP-NP attraction. The curves have been normalized with the maximum peak value at $\dot{\gamma}$=0.0.

tion. A significant shear induced dispersion of particles can be achieved for $\dot{\gamma}$=0.15. The results can be further quantified by tracking the interaction energy between nanoparticles. As we see in figure 7.4b, the non-bonded potential energy (PE) between nanoparticle pairs decrease with time as nanoparticles start to minimize the distance between them. The PE curve also presents the energetic reason favoring nanoparticle aggregation and shows that shear changes the kinetics of this energetically favorable process. Since the simulations are run at a constant temperature, the drop in potential energy is an effect of clustering only.

a

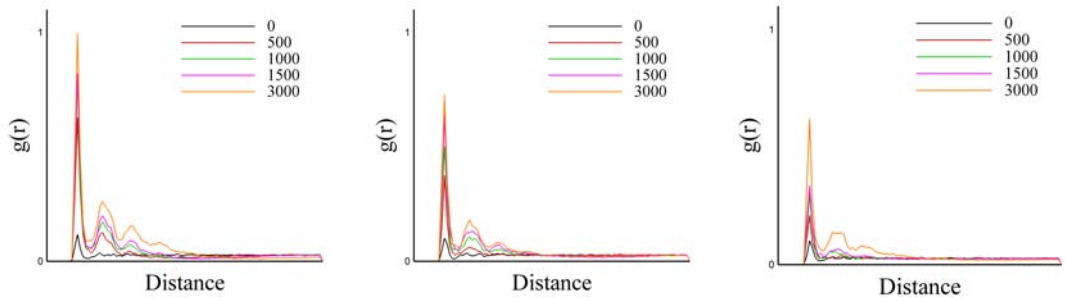

b

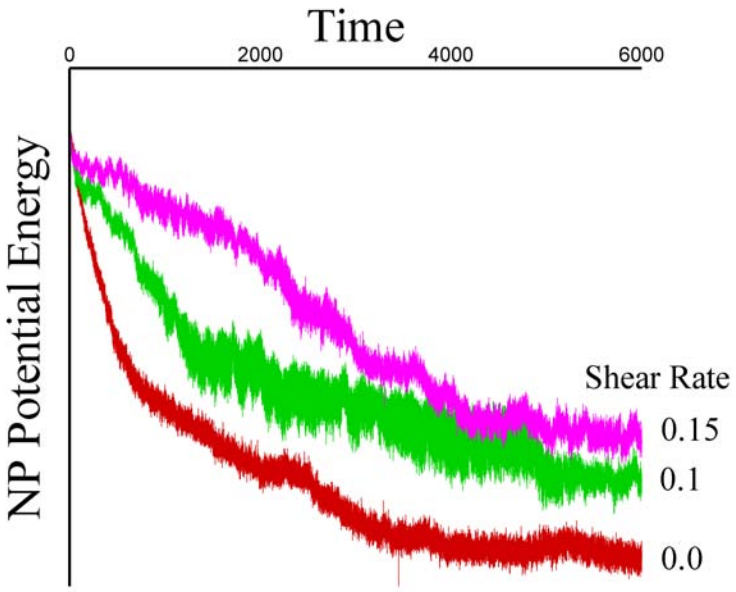

Figure 7.4: NP pair correlation function at $\dot{\gamma}$= (left) 0.0, (center) 0.1, and (right) 0.15. (b) Non bonded potential energy between NP pairs at different shear rates as a function of time. Matrix chain length N=10 and k =0.8 for NP-NP attraction. The curves have been normalized with the maximum peak value at $\dot{\gamma}$=0.0.

We speculate two main effects of shear, first being deformation leading to increase in instantaneous inter-particle distance and second being the effect of shear on nanoparticle diffusion coefficients. One or both of these effects would play a role depending on the time scale of shear vs. the time scale of NP diffusion in a particular system.

a

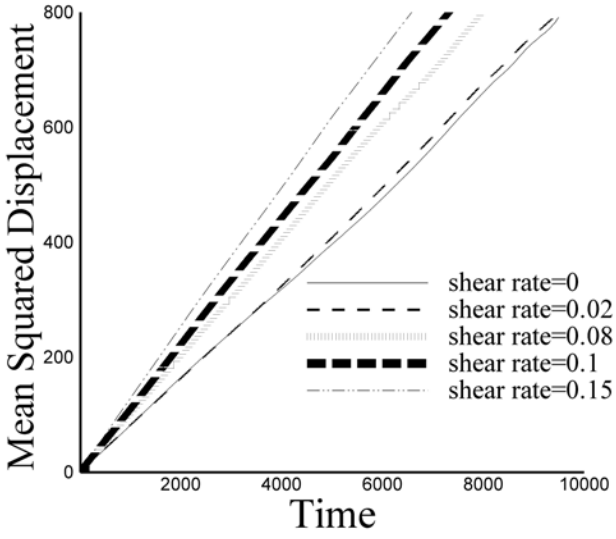

b

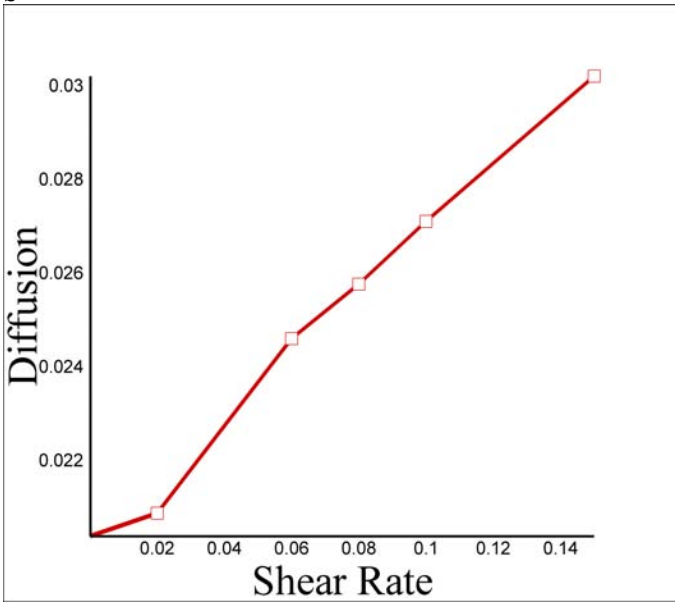

Figure 7.5: Diffusion measurements for system with N=10 and k =0 **a)** Unconvected NP mean squared displacement vs. time for different shear rates b) Diffusion coefficients calculated using equation 7.8 as a function of shear rate.

The first effect can be viewed as being analogous to shear induced breakdown seen during processing of filled rubbers, except here this rupture is taking place when particles are still not part of any cluster. For the particular parameters in this work, as we mentioned above, a real rupture is not seen once a cluster is formed. This rupture-like effect of shear is anticipated as positive in all conditions leading to slower aggregation. This effect is expected to increase with increasing shear rate and be independent of the matrix chain length. However, for the second effect, a detailed study would be very interesting and beneficial. To understand the effect of shear on nanoparticle diffusion, we first plotted mean squared displacement traveled by nanoparticles in a polymer matrix with N=10 for shear rate=0 to 0.15 in figure 7.5a. Figure 7.5b shows the calculated diffusion coefficient values for nanoparticles as function of shear rate using the slope of the curves from fig. 7.5a and equation 7.8. We find that the diffusivity increases with shear rate. Diffusion constants in liquids have been shown to significantly increase under shear flow [20, 21, 22]. This effect has also been seen for systems of particles suspended in liquids both using experiments [23, 24, 25] and simulations [26, 27]. Malandro *et al* [28] conducted Non Equilibrium Molecular Dynamics simulations to study the self diffusion of liquids. They showed that local minima of potential energy disappears under shear strains, leading to mechanical instabilities forcing the system towards alternate local minima causing a shear induced enhancement in diffusion.

Due to the small size of the nanoparticles [13], their diffusion can be compared to that of liquids and an enhancement of diffusion under shear for our system is reasonable. However, an interesting question that needs to be answered here is: *Does the NP diffusion follow the same trend with varying shear rate irrespective of the matrix chain length?* This is particularly important as most in-

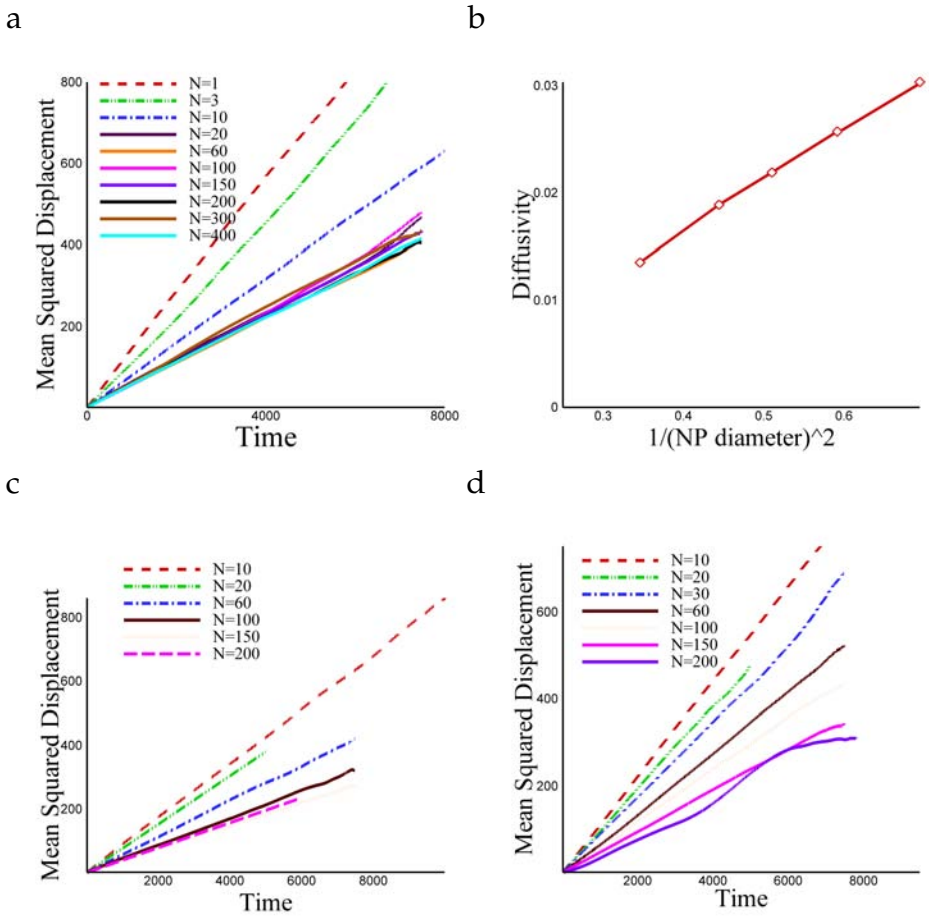

Figure 7.6: Unconvected NP Mean squared displacement for different matrix chain lengths as a function of time (k=0) a) $\dot{\gamma}$=0 c) $\dot{\gamma}$=0.05 d) $\dot{\gamma}$=0.1. Part b) shows the diffusion coefficient values for different NP diameters at $\dot{\gamma}$=0 and N=60.

dustrially relevant polymers have extremely high degree of polymerization and are way beyond the entanglement length (for bead spring model the entanglement length is N~35) [11]. Once we conclusively establish the effect of shear on NP diffusion in various matrix chain lengths, the most important question that will still remain unanswered is: *What effect does enhanced NP diffusion have on aggregation kinetics? Does it speed up the aggregation or does it homogenize the system?* To answer these questions and understand the effect of various parameters on

kinetics of NP aggregation, we studied the diffusion of NPs in polymer matrices with N varying from 1 to 400.

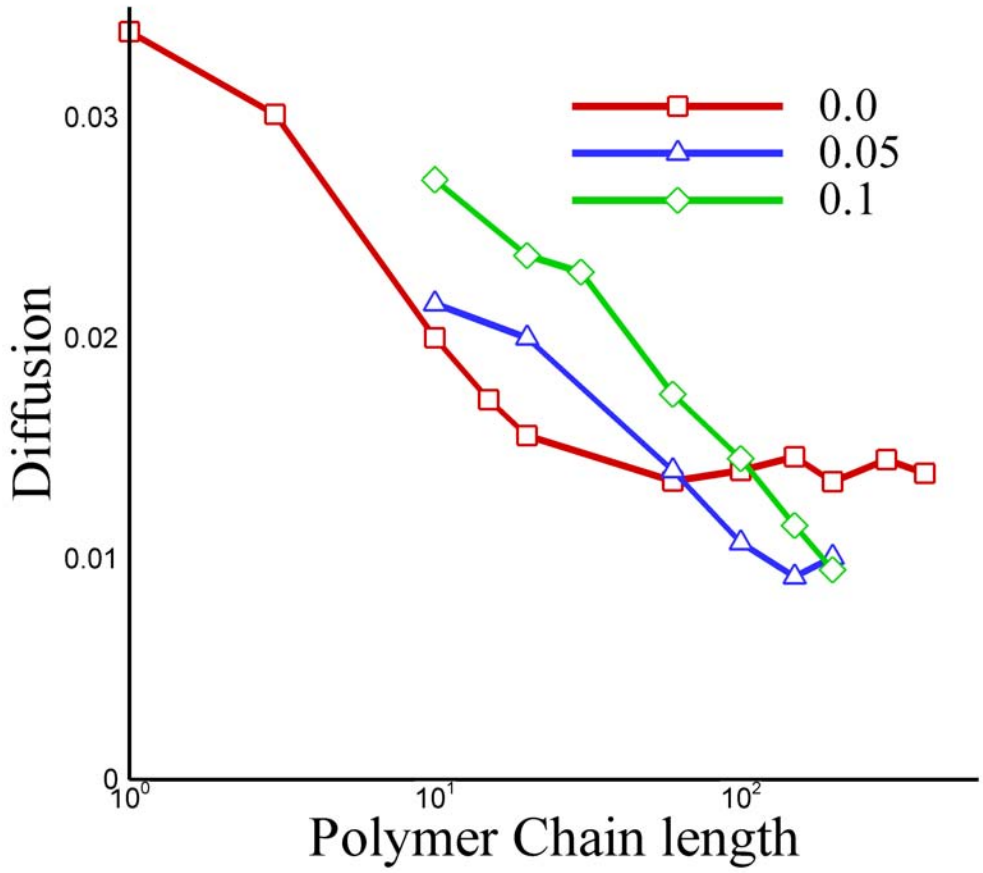

Figure 7.7: Diffusion Coefficients as a function of matrix chain length (N) for different shear rates.

We would again like to point out here that diffusion coefficients in this work (as shown below) are calculated for a system with $k = 0$ (in equation 7.3), i.e NP-NP interaction is same as NP-polymer. This, we believe is a valid approximation as we monitor time scales and dynamics of different systems before the actual onset of aggregation. In addition, for all systems, the time taken by NPs to even start aggregating is much larger than the diffusion time scales, therefore, we

assume that at time scales relevant to diffusion, the nanoparticles do not feel attracted to each other.

Figure 7.6a shows the mean squared displacement of NPs in various matrices for $\dot{\gamma}$=0. As shown in the figure, the diffusion rate decreases with increasing chain length initially up to N=20. This is expected due to a rise in viscosity with increasing chain length. A curve of Diffusivity vs. Inverse of viscosity (not shown) for N=1 to 20 falls on a straight line, in accordance with Stokes Einstein relation. However, the interesting observation in this figure is that beyond N=20, all curves collapse on the same line, in spite of significant increase in the bulk polymer viscosity. Tuteja *et al.* recently studied the diffusion of Cadmium Selenide nanoparticles in a polymeric liquid. They suggested that for nanoparticles smaller than the "tube diameter", the local friction is dependent only on a layer of monomers rubbing next to the particle surface, and is therefore proportional to the nanoparticle area and is independent of the full chain length. A remarkable prediction of this theory is that the diffusion rate of such a small particle will be independent of the polymer chain length or bulk viscosity. Extending this theory to suit our particular system, we believe that the diffusion of NPs in a polymer melt should become constant beyond a certain chain length N=N_{crit}; such that the area spanned by a NP of diameter d=cross-sectional area of the polymer chain with N=N_{crit} ($\sim (R_{gyr})^2$). This explains the constant Diffusion rate for higher N values after an initial drop in diffusivity with chain size. We plotted the diffusivity of nanoparticles with different diameters for N=60 (>N_{crit}) at $\dot{\gamma}$=0 and found that diffusivity is inversely proportional to the NP area ($\sim d^2$) as expected (figure 7.6b). Next, we studied the effect of chain size on NP diffusion under shear flow. Figure 7.6c and 6d shows the mean squared displacement for NPs with diameter=1.7 at $\dot{\gamma}$=0.5 and 0.1 respectively for dif-

ferent N. The diffusion monotonically decreases with increasing N upto N=100 and becomes constant beyond that for $\dot{\gamma}$=0.05, while for $\dot{\gamma}$=0.1, diffusion monotonically decreases for the entire range of N studied. The result in figure 7.6a, c and d is summarized in figure 7.7 by plotting diffusivity as a function of N for different shear rates. From the results of figure 7.7, it appears that diffusion rate vs. N under shear flow follows the same trend as for quiescent system, except N_{crit} shifts to a larger value, indicating that the area spanned by the nanoparticles is a lot larger under shear flow than under quiescent conditions. Therefore, for example, for the case of $\dot{\gamma}$=0.05, the total matrix or bulk viscosity due to long chained polymers makes a significant contribution to the NP diffusion rate upto a N_{crit}= 100.

For a closer look at the effect of shear on NP diffusion rates, we revisited the study we did in Figure 7.5, except this time it is for N=150 ($N >> N_{crit}$). Figures 7.8a and b show the NP diffusivity measurements in a polymer melt with N=150 for a range of $\dot{\gamma}$=0 to 0.15. The diffusivity initially decreases up to $\dot{\gamma}$=0.05 and then starts to increase. From the results of figure 7.5, 7.7 and 7.8, we speculate that there are two main factors that play a role in defining NP diffusivity in polymer melts under shear flow, first is shear enhanced diffusion as we saw in figure 7.5, and second is the effect of local matrix viscosity which increases with shear rate as the area spanned by the NPs increases and therefore, this effect works to reduce the diffusion rate as a function of shear. The latter effect can be seen only for large chain polymers. Figure 7.6 shows that for N=150, the second force is dominant for lower shear rates, while for higher shear rates, the first effect takes over. In figure 7.8c, we plot the diffusion vs. shear rate for different matrix chain lengths. And again we find that for short chains the diffusion monotonically increases with shear rate due to shear enhanced diffusion, while

a

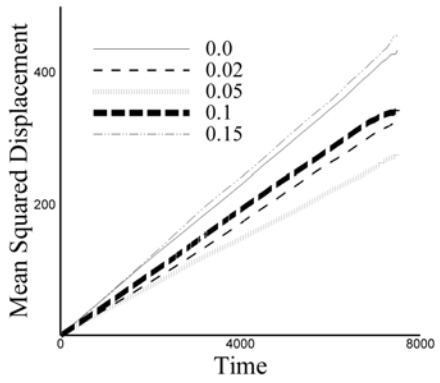

b

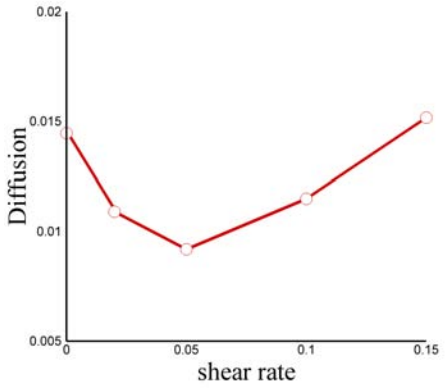

c

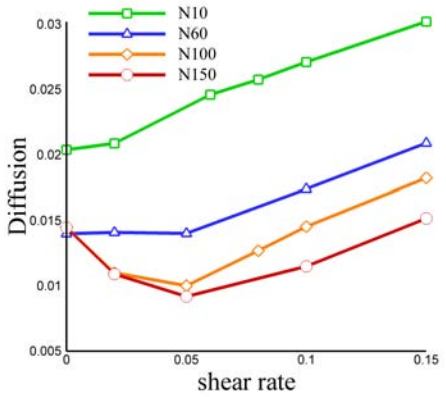

Figure 7.8: (a) Unconvected NP mean squared displacement for a polymer nanocomposite system with N=150 and k =0 at different shear rates as a function of time. (b) Diffusion coefficients calculated using slope of (part a) using equation 7.8 as a function of shear rate (c) Diffusion coefficients vs. shear rate for different matrix chain lengths.

for longer chains we see an initial decrease in diffusion due to the increase in matrix viscosity, followed by shear enhanced diffusion.

Finally, to zero in on the effect of diffusion and deformation during shear flow on the kinetics of NP aggregation, we do a time scale analysis as a function of both chain length and shear rate for a fixed NP-NP attractive potential (k=0.5). We define three time scales in this study, t_{diff} and t_{shear} and t_{agg}. t_{diff} is the time scale of diffusion and is $\sim R^2/D_{NP}$, where R=NP radius, D_{NP}=diffusion constant. t_{shear} is the time scale of deformation and is $\sim 1/\dot{\gamma}$. t_{agg} is the time elapsed before the onset of aggregation for a system with k =0.5. This is determined using a reference value of the pair correlation function (fixed using snapshots of various nanocomposite systems). We find that for the systems studied in this work, t_{agg} is at least 1-2 orders of magnitude higher than t_{diff} or t_{shear}. So at the time scales where diffusion and shear deformation play a role, system does not see any effect of NP-NP attraction, thereby behaving like a homogenous system with equal interaction between different components. This leads us to the assumption that for the time period before any real clusters are seen, the main forces responsible for the state of the system or for t_{agg} are solely diffusion and shear deformation. Based on this assumption, we predict the aggregation rates of various systems taking into account the time scales of NP diffusion and deformation only and compare these predicted values to the actual relative aggregation rates calculated using t_{agg}. Again, what we mean by aggregation rate here is the rate at which the onset of aggregation takes place.

In figure 7.9a, we plot the t_{diff}, and t_{shear} as a function of shear rate for N=10. For N=10, at low shear rates $t_{diff} < t_{shear}$. Both t_{diff} and t_{shear} decrease with shear rate as expected, however t_{shear} decreases at a much faster rate and for $\dot{\gamma} > 0.03$,

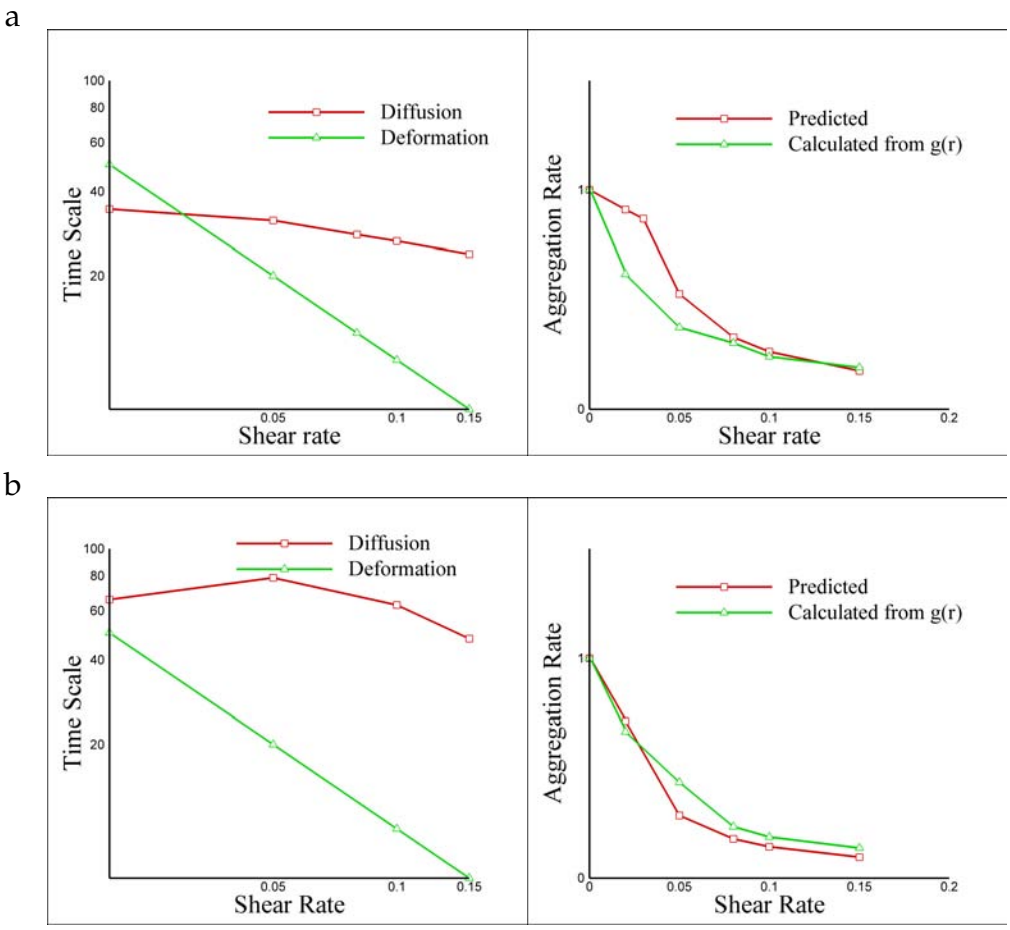

Figure 7.9: Time scale analysis of various forces and events during aggregation of nanoparticles under shear flow as a function of shear rate, a) N=10, b) N=150. In both figure parts, the left curve shows the time scales of shear/deformation and diffusion and the right curve shows the 'predicted' and 'calculated' normalized non-dimensional aggregation rates of nanoparticles. Please see text for explanation of various terms.

$t_{shear} < t_{diff}$. As we mentioned above, at the time scales of diffusion and shear, the system appears to be homogenous with no effect of NP-NP attractions. Therefore, we expect diffusion to be a homogenizing force, helping the particles to eliminate any concentration differences and disperse uniformly. For a similar reason, shear/deformation is expected to be a rupture-like positive force and homogenize the system at time scales dependent on the shear rate. However,

a

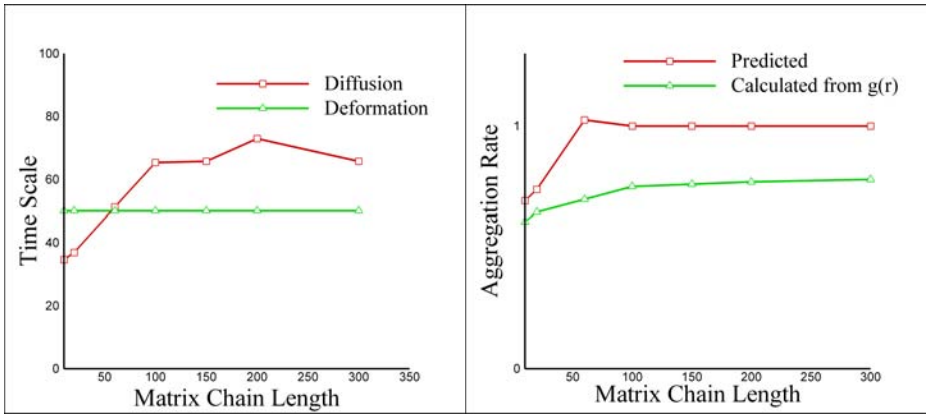

b

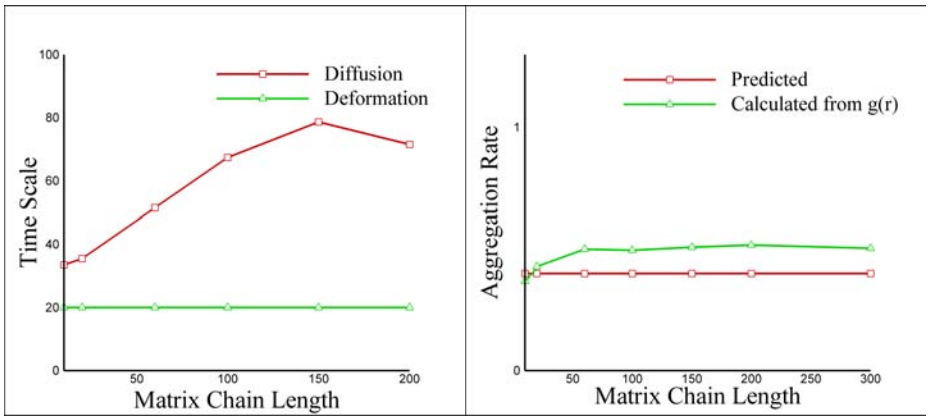

c

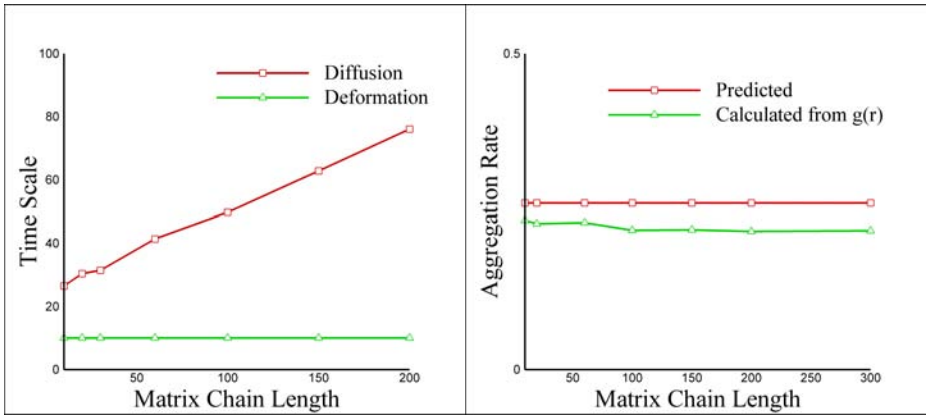

Figure 7.10: Time scale analysis of various forces and events during aggregation of nanoparticles under shear flow as a function of matrix chain length, a) $\dot{\gamma}$=0.02, b) $\dot{\gamma}$=0.05 c) $\dot{\gamma}$=0.1. In all figure parts, the left curve shows the time scales of shear/deformation and diffusion and the right curve shows the 'predicted' and 'calculated' normalized non-dimensional aggregation rates of nanoparticles. Please see text for explanation of various terms.

it still needs to be established which force (diffusion or shear) plays a dominant role in different scenarios. For this we define, another time scale=$t_{homogenizing}$ defined as the dominant force responsible for homogenizing the system. As seen from figure 7.9a (left), $t_{homogenizing}$ can be taken = t_{diff}, for $\dot{\gamma}$ <0.03, while for $\dot{\gamma}$ >0.03, $t_{homogenizing}$=t_{shear}. Due to the homogenizing character of both these forces, we expect the time scale of aggregation to be proportional to $1/t_{homogenizing}$, and the aggregation rate to be proportional to $t_{homogenizing}$. In figure 7.9a (right), we plot the non-dimensional 'predicted' aggregation rate as $t_{homogenizing}(\dot{\gamma})/t_{homogenizing}$ ($\dot{\gamma}$=0), where $t_{homogenizing}$ ($\dot{\gamma}$=0) is the normalizing factor. On the same curve, we also plot the non dimensional 'calculated' aggregation rate. This value is obtained from t_{agg} at different shear rates, normalized using t_{agg} at $\dot{\gamma}$=0. Here, the non dimensional 'calculated' aggregation rate is computed as t_{agg} ($\dot{\gamma}$=0)/t_{agg} ($\dot{\gamma}$) since the aggregation rate is inversely proportional to the time elapsed. We use the term the term 'calculated' as t_{agg} is obtained from the actual simulation snapshots. As seen in figure 7.9a (right), curves of both aggregation rates qualitatively follow a similar trend. However, there are deviations in aggregation rate values, particularly at smaller shear rates. This result suggests that at lower shear rates, where t_{agg} is relatively smaller, the difference between t_{agg} and t_{diff}/t_{shear} reduces. In such a scenario, the assumption that NP-NP attraction does not play a role might be an over simplification.

Figure 7.9b shows a similar time scale analysis for N=150. Here we find that that t_{shear} is the homogenizing force for the entire range of shear rates studied and we again see that 'predicted' and 'calculated' aggregation rates follow the same trend. Figure 7.10 shows the time scale analysis as a function of chain length N at 3 different shear rates ($\dot{\gamma}$=0.02, 0.05, 0.1). Here, t_{shear} remains constant with chain length, while t_{diff} follows the trend, as already seen in figure

7.7. Again, we see qualitatively similar trends for 'predicted' and 'calculated' aggregation rates. Deviations in quantitative comparisons again indicate the importance of including the effect of NP-NP attraction in the time scale analysis.

7.5 Conclusions

In this work, we have conducted a study on how shear flow affects the dispersion state of a polymer nanocomposite system, in which NP-NP attraction exceeds NP-polymer interaction. For the systems studied, the final state is always an aggregated particle cluster as it minimizes the energy of the system, However, as seen in this work, shear flow can greatly alter the kinetics of NP aggregation, and can increase the time scale of aggregation by up to 2 orders of magnitude. We find that the effect of shear is two fold: first is effect of shear on NP diffusion coefficient and second, is the deformation caused due to the shear. To zero in on these two mechanisms, we varied different parameters such as shear rate and polymer chain length. We find that effect of shear flow on NP diffusion is a strong function of polymer chain length and therefore can affect the aggregation time scale. A time scale analysis was done, comparing the time scales of different mechanisms responsible for aggregation/homogenization. This study provides a first step towards understanding how shear flow can be used to an advantage to obtain well dispersed states even in cases where NP-NP attractions are strong. A more detailed study is needed answering questions such as *1) how does NP diffusion vary with changing NP-NP attraction potential?, 2) Can faster diffusion lead to faster aggregation in certain scenarios?, 3) Can shear cause the particles to remain dispersed even at steady state in a certain scenario?, 4) In what*

cases, does shear lead to faster aggregation?. Further studies, particularly, on effect of changing NP-NP attraction and NP volume fraction (or NP-NP distance) are underway.

BIBLIOGRAPHY

[1] Balazs, A. C.; Emrick, T.; Russell, T. P. *Science* **2006**, 314, 1107.

[2] Watson, K.J.; Zhu, J.; Nguyen, S.T.; Mirkin, C.A. *J. Am. Chem. Soc.* **1999**, 121, 462.

[3] Skaff, H.; Ilker, M.F.; Coughlin, E.B.; Emrick, T. *J. Am. Chem. Soc.* **2002**, 124, 5729.

[4] Kalra V.; Joo, Y.L. *Proceedings of AIP Conferences* **2008**, 534, 1027.

[5] Ginzburg, V.V.; Balazs, A.C. *Adv. Mater.* **2000**, 12, 1805.

[6] Balazs, A.C.; Singh, C.; Zhulina, E. *Macromolecules* **1998**, 31, 8370.

[7] Anderson, K.L.; Sinsawat, A.; Vaia, R.A.; Farmer, B.L. *J. Polym. Sc.: Part B: Polym. Phys.* **2005**, 43, 1014.

[8] Bar-Chaput, S.; Carrot, C. *Rheol. Acta.* **2006**, 45, 339.

[9] Kalra, V.; Lee, J.; Lee, J.H.; Lee, S.G.; Marquez, M.; Wiesner, U.; Joo, Y.L. *Small* **2008**, 4, 2067.

[10] Weeks, J.D.; Chandler, D.; Anderson, H.C. *J. Chem. Phys.* **1971**, 54, 5237.

[11] Kremer, K.; Grest, G.S. *J. Chem. Phys.* **1990**, 92, 5057.

[12] Soddemann, T.; Dunweg, B.; Kremer, K. *Phys Rev. E* **2003**, 68, 046702.

[13] Kalra. V.; Mendez, S.; Escobedo, F.; Joo, Y.L. *J. Chem. Phys.* **2008**, 128, 164909.

[14] Evans, D.J.; Morris, G.P. *Statistical Machanics of Non Equilibrium Liquids*; Academic Press, California, 1990.

[15] Lees, A.W.; Edwards, S.F.; *J. Phys. C* **1972**, 5, 1921.

[16] Kroger, M.; Hess, S.; *Physical Review Letters* **2000**, 85, 1128.

[17] Allen, M.P.; Tildesley, D.J. *Computer Simulation of Liquids*; Oxford University Press, New York, 1987.

[18] Kairn, T.; Daivis, P.J.; Ivanov, I.; Bhattacharya, N. *J. Chem. Phys.* **2005**, 123, 194905.

[19] Starr, F.W.; Douglas, J.F.; Glotzer, S.C. *J. Chem. Phys.* **2003**, 119, 1777.

[20] Cummings, P.T.; Wang, B.Y.; Evans, D.J.; Fraser, K.J. *J. Chem. Phys.* **1991**, 94, 2149.

[21] Sarman, S.; Evans, D.J.; Baranyai, A. *Phys. Rev. A* **1992**, 46, 893.

[22] Baranyai, A.; Cummings, P.T. *Mol. Phys.* **1995**, 86, 1314.

[23] Qiu, X.; Ou-Yang, H.D.; Pine, D.J.; Chaikin, P.M. *Phys. Rev. Lett.* **1988**, 61, 2554.

[24] Abbot, J.R.; Tetlow, N.; Graham, A.L.; Altobelli, S.A.; Fukushima, E.; Mondy, L.A.; Stephans, T.S. *J. Rheol.* **1991**, 35, 773.

[25] Koh, C.; Hookham, H.; Leal, L.G.; *J. Fluid Mech.* **1994**, 266, 1.

[26] Xue, W.; Grest, G.S. *Phys. Rev. A* **1989**, 40, 1709.

[27] Chang, C.; Powell, R.L. *J. Fluid Mech.* **1994**, 281, 51.

[28] Malandro, D.L.; Lacks, D.J. *Phys. Rev. Lett.* **1998**, 81, 5576.

CHAPTER 8

COARSE-GRAINED MOLECULAR DYNAMICS STUDY OF BLOCK COPOLYMER/NANOPARTICLE COMPOSITES UNDER ELONGATIONAL FLOW

8.1 Abstract

Symmetric diblock copolymer/nanoparticle systems under planar elongational flow have been modeled and simulated using coarse grained, non-equilibrium molecular dynamics. The aim of our present study is to understand how the dispersion of nanoparticles in a block copolymer system is influenced by elongational flow, and how the presence of nanoparticles changes the rheology and flow-induced morphology transition in block copolymers. We consider two different kinds of spherical nanoparticles (NPs) categorized with respect to their interaction potential with the polymeric blocks, 1) selective NPs, that show a preference towards one of the blocks of a model diblock copolymer, and 2) non-selective NPs, that show equal attraction towards both blocks. For unrestricted simulation times during elongational flow, spatially and temporally periodic boundary conditions devised by Kraynik and Reinelt (Int. J. Multiphase Flow, 1992, 18, 1045) have been implemented. Our results show that the peak concentration of both selective nanoparticles at the center of the preferred domain and non-selective nanoparticles at the domain interface becomes broader with increasing elongation rate, suggesting that elongational flow can be used as another parameter to control nanocomposite self assembly. Our results also reveal that the onset of flow induced transition from lamellar to disordered morphology is also greatly influenced by particle-particle and particle polymer interac-

tions.

8.2 Introduction

Block copolymers have been attracting great attention in recent years as templates to guide the location of nanoparticles within polymeric matrices [1, 2, 3]. Such popularity stems from the tendency of block copolymers to self assemble into a variety of periodic meso-scale structures such as spheres, cylinders and lamellae when cooled below a certain temperature (T_{ODT} or Order-Disorder transition temperature) [1, 4]. The shape and size of such self assembly structures can be tailored using different compositions and molecular weights of the block copolymer, respectively. With carefully chosen characteristics of the block copolymer (composition and molecular weight) and nanoparticles (size and surface modifying ligands), one can periodically arrange the nanoparticles (NPs) in a desired pattern within the composite [2, 3]. Having the NPs periodically spaced can lead to synergistic effects of optical [2] and mechanical properties [3, 5], for example, and can potentially be used in novel applications such as magnetic storage media and catalysis [6, 7, 8].

Recently, numerous studies have been conducted to explore how various system parameters affect the equilibrium location of NPs within block copolymers (BCPs) using experiments, theory and computer simulations. In these studies, researchers varied parameters such as the interaction between the NP and the "A" or "B" monomer of an "AB" diblock copolymer or the size of the NPs (relative to the BCP end to end distance, R_0). In order to experimentally study the effect of interaction between different components of the system, one

would typically chemically coat the surface of the nanoparticles with short polymeric ligands. For example, one could synthesize 'selective' nanoparticles by chemically modifying the NP surfaces with ligands of block "A", for example in an "AB" diblock copolymer [9]. In another scenario, one could chemically tether ligands of both blocks "A" and "B" on NP surfaces to fabricate "non selective" NPs [10].

As expected, the equilibrium location of the NPs within a block copolymer melt is dictated by thermodynamics, namely, by the balance between enthalpy and entropy. There are enthalpic interactions between the chemically altered NP and the copolymer blocks. The entropic contribution has two prominent components: the translational entropy of the NPs and the configurational entropy of the polymer chains. In line with the above factors, it has been found that small sized selective NPs ($R<<R_{gyr}$; R=NP radius, R_{gyr} = Radius of gyration of polymer chains) uniformly disperse within the preferred block copolymer domain to gain translational entropy [11]. However, when the NP radius is comparable to the R_{gyr}, the polymer chains can lose significant configurational entropy if they try to wrap around the particles. Therefore, the chains push the particles away towards the chain ends (which lie at the center of the preferred domain), causing the NPs to line up at the center of the preferred BCP domain [9, 12, 13]. In addition, interesting results have been found for the case of non selective NPs. Experimentally, Kramer and coworkers have shown gold NPs with surfaces coated half and half with ligands of "A" and "B" respectively. Here the NPs line up at the interface between the two blocks due to enthalpic interactions of different surface ligands with different blocks [10]. As a consequence, they found that the presence of NPs at the interface led to a decrease in the number of A-B contacts, thereby weakening segregation between the two

blocks at the interface. In a recent study that we conducted using molecular dynamics simulations, we modeled our non selective NPs in such a way that the entire NP surface was identical and had equal interaction with both blocks [13]. In this case, one would intuitively expect the NPs to be uniformly dispersed in both blocks. However, the presence of NPs at the interface even in this scenario suggested that reduction in A-B contacts could be a driving force for such an assembly.

Besides investigating the spatial arrangement of NPs, there is interest in determining how the addition of NPs affects the formation of self-assembled structures or the phase diagram of block copolymers, which in turn will affect the final arrangement of NPs within the polymeric matrix. It has been found that addition of selective NPs leads to higher effective volume fraction of the preferred domain and therefore induces phase transitions between the thermodynamically stable self-assembled structures such as spheres, cylinders and lamellae [12, 14]. The nonselective NPs do not show any dramatic effects on the self-assembled structures except that their presence shifted the χN ODT to higher values; moreover, for a given χN, above a certain critical NP volume fraction, the structure transitioned from ordered to disordered due to a reduction in segregation between "A" and "B" [10, 12].

Most previous studies on BCP/NP systems have been limited to equilibrium state. We cannot overstate the importance of studying non equilibrium systems, given that deformation and flow is a constituent of most everyday manufacturing processes. During the manufacturing process a polymer-based melt can be exposed to shear, compressive, and tensile forces, which may affect the properties of the finished product. Knowledge of how the material behaves in such

circumstances is therefore imperative. To provide an insight into the effect of deformation on BCP/NP melt systems, we need answers to two important questions: 1) *Are the properties of the composites retained (which is a strong function of nanoparticle placement) even after they are processed into final products? ; 2) Can flow produce desirable effects and further help us to tailor nanoparticle placement and thereby improve material properties?*

Recently, we studied the effect of shear flow on different types of symmetric block copolymer/nanoparticle systems [13]. We obtained interesting results not only on how the placement of NPs gets affected under shear, but also obtained some insight into how the presence of nanoparticles affects the shear-induced transition of lamellar orientation in a symmetric diblock copolymer. This study was also important because shear has been shown to be very effective in inducing long range order in block copolymers, and a detailed study of this aspect provided an understanding of how nanoparticles behave when shear is used to generate long range order in block copolymer templates. However, shear flow is rarely the only process occurring in a typical polymer processing context. Following this argument, we study the effect of elongational flow on similar BCP and BCP/NP systems. This study is extremely important to compliment industrial processes such as blow molding, film molding and fiber spinning. Additonally, our interest arises from our recent experimental work on electrospinning of block copolymers and block copolymer/nanoparticle materials [15, 16]. Electrospinning is a fiber spinning process that uses strong electric field to accelerate and elongate a polymer solution/melt jet to form nanoscale fibers (diameter~50-500 nm) [15, 16, 17, 18]. This process involves very strong extensional deformation with strain rates as high as 10000 s^{-1}. We found some interesting results through this study both for pure BCP systems and BCP/NP

composite systems, which we anticipate to be effects of elongational flow during electrospinning [17, 18]. This work is intended to provide a qualitative explanation for our findings, along with some general insights into the effects of elongational flow to aid the optimization of various processes. Furthermore, through this work, we wish to provide a direct comparison to our recent findings of effect of shear flow on BCP and BCP/NP systems [13].

Effects of elongational flow have not been very well studied even for simple polymeric systems in the past, the reason for which will become clearer below. Three basic kinds of elongational flow are planar elongational flow (PEF), uniaxial stretching flow (USF) and biaxial stretching flow (BSF). In each of these flows, there is at least one dimension that is continuously shrinking with time, making it extremely difficult to devise an apparatus in which steady state is achieved. Typical experimental methods record the transient properties, with an extrapolation then made to obtain the steady state properties [19, 20, 21]. Based on our literature survey, only a handful of publications have studied the effect of elongational flow on block copolymers. Kwon *et al.* studied the elongational flow-induced alignment process of a lamellar-forming polystyrene-b-poly(ethylene-propylene) (SEP) diblock copolymer using opto-rheometry and small angle X-ray scattering [22]. They studied two cases with different initial lamellar orientation both under a small henky strain rate of 0.01 s^{-1}. In the first case, extension was applied perpendicular to the lamellae normal, while in the second case, extension was applied parallel to the lamellae normal. In both cases, the lamellae finally oriented such that their normal was perpendicular to the flow direction before rupture of the sample material took place. Extensional flow has also been shown to cause micronecking and breaking of ordered block copolymer domains [23, 24, 25].

The computation of the elongational flow via Non Equilibrium Molecular Dynamics (NEMD) has been plagued by similar problems to those found in experiments. The contraction, occurring in at least one dimension imposes a limit on the amount of time we can run a simulation. This problem is particularly critical for study of steady state behavior of slow relaxing systems like polymers. Although, some methods such as appropriate selection of initial system dimensions [26] or using an oscillating elongational field [27, 28], but none of these methods can improve the allowed simulation time sufficiently to study polymers. Moreover, schemes such as starting with larger initial system dimension will also greatly increase the computational cost.

Kraynik and Reinelt showed that it is possible to perform PEF on a initial lattice structure, maintaining both spatial and temporal periodicity [29]. Here the initial simulation box is inclined at a certain angle θ_o to the flow direction. The system boundaries are allowed to deform with the flow, and after a certain time, the lattice can be seen to reproduce itself, making the simulation periodic in time. The advantage of using such a technique is that it allows the simulation to run indefinitely. Todd and Daivis, very efficiently implemented the Kraynik-Reinelt (KR) periodic boundary conditions in an NEMD simulation of planar elongational flow (PEF) to study different polymeric systems [30, 31]. We adopt a similar scheme in this paper to study the effects of planar elongational flow. We will talk about this scheme in more detail in following sections.

In the current work, we present results on coarse-grained molecular dynamics simulations we performed to model BCP/NP mixtures that are subjected to planar elongational flow. As mentioned above, effects of elongational flow have not been extensively studied for block copolymer systems. Therefore, we first

study how a symmetric block copolymer self assembly changes with increasing elongational flow rate. This study is conducted with no nanoparticles. Then we study composite systems with 10 vol% nanoparticles in symmetric block copolymer melts. Here we take the case of both "selective" and "non selective" NPs for a fixed NP diameter over a range of elongational flow rates. From these simulations we aim to address three questions: 1) *How does elongational flow affect the block copolymer self assembly?; 2) How does elongational flow affect the spatial distribution of NPs?; 3) How does the presence of NPs affect the flow-induced transition in BCP self assembly?* Our ultimate goal is to elucidate the conditions that are necessary to gain even greater control of the highly ordered placement of NPs.

In the following section we describe the manner in which we modeled the block copolymer and the nanoparticles. We show the pair-wise potentials for all species, and we provide details on the computational method employed to make the system temporally periodic. In the Results Section, we present simulation results on pure block copolymer system and the different nanocomposite systems that we studied under elongational flow. Finally, in the Discussion Section, we suggest mechanisms that could explain our findings.

8.3 Model and Computational Details

8.3.1 Potentials

The copolymer chains in the current study are modeled as bead-rod chains. In order to fix the bond lengths, we have adopted a method of constraints de-

scribed by Bruns *et al* [32]. In this method, first positions of all beads in a particular chain are calculated using Newton's equations of motion. Then the deviation of the new bond lengths from the desired bond length is used to calculate the correction term. This correction term is then used to calculate a new position value of all beads. This process is repeated until all bonds attain a constant desired value of 1.0 MD units within an error of 0.00001.

Since we are dealing with a diblock copolymer, the chains consist of "A" and "B" blocks of monomers. The excluded volume interactions between the A and B monomers are accounted for by the purely repulsive, cut and shifted, Lennard-Jones (LJ) potential which is often referred to as the WCA potential [33],

$$u^{REP}(r) = 4\varepsilon\left[\left(\frac{\sigma}{r}\right)^{12} - \left(\frac{\sigma}{r}\right)^{6}\right] + \varepsilon = u^{LJ}(r) + \varepsilon, \quad r \leq 2^{1/6} \tag{8.1}$$
$$u^{REP}(r) = 0, \quad r > 2^{1/6}$$

where r is the separation distance between beads, and σ are ε are the Lennard Jones parameters, taken to be unity for the sake of simplicity.

To incorporate the physics of microscopic phase separation between the A and B species, we utilize an attractive potential between like monomers (i.e., $A-A$ or $B-B$). This interaction taken together with the repulsive $A-B$ potential ensures that phase separation will occur if the temperature is below the order-disorder transition temperature. We use the same attractive potential that was used by Horsch and coworkers [34] to model the equilibrium properties of diblock copolymer melts. This is again a LJ potential but now it is cut and shifted at values that differ from those presented in Eq. 8.1,

$$u^{ATT}(r) = 4\varepsilon\left[\left(\frac{\sigma}{r}\right)^{12} - \left(\frac{\sigma}{r}\right)^{6}\right] + u^{LJ}(2.5), \quad r \leq 2.5 \tag{8.2}$$
$$u^{ATT}(r) = 0, \quad r > 2.5$$

The higher cut-off means that this is not purely repulsive and that monomers of the same type are attracted to each other. With this potential, Horsch *et al* generated various points in the phase diagram, and found good agreement with the phase diagram from mean field theory. These authors derived the Flory-Huggins χ parameter between the A and B sites as a function of the simulation temperature [34]. In the present work, we performed all simulations for model symmetric block copolymers at a temperature that results in χN value (~50) well above the order disorder transition.

For the nanoparticles, we model two different types of particles, namely selective and non selective. For selective particles, we use a purely repulsive potential between monomer "B" and particle "P" (eq. 8.1) and for the interaction between monomer "A" and P, we use the Lennard Jones potential with an attractive tail = u^{ATT} (eq. 8.2). For Non selective nanoparticles, the interaction of P with both monomer "A" and monomer "B" =u^{ATT}. P-P potential used in all systems =u^{ATT}. Table 8.1 summarizes the interactions between different elements in various systems.

Table 8.1: Summary of interactions between the nanoparticles (P) and the A and B monomers of the diblock copolymer.

Selective	u^{ATT}	*A-A, B-B, P-P, A-P*
	u^{REP}	$A-B, B-P$
Non Selective	u^{ATT}	*A-A, B-B, P-P, A-P, B-P*
	u^{REP}	$A-B$

Our simulation model neglects the effect of nanoparticle rotational dynamics on the rheological behavior of our systems. Note that although such rotational effects are irrelevant for thermodynamic behavior, they are important

for flow behavior. It is expected, however, that such effects will become more significant the higher the concentration of nanoparticles in the system and the higher the shear rate. We assume that the nanoparticle surface functionalization is such that rotation modes tend to be suppressed and that for the relatively low nanoparticle concentration used in this work (10 vol%), such rotational effects are small compared to that of the translational modes. This is clearly an approximation but is expected not to greatly affect the qualitative response of our systems under shear flow.

8.3.2 Computational Details

Throughout these simulations we fixed the polymer chain length to 10 monomers or beads. The particle volume fraction was fixed at 0.1 for both selective and non selective NPs to preserve lamellar morphology in the nanocomposite[12]. The site density, ρ, was kept fixed at 0.85 and the temperature, k_BT, was kept at 1.0 using the gaussian thermostat [31]. The velocity verlet algorithm was used to integrate the equations of motion with a time step=0.005. The simulations were run for a sufficiently long time until variables such as pressure, potential energy, radius of gyration and mean squared end to end distance remained constant.

We note that the NP size used for most part of the current work is same as the size of the monomeric bead (~ kuhn monomer [36]) and one could then consider such NPs to actually represent a solvent or small oligomer. However, the "NP size/polymer radius of gyration" ratio corresponding to NPs used in this work has been found in practice in several instances [37, 38, 39]. From our

preliminary results, we find that the radius of gyration of a copolymer chain in the pure block copolymer system used in this work is R_{gyr}=5.9, corresponding to σ_P/R_{gyr} = 0.17, where σ_P(NP size)=1. Table 8.2 summarizes some of the parameters used in this work.

Table 8.2: Simulation Parameters

Parameters	**Symbol**	**Value (MD units)**[1]
Temperature	k_BT	1
monomer size	gσ	1
NP diameter	σ_P	1
NP,monomer mass	M	1
Chain length	N	10
Bead density	ρ	0.85
Cubic box size	L	16.758
NP fraction	ϕ_P	0, 0.1
Number of chains	M	400
Flory Huggins parameter*N[20]	χN	53.3
MD integration time step	Δt	0.005
Copolymer radius of gyration	R_{gyr}	5.9
Elongational rate	$\dot{\varepsilon}$	0.0-0.15

[1]The values in MD units are understood to be multiplied by the appropriate combinations of three independent fundamental units of length, mass and energy [40].

8.4 Implementation of Elongational Flow

To implement planar elongational flow with temporally periodic boundaries, we adopt an algorithm first proposed by Todd and Daivis using the boundary conditions devised by Kraynik and Reinelt [29, 30, 31]. Here, we start the simulations with an initial box/lattice inclined at an angle θ=31.7^o to the direction of elongation (x). Kraynik and Reinelt showed that for certain discrete values of θ the lattice is both spatially and temporally periodic. The lattice has been shown to repeat itself at integer multiples of a fixed strain termed as 'henky strain (ε_p)'. So the system remains temporally periodic at times t=nτ_p, where n is an integer multiple and $\tau_p = \varepsilon_p/\dot{\varepsilon}$. The boundaries of the simulation lattice evolve according to Eq. 8.3 (obtained by integrating the governing equations of motions). At t=τ_p, the lattice reproduces itself. If any particle/bead is outside of the lattice boundaries at any step, they are appropriately translated in x, y and z directions, such that it re-enters the test simulation box.

$$\begin{aligned} x(t) &= x(t=0)\ \exp(\dot{\varepsilon}t) \\ y(t) &= y(t=0)\ \exp(-\dot{\varepsilon}t) \end{aligned} \tag{8.3}$$

To implement the spatial periodic boundary conditions in the elongated lattice, we use the deforming brick scheme as described by Todd and Daivis [30].

We use the SLODD equations of motion with a Gaussian thermostat to implement elongational flow.

$$\frac{d\vec{r}_i}{dt} = \frac{\vec{p}_i}{m_i} + r_i \cdot \nabla\vec{u} \tag{8.4}$$

$$\frac{d\vec{p}_i}{dt} = \vec{F}_i - \vec{p}_i \cdot \nabla\vec{u} - \alpha\vec{p}_i \tag{8.5}$$

where, $\vec{r}_i$is the position of particle/bead i, $\vec{p}_i$is the peculiar momentum of particle/bead i, m$_i$ is the mass of particle/bead i, $\nabla\vec{u}$ is the velocity gradient and α is

the Gaussian thermostat multiplier.

$$\nabla u = \begin{bmatrix} \dot{\varepsilon} & 0 & 0 \\ 0 & -\dot{\varepsilon} & 0 \\ 0 & 0 & 0 \end{bmatrix} \tag{8.6}$$

$$\alpha = \frac{\sum_i p_i . \left[F_i - (p_i . \nabla u)\right]}{\sum_i p_i^2} \tag{8.7}$$

The pressure (total stress) tensor is calculated using:

$$P = \frac{1}{V}\left(\sum_i^{nM} \frac{p_i p_j}{m_i} + \sum_{j>i}^{nM} r_{ij} F_{ij}\right) \tag{8.8}$$

We calculate elongational viscosity as:

$$\eta_E = \frac{P_{yy} - P_{zz}}{4\dot{\varepsilon}} \tag{8.9}$$

This values of viscosity (η_E) and pressure are first calculated for bead-rod homopolymer systems and the values obtained are compared with those of Matin *et al.* [35] for validation of our code. This validation is conducted for different chain lengths of N=1, 2, 4, and 10.

8.5 Results

8.5.1 Effect of Elongational Flow on Block Copolymer Self Assembly

We conducted simulations for a pure block copolymer melt system for different elongational rates ranging from $\dot{\varepsilon}$=0 to $\dot{\varepsilon}$=0.2 MD units at intervals of 0.001/0.005

at lower flow rates and intervals of 0.02 at higher flow rates. We find that for $\dot{\varepsilon}$<0.025, the system develops an ordered lamellar morphology at steady state, while for $\dot{\varepsilon}\geq$0.025, a disordered morphology is formed. In figure 8.1, we show simulation snapshots for $\dot{\varepsilon}$=0.005 and $\dot{\varepsilon}$=0.2 showing ordered lamellar and disordered morphology, respectively. In figure 8.2, we plot the concentrations of block A and block B along the z axis. In figure 8.2a indicates strongly segregated blocks with ordered lamellae consistent with the snapshot in figure 8.1a. Also, the concentration profile in figure 8.2b is uniform throughout the z axis indicating disordered or homogeneous morphology. Figure 8.2c shows the concentration profile of blocks A and B at different elongational rates. It is predicted that the segregation between A and B blocks gradually decreases with increasing flow rate. For flow rates $\geq$ 0.025, no identifiable ordered structure is seen in the simulation snapshots (figure not shown). Figure 8.2d shows the elongational viscosity of the system as a function of flow rate. Absence of any sudden drop in viscosity indicates the order-disorder transition under extensional flow is a gradual one, unlike the parallel to perpendicular lamellar transition seen under shear flow [38, 39]. An interesting thing here is that for all low flow rates where ordered lamellae is formed, lamellae develop in the perpendicular orientation. Here, we define perpendicular orientation as the one where normal to the lamellae is along the neutral (z) direction (similar to the way it is defined for shear flow). We do not see parallel orientation for any of the flow rates studied. Again, the parallel orientation is defined as the one where the layers are parallel to the extensional flow direction. This is different from the shear flow case, where it has been shown through both experiments[38, 39] and simulations[41, 42], that parallel lamellae are formed at low shear rates. In our recent Molecular Dynamics study of shear flow, we had found parallel lamel-

lae for low flow rates comparable to the ones used in this study[13]. However, shear flow has been shown to induce a transition of orientation from parallel to perpendicular lamellae on increasing the flow rate [38, 41, 13]. Perpendicular lamellae in these studies has been associated with lower potential energy and a lower modulus, thus providing an energetic reason favoring such transition. A very interesting analogy suggested by Wiesner and coworkers compares the block copolymer chains during perpendicular alignment to rolling logs, that shows less resistance to flow than in parallel alignment [38, 39]. A possible explanation for appearance of only perpendicular lamellae and absence of parallel lamellae even at low flow rates during elongational flow could be that the the deformation effect is more drastic during extension compared to shear flow. Morevover, in a parallel lamellar morphology under extensional flow, the polymer chains would be parallel to the contraction direction (y) and would therefore experience much higher resistance, unlike shear flow where there is no contraction. As mentioned above, at high elongational rates, a disordered morphology is formed. Such a transition could be driven by a tendency of the polymer chains to align along the flow axis (x axis) causing the blocks to lose their order. Rupture of ordered domains into smaller broken domains has also been found experimentally. Seguela *et al.* studied elongational deformation mechanism of solution cast films of polybutadiene-hydrogenated SBS block copolymer exhibiting lamellar morphology [23]. They found that lamellae undergo necking and rupture at high elongational rates. Pakula and coworkers studied the extensional deformation behavior of Styrene-Butadiene-Styrene block copolymer exhibiting cylindrical morphology [24]. They presented a variety of deformation behaviors that occur when the oriented microdomain structure is deformed at various angles to its original orientation. They also found that

rupture of domain structures takes place at high extension rates. Moreover, in our recent work on electrospinning of block copolymers, we had seen that disordered morphology forms in as-made electrospun nanofibers. The electrospinning process involves very strong extensional deformation with strain rates as high as 10000 s^{-1}.The simulation results above provide a reasonable explanation for formation of such disordered structures. Figure 8.3 shows the mean squared end to end distance of polymer chains ($<R^2>$) in x, y and z direction as a function of shear rate. $<R^2(x)>$ monotonically increases with increasing flow rate due to the orientation of chains along the flow axis. For low flow rates, $<R^2(z)> > <R^2(y)>$ due to the presence of perpendicular lamellae. With increasing flow rate, $<R^2(z)>$ decreases and $<R^2(y)>$ increases as the morphology shifts from ordered to disordered. The gradual decrease in $<R^2(z)>$ (and absence of a sudden drop) with increasing flow rate indicates a gradual shift of morphology from ordered lamellae to disordered structure. Furthermore, $<R^2(z)>$ drops to $\sim$ zero at $\dot{\varepsilon}$=0.2. This suggests that the chains tend to lie in the x-y plane at high elongational rates.

8.5.2 Spatial Distribution of Selective Particles within Diblock Copolymers

Here we study the effect of elongational flow on distribution of selective nanoparticles (NPs) in block copolymer melts. Here the NPs are modeled in such a way that they have a preference for block *A*. Here again, we find that the morphology shifts from ordered perpendicular lamellae to disordered as we increase the flow rate. However, this time such transition takes place at a higher

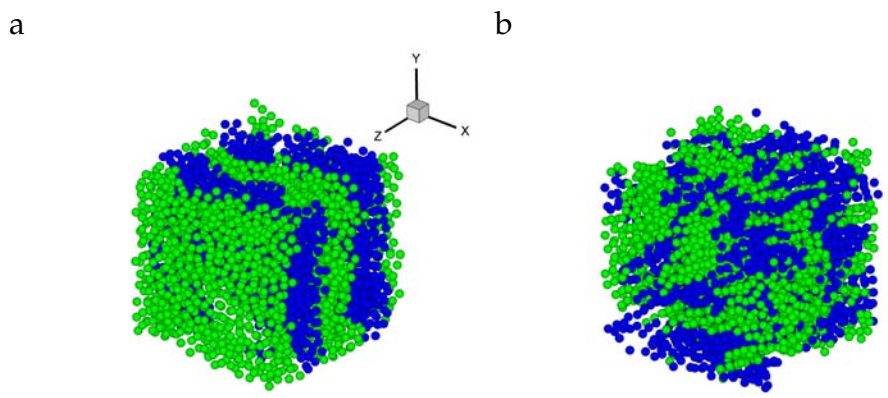

Figure 8.1: Symmetric diblock copolymer melt. Snapshots from MD simulations for $\dot{\varepsilon}$ a)= 0.005, b)=0.2. Green and Blue regions are blocks *A* and *B* respectively.

extension rate, $\dot{\varepsilon}$=0.03 than the pure BCP case. In figure 8.4a and b, we show simulation snapshots at $\dot{\varepsilon}$=0.005 and 0.2 respectively showing ordered and disordered morphology respectively. In both parts, we show snapshots from two different angles, to show the NP location more clearly. In addition, we plot the concentration of blocks *A* and *B* and the NPs along the z axis for $\dot{\varepsilon}$=0.005. We note that the concentration of *A*-selective NPs in the *B* domain remains zero, in spite of the flow. These results show that the NPs have a tendency to line up at the center of the *A* domain. For the NP size/polymer end to end distance ratio used in this work, such results have been found both experimentally and through simulations for quiescent/equilibrium systems [9, 12]. Our results in this work indicate that the NPs maintain this tendency inspite of the strong extensional flow conditions. And 'prevention of configurational entropy loss' still remains the dominant force, which pushes the particles close to *A* chain ends at the center of the A domain [9, 12, 13]. This result is similar to what we found for shear flow in a previous study [13]. Then we studied the effect of elonga-

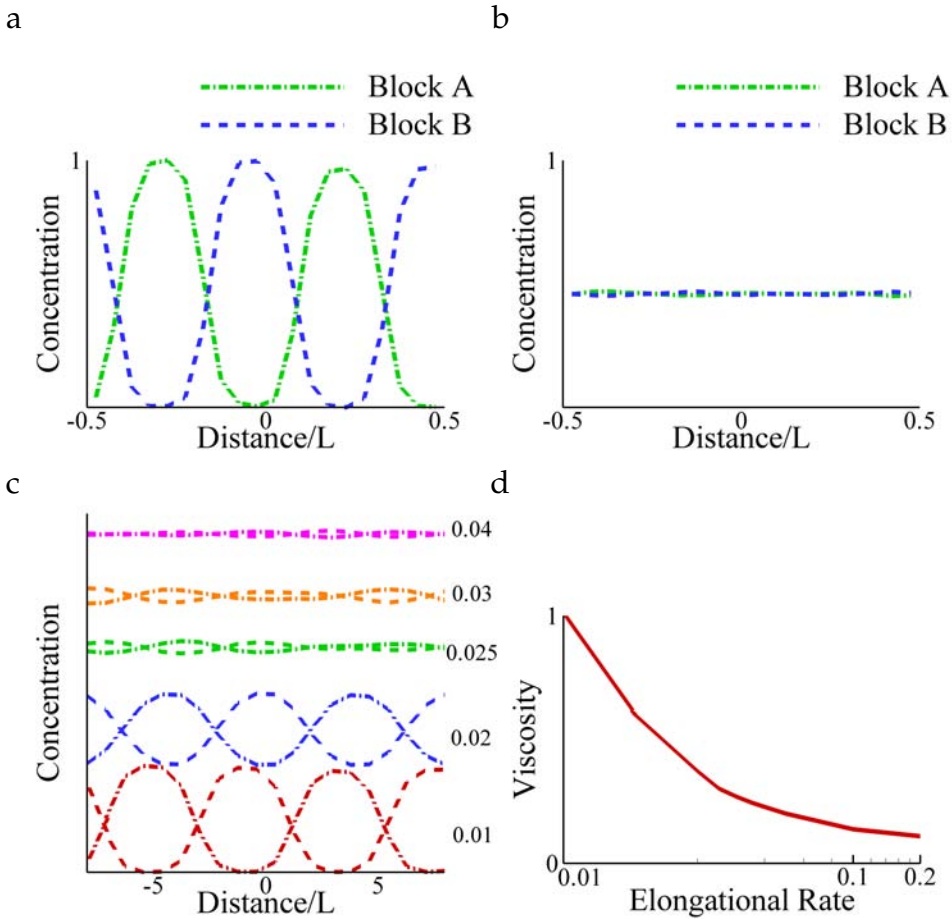

Figure 8.2: a,b) Concentration profiles of blocks A and B in a diblock copolymer melt along z axis for $\dot{\varepsilon}$= a) 0.005, b) 0.2. c) Concentration profiles of blocks A and B at different elongational flow rates. Flow rate value in MD units is written next to each curve. Curves have been vertically shifted for clarity. d) Viscosity vs. elongational flow rate for a diblock copolymer melt.

tional flow strength on the NP concentration peak (at the center of A domain) shown in figure 8.5a. Here, we restrict ourselves to elongational rates where ordered lamellar structure is formed. The figure shows that the peak of the selective NP concentration in the A domain broadens as we increase the flow rate. This could be attributed to the decreasing segregation strength between the two blocks, causing a decrease in A-chain end density at the center of the A domain.

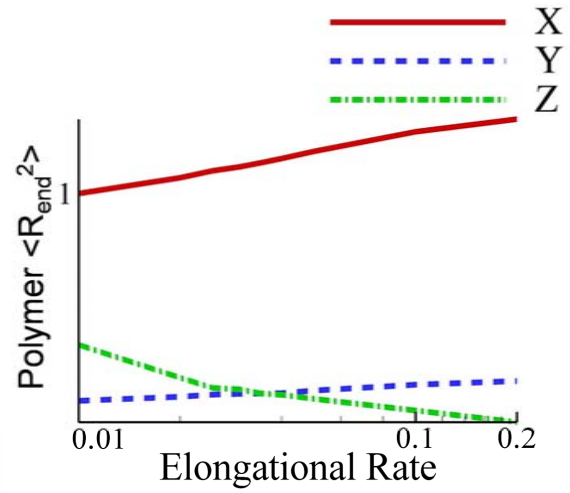

Figure 8.3: Mean squared end to end distance of polymer chains in a pure BCP melt in x, y and z directions as a function of elongational rate. All values have been normalized using $\langle R^2(x) \rangle$ at $\dot{\varepsilon}=0$.

To support this argument, we also plot the *A*-chain end concentration for different elongational rates in figure 8.5b. These simulation results suggest that the entropic contributions play a significant role in determining the assembly of NPs in block copolymers under deformation. We would like to point out here, that for the case of shear flow also, we had found that entropic contributions play a dominant role. However, under shear flow, the NP concentration peak sharpened with increasing shear rate, due to the shear-induced suppression of fluctuations (that lead to an increase in *A*-chain end density at the center of *A* domain as a function of shear rate) [13]. Here we report the opposite trend for elongational flow that the concentration peak of selective NPs becomes broader with increasing extension rate.

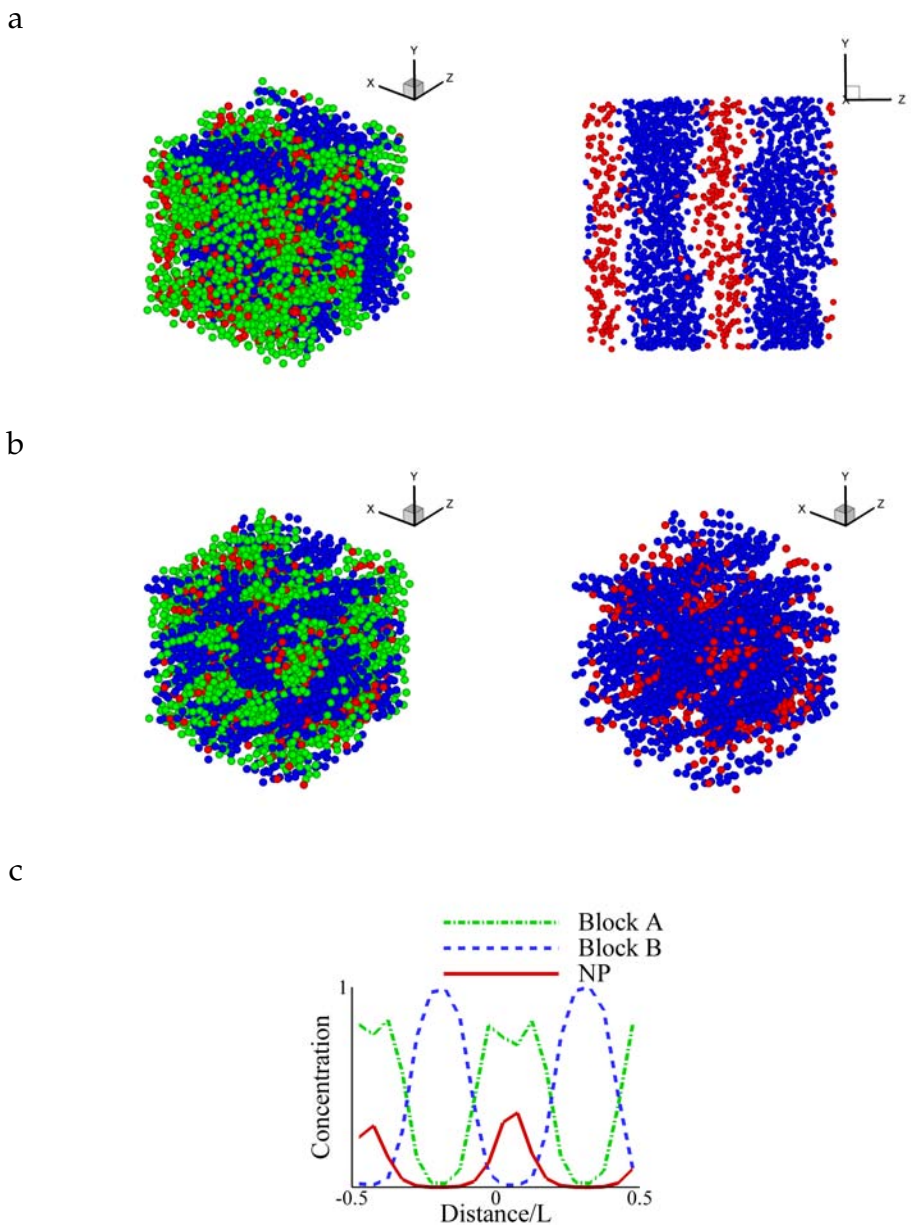

Figure 8.4: Symmetric diblock copolymers mixed with selective NPs. (a) Snapshots from a MD simulation with $\dot{\varepsilon} = 0.005$. For the figure on the right, block A is not shown for the sake of clarity, b) Snapshots from a MD simulation with $\dot{\varepsilon} = 0.2$. For the figure on the right, block A is not shown for the sake of clarity, c) Concentration profiles of blocks A, B and NPs along z axis for case shown in part (a). Green region is block A, blue region is block B and red beads are NPs. Concentration plot is normalized with the maximum concentration value of block A (or B).

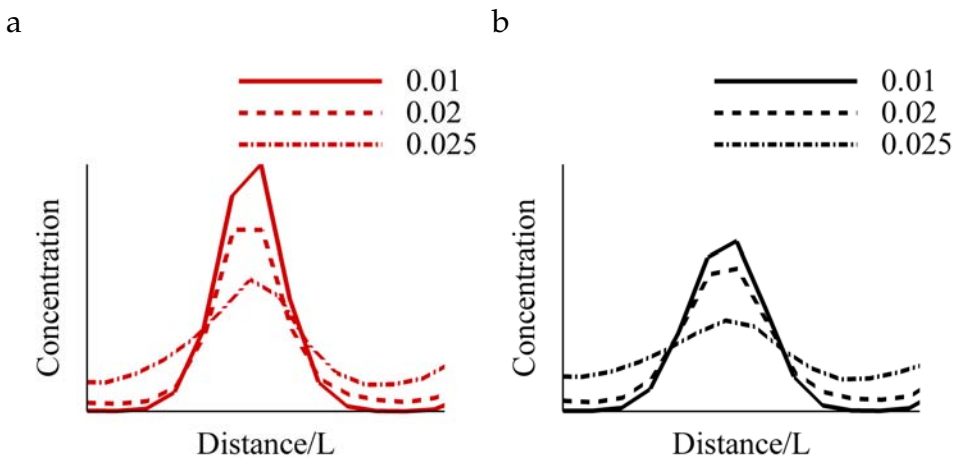

Figure 8.5: Symmetric diblock copolymers mixed with selective NPs. a) NP concentration profile for different elongational flow rates, b) *A*-chain end concentration profile for different elongational flow rates.

8.5.3 Spatial Distribution of Non Selective Particles within Diblock Copolymers

In Figure 8.6a and b, we present a snapshots of the structures we obtained from our simulations of Non Selective NP/BCP system. Here the NPs are modeled in such a way that they have equal preference for both blocks *A* and *B*. Again, we see a transition of morphology from ordered perpendicular lamellae to disordered structure, except this time this transition takes place at a lower extension rate, $\dot{\varepsilon}$=0.02 than the pure BCP case. In addition, the image indicate that the NPs are preferentially located at the interface between *A* and *B* domains. In Figure 8.6c we see distinct peaks in the concentration profiles which mean that the NPs are centered between the minima of the *A* and *B* monomer concentration profiles. The non-selective particles are equally attracted to the monomers of both copolymer blocks, therefore, we expect that the particles show no en-

thalpic preference for either domain. The main driving force causing the particles to position at the *AB* interface is the reduction in interfacial tension arising from decrease in *AB* contacts [12, 13]. However, the particles are not zero in A and B domains due to the favorable interactions between NPs and *A* (and *B*) domains. Our results qualitatively agree with the findings of Schultz *et al* who studied similar systems under no flow conditions [12]. The concentration profile has been normalized with the maximum *A* (or *B*) concentration. In 8.7, we plot the NP concentration as a function of elongational rate. Here again we only consider flow rates where an ordered lamellar structure is formed. Consistent with the Selective NP case, we see that the NP concentration peak becomes broader as the flow rate increases due to a decrease in the segregation between blocks *A* and *B*.

8.5.4 Flow-induced Transitions in Lamellae Orientation

As noted above, we see a transition from ordered lamellar morphology to a disordered structure as we increase the elongational flow rate for all the above systems (pure BCP, selective NP/BCP, non selective NP/BCP). However, as seen from simulation snapshots and concentration profiles, this transition takes place at $\dot{\varepsilon}$=0.025 for the pure BCP case, $\dot{\varepsilon}$=0.03 for selective NP/BCP case and $\dot{\varepsilon}$=0.02 for non selective NP/BCP system. In addition to this, we studied this aspect using mean squared end to end distance in y and z direction as a function of elongational flow rate (see figure 8.8). We find that $<R^2(z)>$ decreases at different rates for the three systems, with the non selective NP case being the fastest and the selective NP case being the slowest, consistent with the results from snapshots and concentration profiles. Again, we would like to point out here

that the critical flow rates mentioned above (where the transition takes place) is rather approximate as this transition is gradual and not a sudden one. So here the rate at which this transition takes place would be more relevant (as seen from figure 8.8).

8.6 Discussion

In the first part of our results section, we considered the effect of elongational flow on pure block copolymer melts. Here we find that at low flow rates, the systems forms an ordered lamellar structure oriented in the perpendicular direction (i.e. the lamellae normal is parallel to the neutral (z) direction). However, at higher flow rates, the morphology evolves into a disordered structure. This transition is a gradual one, where the segregation between the two blocks decreases with increasing elongational rate and beyond a certain elongational rate (=critical rate), the morphology is no longer ordered. This effect stems from the tendency of the polymer chains to align along the flow direction, such that beyond a certain rate, the segregation between blocks no longer plays a role in determining the assembly of the system. This result is in agreement with experimental findings in the past, where extensional flow was shown to cause micronecking and breaking of ordered block copolymer domains resulting in disordered morphology [23, 24, 25]. Furthermore, in our recent work on electrospinning of block copolymers, we saw the formation of disordered morphology in as-made fibers partly due to the strong extensional deformation during the fabrication process [15, 16].

The formation of the perpendicular lamellae vs. parallel lamellae at low flow

rates can be justified as follows: In a parallel orientation, the polymer chains are perpendicular to the flow direction or the interface between strongly segregated A and B blocks is parallel to the flow direction, therefore the chains or the block copolymer domains feel a large resistance to flow. For the case of perpendicular orientation chains are oriented along the neutral (z) direction, making them slide /roll like a log when flow is applied. This rolling log analogy has been used by Wiesner and coworkers in the past for the perpendicular lamellar orientation seen during shear flow [38, 39]. However, in some of the experimental studies done in the past, it was found that the lamellae orient along the parallel direction under extensional deformation [22]. The strain rates used in the literature (=0.01 s^{-1} in Kwon *et al.* [22]) are much lower than those in this work (0.005 MD units $\sim 10^5$ s^{-1} [43]). Moreover, in real systems, modulus contrasts between the two blocks could play a prominent role, unlike our simulation model where such a contrast is not present. This contrast has been shown to result in the formation of parallel orientation under shear flow by Wiesner and coworkers [38].

In the second part of our results we consider block copolymer nanocomposite systems with two qualitatively different kinds of nanoparticles in a symmetric diblock copolymer melt, namely, selective and non selective NPs. For the case of selective particles, we find that the NP concentration profile exhibits a maxima at the center of the preferred domain *A* where most chain ends lie. This finding is in agreement with literature results (for quiescent systems) for the NP size to polymer ratio considered in this work [12, 2]. Here, the entropic contribution plays a dominant role and pushes the NPs close to the *A* block chain ends, since the energetics remain the same for NPs throughout the A domain. A broadening of the NP concentration peak is seen with the application of elonga-

tional flow. We suggested that this finding can be attributed to the flow induced suppression of *A*-*B* segregation causing the A-chain ends to be less defined at the domain center, leading to a less defined particle layer at the domain center. To further support this argument, we plotted the concentration profile of the "*A* chain end" for different elongational rates and we found a similar trend as the NP profile. This is in agreement with our recent simulation work on effect of shear flow on similar nanocomposite systems [13], where we had found that the *A*-chain end concentration is a significant factor in determining the NP concentration peak at the domain center (where most chain ends lie). However, under shear flow, this peak sharpens with increasing shear rate as shear flow suppresses concentration fluctuations and sharpens the *A*-chain end density at the domain center, unlike elongational flow.

For the non selective particles, NP concentration peak appears at the *A*-*B* interface. This phenomena is energetically favorable as the NPs tend to compatibilize the interface by reducing the number of *A*-*B* contacts. In this case, also, we see a similar broadening of the NP concentration peak with increasing elongational flow rates, owing to the same reduction in *A*-*B* segregation or broadening of the interface. We do note here, that for the case of non selective particles, the NP concentration peak at the *A*-*B* interface is a lot less sharp than the Selective NP concentration peak at the *A*-domain center. This could be possible explained as follows: for selective NPs, the particles experience the same enthalpic interaction throughout the A *A* domain, so the only force thats active and causes the particles to line up at the center is the entropic force. For the case of non selective NPs, there is a competition between two forces, the enthalpic force tries to keep the NPs at the interface as they reduce interfacial tension between *A* and *B*; and the entropic force tries to push the particles away from the

interface towards the chain ends to prevent any entropic penalty. Due to this competition, the driving force to keep the particles at the interface is not that strong and hence, a relatively less sharp peak is seen.

Lastly, we studied the critical shear rate at which the transition from ordered to disordered morphology takes place for the three systems. Here we found that for non selective particles, this critical shear rate reduces (compared to a pure block copolymer). As we mentioned above that non selective particles at the interface reduce the A-B segregation, therefore for such a system its much easier to form a disordered morphology. While, for the case of selective particles, we believe that the NPs help in bridging different A chains and strengthening the cohesive forces within block A causing an increase in effective segregation between A and B. Therefore the critical flow rate increases for the case of selective NPs. In our previous work on effect of shear flow, we had found a similar shift in critical shear rate. But in this case, this critical shear rate was the shear rate at which the transition took place from parallel to perpendicular lamellar. Although, this transition was a different one, but in both cases, the system goes through a disordered phase and the segregation between blocks A and B is very critical [41, 42, 44, 45, 46]. Our results for both elongational flow and shear flow [13] are consistent in this respect.

8.7 Conclusion

In this work, we have conducted a coarse grained molecular dynamics study on how planar elongational flow affects the self assembly of pure symmetric diblock copolymer melt systems and symmetric diblock copolymer/nanoparticle

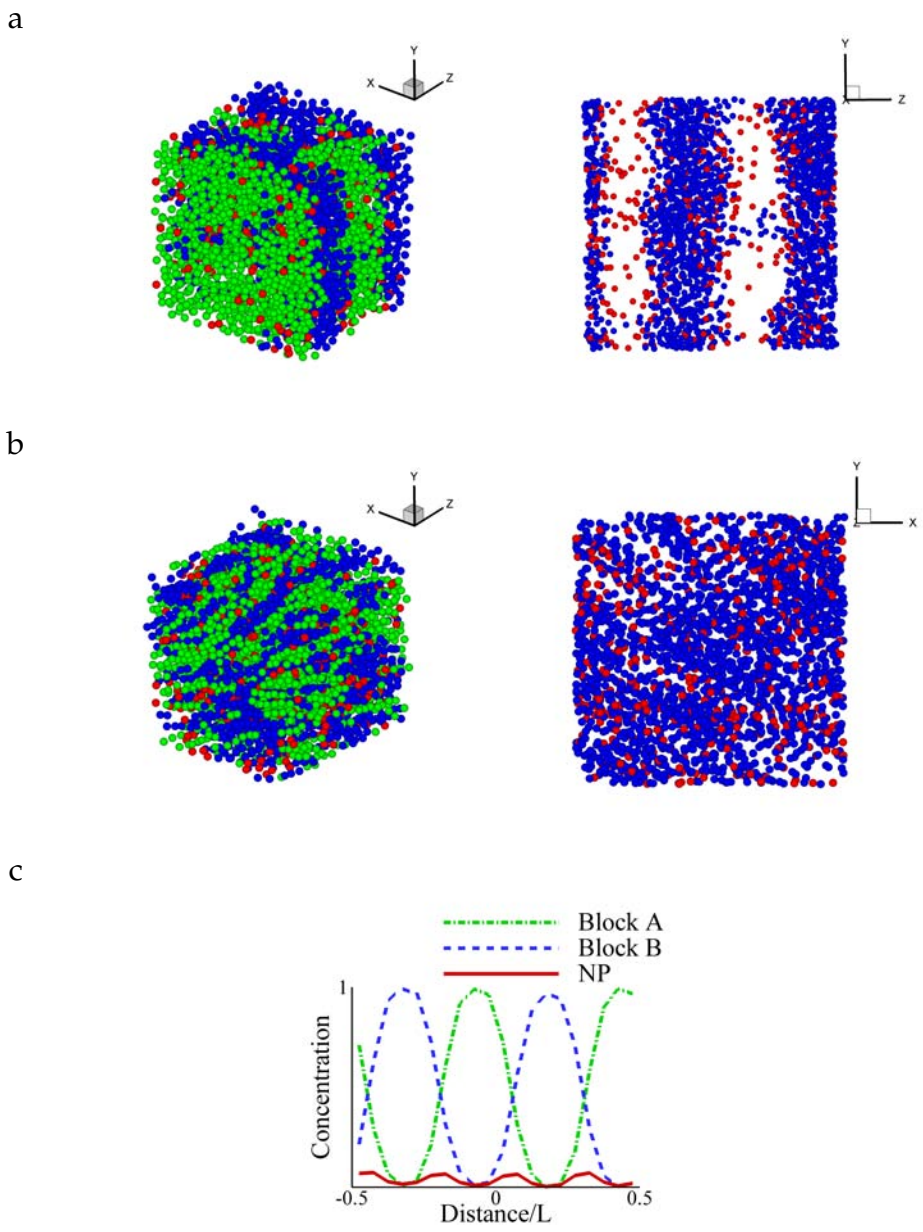

Figure 8.6: Symmetric diblock copolymers mixed with non selective NPs. (a) Snapshots from a MD simulation with $\dot{\varepsilon} = 0.005$. For the figure on the right, block A is not shown for the sake of clarity, b) Snapshots from a MD simulation with $\dot{\varepsilon} = 0.2$. For the figure on the right, block A is not shown for the sake of clarity, c) Concentration profiles of blocks A, B and NPs along z axis for case shown in part (a). Green region is block A, blue region is block B and red beads are NPs. Concentration plot is normalized with the maximum concentration value of block A (or B).

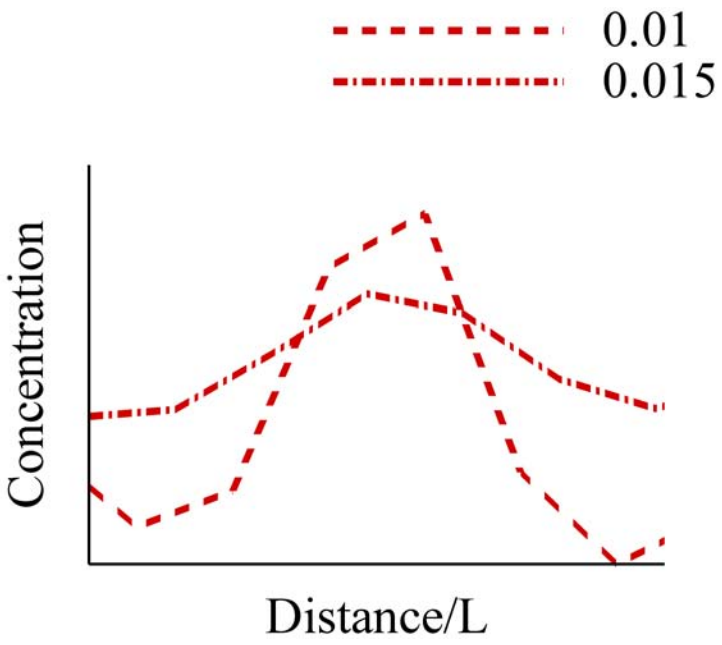

Figure 8.7: Symmetric diblock copolymers mixed with non selective NPs. NP concentration profile for different elongational flow rates.

composites. For unrestricted simulation times during elongational flow, spatially and temporally periodic boundary conditions devised by Kraynik and Reinelt have been implemented [29]. For the case of pure block copolymer melt, it was found that elongational flow causes a order-disorder transition as the flow rate is increased driven by the tendency of polymer chains to orient along the flow direction. Moreover, only perpendicular lamellae orientation was seen at low elongational flow rates possibly due to the compression along the y-axis during extension preventing the formation of parallel lamellae. For the study of block copolymer nanocomposites, we investigated two main aspects, namely, the effect of elongational flow on nanoparticle assembly within block copolymers and the effect of the presence of nanoparticles on flow induced order-disorder transition. Two different kinds of nanoparticles were considered in this

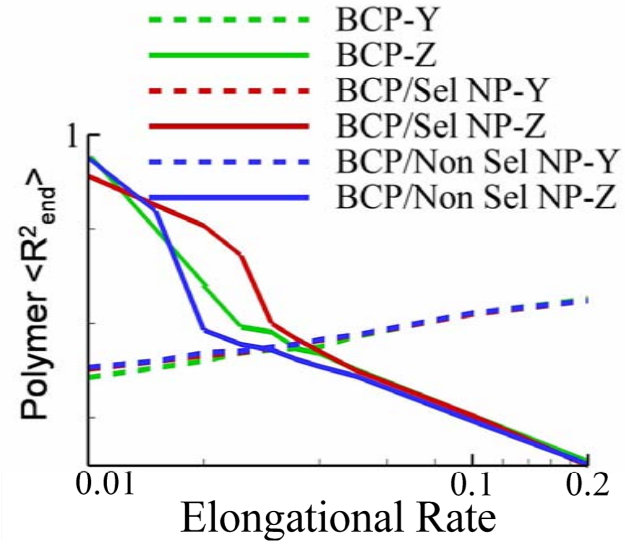

Figure 8.8: Mean squared end to end distance of polymer chains in three different systems in y and z directions as a function of elongational rate.

work, selective nanoparticles and non selective nanoparticles, categorized with respect to their interaction potentials with the polymer chains. For both cases we found that flow has a prominent effect on nanoparticle assembly and therefore can be used as a parameter to control the location of nanoparticles within block copolymers. In addition, it was shown that the presence of nanoparticles affects the critical flow rate at which the order-disorder transition takes place and such an effect is a strong function of polymer-particle interaction potentials. Mechanisms responsible for our findings have been suggested with a systematic comparison with the effect of shear flow on similar systems seen in literature and our own previous work [13].

BIBLIOGRAPHY

[1] Park, C.; Yoon, J.; Thomas, E. L. *Polymer* **2003**, 44, 6725.

[2] Bockstaller, M.R.; Mickiewicz, R.A.; Thomas, E.L. *Adv. Mater.* **2005**, 17, 1331.

[3] Buxton, G.A.; Balazs, A.C. *Phys Rev. E* **2003**, 67, 031802.

[4] Khandpur, A.K. *et al*. *Macromolecules* **1995**, 28, 8796.

[5] Pryamitsyn, V.; Ganesan, V. *Macromolecules* **2006**, 39, 8499.

[6] Balazs, A. C.; Emrick, T.; Russell, T. P. *Science* **2006**, 314, 1107.

[7] Hamley, I.W. *Angew. Chem. Int. Ed.* **2003**, 42, 1692.

[8] Shenhar, R.; Norsten, T.B.; Rotello, V. *Adv. Mater.* **2005**, 17, 657.

[9] Chui, J. J.; Bumjoon, J. K.; Kramer, E. J.; Pine, D. J. *J Am. Chem. Soc.* **2005**, 127, 5036.

[10] Kim, B.J.; Fredrickson, G.H.; Hawker, C.J.; Kramer, E. J. *Langmuir* **2007**, 23, 7804.

[11] Thompson, R.B.; Ginzburg, V.V; Matsen, M.W.; Balazs, A.C. *Science* **2001**, 292, 2469.

[12] Schultz, A. J.; Hall, C. K.; Genzer, J. *Macromolecules* **2005**, 38, 3007.

[13] Kalra. V.; Mendez, S.; Escobedo, F.; Joo, Y.L. *J. Chem. Phys.* **2008**, 128, 164909.

[14] Huh, H.; Ginzburg, V.V; Balazs, A.C. *Macromolecules* **2000**, 33, 8085.

[15] Kalra, V.; Kakad, P. A.; Mendez, S.; Ivannikov, T.; Kamperman, M.; Joo, Y. L. *Macromolecules* **2006**, 39, 5453.

[16] Kalra, V.; Mendez, S.; Lee, J. H.; Nguyen, H.; Marquez, M.; Joo, Y. L. *Adv. Mater.* **2006**, 18, 3299.

[17] Dzenis, Y. *Science* **2004**, 304, 1917.

[18] Li, B.D.; Xia, Y. *Adv. Mater*. **2004**, 16, 1151.

[19] Micic, P.; Bhattacharya, S.N. *Polymer Engineering and Science* **2000**, 40, 1571.

[20] Micic, P.; Bhattacharya, S.N. *Polymer International* **2000**, 49, 1580.

[21] Micic, P.; Bhattacharya, S.N.; Field, G. *International Polymer Processing* **1997**, 12, 110.

[22] Kwon, Y.K.; Ko, Y.S.; Okamoto, M. *Polymer* **2008**, 49, 2334.

[23] Seguela, R.; Homme, J.P. *Macromolecules* **1981**, 14, 197.

[24] Pakula, T.; Saijo, K.; Kawai, H.; Hashimoto, T. *Macromolecules* **1985**, 18, 1294.

[25] Daniel, C.; Hamley, I.W.; Mortensen, K. *Polymer* **2000**, 41, 9239.

[26] Hounkonnou, M.N.; Pierleoni, C.; Ryckaert, J.P. *Journal of Chemical Physics* **1992**, 97, 9335.

[27] Daivis, P.J.; Todd, B.D. *International Journal of Thermophysics* **1998**, 19, 1063.

[28] Todd, B.D.; Daivis, P.J. *Journal of Chemical Physics* **1997**, 107, 1617.

[29] Kraynik, A.M.; Reinelt, D.A. *International Journal of Multiphase Flow* **1992**, 18, 1045.

[30] Todd, B.D.; Daivis, P.J. *Physical Review Letters* **1998**, 81, 1118.

[31] Todd, B.D.; Daivis, P.J. *Computer Physics Communications* **1999**, 117, 191.

[32] Bruns, W.; Bansal, R. *J. Chem. Phys.* **1981**, 74, 2064.

[33] Weeks, J.D.; Chandler, D.; Anderson, H.C. *J. Chem. Phys.* **1971**, 54, 5237.

[34] Horsch, M.A.; Zhang, Z.; Iacovella, C.R.; Glotzer, S. *J. Chem. Phys.* **2004**, 121, 11456.

[35] Matin, M.L.; Daivis, P.J.; Todd, B.D. *J. Chem. Phys.* **2000**, 113, 9122.

[36] Kairn, T.; Daivis, P.J.; Matin, M.L.; Snook, I.K. *Polymer* **2004**, 45, 2453.

[37] Kalra, V.; Lee, J.; Lee, J.H.; Lee, S.G.; Marquez, M.; Wiesner, U.; Joo, Y.L. *Small* **2008**, 4, 2067.

[38] Leist, H.; Maring, D.; Thurn-Albrecht, T.; Wiesner, U. *J. Chem. Phys.* **1999**, 110, 8225.

[39] Maring, D.; Wiesner, U. *Macromolecules* **1997**, 30, 660.

[40] Allen, M.P.; Tildesley, D.J. *Computer Simulation of Liquids*; Oxford University Press, New York, 1987.

[41] Guo, H. *The Journal of Chemical Physics* **2006**, 124, 054902.

[42] Guo, H. *The Journal of Chemical Physics* **2006**, 125, 214902.

[43] Kremer, K.; Grest, G.S. *J. Chem. Phys.* **1990**, 92, 5057.

[44] Gupta, V.K.; Krishnamoorti, R.; Kornfield, J.A. Smith, S.D. *Macromolecules* **1995**, 28, 4464.

[45] Gupta, V.K.; Krishnamoorti, R.; Chen, Z-R.; Kornfield, J.A.; Smith, S.D.; Satkowski, M.M.; Grothaus, J.T. *Macromolecules* **1996**, 29, 875.

[46] Chen, Z-R.; Kornfield, J.A.; Smith, S.D.; Grothaus, J.T.; Satkowski, M.M. *Science* **1997**, 277, 1248.